IDŐJÁRÁS

QUARTERLY JOURNAL
OF THE HUNGARIAN METEOROLOGICAL SERVICE

CONTENTS

Márta Gaál and *Enikő Becsákné Tornay:* Drought events in Hungary and farmers' attitudes towards sustainable irrigation 143

Shaomin Cai, Weijia Zhang, and *Yizhou Zhao*: Retrieval of atmospheric trace gases from satellite infrared limb sounding data 167

Tibor Rácz: Wind speed estimation for the correction of wind-caused errors in historical precipitation data 199

Tímea Kocsis, Kinga Magyar-Horváth, Zita Bihari, and *Ilona Kovács-Székely:* Analysis of the correlation between the incidence of food-borne diseases and climate change in Hungary 217

Boryana Tsenova, Konstantin Mladenov, and *Milen Tsankov:* Graupel mixing ratio forecast from a cloud resolving numerical weather prediction model as a tool for lightning activity prediction 233

Noriza Khalid, Asma H. Sghaier, Márton Jolánkai, and *Ákos Tarnawa:* The role of temperature on the germination activity of leguminous crops exposed to saline conditions 257

VOL. 127 * NO. 2 * APRIL – JUNE 2023

* * * * *

IDŐJÁRÁS

Quarterly Journal of the Hungarian Meteorological Service

Editorial Office: Kitaibel P.u. 1, H-1024 Budapest, Hungary
P.O. Box 38, H-1525 Budapest, Hungary
E-mail: journal.idojaras@met.hu

Indexed and abstracted in Science Citation Index Expanded™ and Journal Citation Reports/Science Edition
Covered in the abstract and citation database SCOPUS®
Included in EBSCO's database

Subscription by mail:
IDŐJÁRÁS, P.O. Box 38, H-1525 Budapest, Hungary
E-mail: journal.idojaras@met.hu

DOI:10.28974/idojaras.2023.2.1

IDŐJÁRÁS

Quarterly Journal of the Hungarian Meteorological Service
Vol. 127, No. 2, April – June, 2023, pp. 143–165

Drought events in Hungary and farmers' attitudes towards sustainable irrigation

Márta Gaál* and **Enikő Becsákné Tornay**

Climate and Environmental Research Department
Institute of Agricultural Economics, Budapest, Hungary

**Corresponding author E-mail: gaal.marta@aki.gov.hu*

(Manuscript received in final form June 30, 2022)

Abstract— Among the different forms of agricultural damage in Hungary, drought poses a remarkably high risk according to the reported drought events, the area affected, and the level of mitigation payments. This study explores drought damage based on the 2018–2020 data of the Hungarian Agricultural Risk Management System. Owing to eligibility criteria, slightly more than half of the members of the scheme who reported drought damage received mitigation payments, but for them, the value of compensation significantly exceeded the mitigation contribution. According to our results, most of the damaged areas were outside the impact areas of water supply systems or were within the impact area but on non-irrigated fields, which proved that irrigation could be an effective drought mitigation tool. To avoid drought damage, irrigation development is essential, and special attention should be paid to the territory of Szabolcs-Szatmár-Bereg county. This area suffered significant drought damage in the years examined, and currently the impact area of the surface water-based water supply systems is small, while the groundwater resources are already overexploited. At the same time, the risk management system should be modified to transform it into a preventive system which encourages farmers to use water retentive soil cultivation methods, appropriate cropping systems, sustainable water management, and efficient and reasonable levels of irrigation. Accordingly, fewer mitigation benefits would be paid through less drought damage. Based on questionnaire surveys, farmers are open to using water retention practices and sustainable irrigation management.

Key-words: drought, Agricultural Risk Management System, irrigation, water supply systems, crops

1. Introduction

Over the last few decades, damage and losses caused by weather and climate-related extremes, such as floods, droughts, storms, and heatwaves, have increased all over the world. Among these natural disasters, drought is probably the most complex and severe due to its wide-ranging economic, social, and environmental impacts. Droughts can have cascading effects. For example, they reduce water levels in rivers and ground water, stunt tree and crop growth, increase pest attacks and fuel wildfires (EC, 2021). Agriculture is assumed to be one of the most drought-vulnerable sectors, as drought can substantially affect crops through many direct and indirect ways (*Musolino et al.,* 2018; *Vogt et al.,* 2018; *Cammalleri et al.,* 2020, *Trnka et al.,* 2022). While in the past the Mediterranean area was a region of major concern in Europe, central and eastern Europe and the Carpathian region have also become drought hotspots in recent decades. Long-term studies revealed that in the period June-August, a drying trend has been typical for the central and southern regions, including Czechia, Slovakia, Hungary, Romania, Moldova, and southern Poland (*Jaagus et al.*, 2021). Moreover, *Spinoni et al*. (2016) found that both drought frequency and severity have increased in the Carpathian region, in particular Hungary and Slovakia.

In recent years, such as 2003, 2007, 2012, 2015, 2017, substantial areas of the Danube River Basin were affected by water scarcity and drought (*Gregorič et al*., 2019). Extreme droughts in the western and central parts Europe in 2018, 2019 and 2020 caused considerable damage to agriculture. In 2018 alone, agricultural damage amounted to some EUR 2 billion in France, EUR 1.4 billion in the Netherlands, and EUR 770 million in Germany (EC, 2021). Using long-term observations, *Hari et al.* (2020) demonstrated that the occurrence of the 2018–2019 consecutive summer droughts across Central Europe was unprecedented in the last 250 years. More than 50% of the region suffered severe drought conditions, and its combined impact on the growing season vegetation activities was stronger compared to the 2003 European drought. The 2020 drought marked the third consecutive year of unexpectedly dry conditions across Europe. Central and Eastern Europe recorded a widespread lack of rainfall in April, less so during May (EDO, 2020).

The IPCC's Sixth Assessment Report (IPCC, 2021) showed that global warming will continue in the coming decades, and changes in extremes will continue to become larger. Future climate projections indicate increasing heat waves, longer warm seasons, shorter cold seasons and, in some regions, increasing agricultural and ecological droughts. Based on the results of the PESETA IV project, with global warming droughts are expected to be more frequent, longer lasting, and more intense in the southern and western parts of Europe, while drought conditions will become less extreme in northern and northeastern Europe. In the central parts of the region (Czechia, Austria, Slovakia, Hungary, eastern part of Germany), drought hazard conditions are projected to reduce slightly, yet uncertainty in the projections is highest here (*Cammalleri et al*., 2020). Using

model simulation for Central Europe, *Hari et al*. (2020) found that under the highest Representative Concentration Pathway (RCP 8.5), a seven-fold increase in the occurrence of consecutive droughts could be expected, with an additional 40 (±5) million hectares of cultivated area being affected by droughts, during the second half of the century. Under low and medium scenarios (RCP 2.6 and RCP 4.5), drought occurrence would be significantly reduced, suggesting that an effective mitigation strategy is needed.

In addition to the different spatial frequency, magnitude, and damage consequences of drought years, the resilience can also vary depending on the geographical and socio-economic conditions (*Blauhut et al.*, 2021). In the case of agricultural damage, crop species are characterized by different water requirements and drought tolerance. Furthermore, it is important to consider that the water demand of the plant species depends on their developmental (phenological) stage. May–June is critical for winter cereals for heading and grain filling, June–August for maize for tasseling and filling, June-July for lucerne after mowing, October for rapeseed for leaf development, and May-June for flowering and setting. Drought during the period of high water demand is the main cause of yield losses (*Antal et al*., 2005). An extensive analysis based on an ensemble of crop models (*Webber et al*., 2018) concluded that maintaining current genotypes, sowing dates, and the mix of rainfed and irrigated land use would result in a 20% decrease of maize yields by 2050. For winter wheat, a yield increase of 4% is projected when CO_2 fertilization is accounted for, versus a 9% decline without. However, for both crops, drought is the larger yield-limiting climatic factor across Europe.

According to the Global Water Partnership Central and Eastern Europe (GWP, 2019), most countries react to droughts as crises requiring emergency interventions, which can be costly. The alternative is to act before droughts occur to reduce the risks and their impacts, and they encourage governments to take this approach. Instruments for financing disaster recovery need to be in place, especially for coping with extraordinary catastrophic losses; however, farmers should be encouraged to invest in preparedness and private insurance instead of the risk and ex-post damage compensation (*Leitner et al*., 2020). As far as possible, a proactive approach should be preferred, such as increasing soil water retention capacity, increased groundwater storage, improvement of irrigation techniques, investment in water-saving technologies, and improvements in water supply (*Musolino et al*., 2018; *Vogt et al.*, 2018; *Kolossváry*, 2021).

A pan-European survey on drought perception and management highlighted that even though the awareness of a future increase of drought risk is prevalent, drought is often still not considered as a risk in Central, Northern and Eastern Europe (*Blauhut et al.*, 2021). This is consistent with the findings of *Mutua Ndue* and *Goda* (2021), that there is no single European Union (EU) Member State whose agricultural sector can be considered as fully climate adapted. Hungary is among those with weak potential for climate change adaptation and, thereby, very exposed to the impacts of climate change.

2. Hungarian climate trends and the agricultural risk management system

In this paper, we focus on Hungary, where agriculture plays a significant role in the economy. Hungary lies in the Carpathian Basin, where the natural conditions (climate, water, soil, and biological resources), particularly in the lowlands and plains, are generally favorable for agriculture. However, these conditions show high spatial and temporal variability. Humid conditions can be observed in the western parts and semiarid conditions dominate in the eastern regions of the country. The spatio-temporal distribution of precipitation is highly irregular and more and more frequently produce extremes.

Owing to the expansion of built-up areas, the productive land area is slowly decreasing, but still over 54% of the total area is used for agriculture (KSH, 2021). About 82% of the agricultural land is arable land (*Fig. 1*), the main crops are maize, wheat, sunflower, and rapeseed.

Under current conditions, crop systems are mainly rainfed and water licenses are underexploited. The share of irrigated (at least once a year) areas in Hungary is very low, with only 2.6%, compared to the EU-28 average of 5.9% (Eurostat, 2019). According to the General Directorate of Water Management (OVF), 3.0–3.7% of arable land is potentially irrigable, but only around 2% is irrigated. For orchards, the irrigable area varies between 11.5 and 12.8%, of which the actual irrigated area varies between 1.9 and 7.7% depending on the year (*Kolossváry*, 2021).

Several studies have been conducted to investigate climate change trends in the Carpathian region and Hungary for the period 1961–2010. According to the results, the first decade of the 21st century was the warmest period since 1901, with two heavy and three moderate drought events, and significant changes in the trends of the annual extreme temperature and precipitation indices can be observed (*Lakatos* and *Bihari*, 2011; *Lakatos et al*., 2016; *Mezősi et al*., 2016). For the same period, *Alsafadi et al*. (2020) reported that the north-eastern region was less sensitive to drought despite experiencing the highest duration of total drought. Their results also showed that the eastern part of Hungary was less vulnerable to drought, while the western part was more prone to drought. The southern-western part of the country received more rainfall than the central part, while the central part was more susceptible to rainfall changes and more prone to drought. Spatial analyses of *Szabó et al*. (2019) confirmed the western-eastern difference, with the smallest temperature increase in the Great Hungarian Plain and the largest in the Transdanubian Hills. Accordingly, in areas where the temperature was high, the level of further increase was smaller compared to colder areas in the western part of the country. *Berényi et al*. (2021) confirmed the increase in the frequency and intensity of extreme precipitation events, in the length of dry periods, as well as in the occurrence of extreme weather events in the Great Hungarian Plain for 1951–2019.

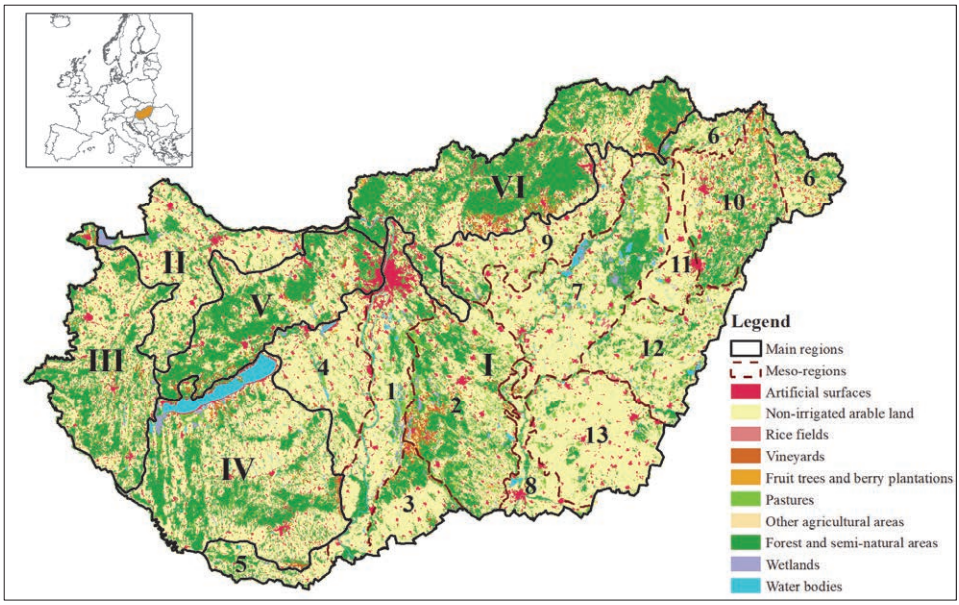

Fig. 1. Location of Hungary within Europe, the land use categories, and the main geographic regions: Great Hungarian Plain (I), Small Hungarian Plain (II), West-Hungarian Borderland (III), Transdanubian Hills (IV), Transdanubian Mountains (V), North Hungarian Mountains (VI). All the main regions can be divided into meso-regions, of which only the 13 meso-regions of the Great Hungarian Plain are highlighted.
Source: own editing based on CORINE 2018

Climate models predict that extremely hot days will become more frequent in the future, and summer rainfall could fall by more than 20% by the end of the century (*Lakatos* and *Zsebeházi*, 2018). Due to the increasing drought hazard and more frequent drought years, agricultural production conditions are expected to worsen throughout the 21st century (*Mezősi et al.*, 2016). The largest increase in the drought hazard by the end of the century is simulated to occur in the Hungarian Great Plain, while it is projected to be lowest in the westernmost part of the country (*Blanka et al*., 2013).

The Hungarian Agricultural Risk Management System (HARMS) has been operating since 2012 to address adverse climate impacts. The system consists of four pillars: (1) the compensation scheme, (2) the subsidized insurance, (3) the National Hail Damage Reduction System, and (4) the Agricultural Crisis Insurance System, which is the most recent income stabilization tool (*Lámfalusi* and *Péter*, 2021).

Pillar 1 provides damage compensation for farmers when winter frost, spring frost, autumn frost, floods, inland inundation, storms, heavy rainfall, hail, or

drought damage occurs. There is a mandatory membership of the risk-sharing community in Pillar 1, when the farmers' cultivated area fulfils either:

- 10 ha for arable crops
- 5 ha for field vegetables
- 1 ha for plantations
- 5 ha for plantations combined with field vegetables
- 10 ha for all categories combined.

Smallholders, whose areas do not reach the requirements above are allowed to join voluntarily. The Hungarian single area payment scheme (SAPS) distinguishes approximately 460 crop codes, of which around 300 are relevant for Pillar 1. Forests, meadows, pastures, green manure crops, and some other specified crops are not covered by the compensation scheme. The system covers approximately 3.7 million hectares; plantations have the highest share of area involved (95.3%), followed by arable crops and vegetables (92.9% and 92.5%, respectively). Annual membership contributions are calculated per area unit: HUF 1000 per hectare for arable crops and HUF 3000 per hectare for vegetables production and plantations (from 2021, a 1.5-fold increase has been applied). The main eligibility criteria for compensation are a certified yield loss at minimum damage threshold of 30% and yield value loss at minimum 15% compared to the Olympic average (excluding the highest and lowest value) of the past five years.

Drought events are difficult to characterize, since there is no generally accepted definition for them. Several drought indices have been developed to determine the duration and severity of drought. The Act No. CLXVIII of 2011 on handling of weather-related and other natural risks affecting agricultural production defines the drought as a natural phenomenon, when during the growing season of the crop concerned, at a certain location, the total precipitation is less than ten millimeters for a period of thirty consecutive days, or the precipitation is less than twenty-five millimeters, and the maximum daily temperature exceeds 31 °C for at least fifteen days. As part of the risk management system, the National Meteorological Service (OMSZ) determines the fulfilment of these criteria based on data from around 120 automatic measuring stations and nearly 500 rainfall measuring stations and interpolating to a regular grid using a method specifically designed for meteorological purposes.

Among the different forms of agricultural damage, drought poses a remarkably high risk. According to the data of the Hungarian Agricultural Risk Management System, the amount of contribution paid by members hardly changed in the period 2016–2020, while the amount of compensation paid steadily increased (however, in 2017 the eligibility criteria for payments changed, with the decrease in yield value being considered at crop level instead of at farm level). Drought mitigation payments accounted for 27.5–50.7% of the total payments, except the wetter year in 2016. In 2019–2020, the value of the drought mitigation payments exceeded the total value of contributions paid (*Table 1*).

Table 1. Payments related to drought damage in the period 2016–2020

Indicator	2016	2017	2018	2019	2020
Damage mitigation contribution (million HUF)	4,185	4,167	4,088	4,121	4,145
Total mitigation payment (million HUF)	4,928	7,160	7,608	13,777	18,680
Drought mitigation payment (million HUF)	7,9	1,971	3,858	6,500	7,582
Ratio of the drought mitigation payment to the total (%)	0.2	27.5	50.7	47.2	40.6

Source: own calculations based on the HARMS database

Several studies have focused on agricultural droughts in Hungary based on long-term datasets of temperature, precipitation, or other climate variables. Drought indices (e.g., *Fiala et al.*, 2014; *Mezősi et al.*, 2016) and vegetation indices, like the normalized difference vegetation index (NDVI) (e.g., *Nagy et al.*, 2019; *Szabó et al.*, 2019) are popular tools for revealing drought trends and severity. The present study explores the relationship between drought damage and irrigation, the spatio-temporal distribution of the drought events, and the affected crops based on the 2018–2020 data of the Hungarian Agricultural Risk Management System. In addition, farmers' attitudes towards irrigation as a mitigation tool are examined.

3. Materials and methods

3.1. Datasets

Analyses were based on the HARMS database. The database contains the type of damage, the date and area damaged, the crop, and the decision to accept or reject the damage at parcel level. These data were obtained from the Damage Assessment Workflow Support System operated by the National Food Chain Safety Office (Nébih). The contribution and mitigation payment data were collected and provided by the Hungarian Paying Agency (MÁK) as the responsible authority for these datasets under Pillar 1 of the compensation scheme. The mitigation contributions were available at parcel level, while the mitigation payments were available at farm level, broken down by crop and type of damage. The designation of the parcels as irrigated or non-irrigated was based on farmers' declarations in the single application database. Data on the date and amount of irrigation water used were not available. Although most of the data were available in the database at parcel level, and the parcel geometry is recorded

in the national Land Parcel Information System (LPIS), the latter was not available for us, only larger units, the physical blocks of the LPIS were obtained from the MÁK as shape files.

Most of the irrigated areas are supplied with water through interconnected integrated water supply systems, but irrigation water can also be obtained directly from lakes, reservoirs, and underground wells. Examining the spatial distribution of drought damage, the impact areas of the water supply systems were also considered. Agricultural water is supplied through 68 public irrigation water supply systems. A supply system is generally a large-scale water management and operation unit of the highest order, associated with a main water intake, defined by topography, and connected to a channel system. They are primarily used to meet agricultural water needs, but in many cases also perform other functions, such as the provision of drinking and industrial water, and ecological and recreational water replenishment. The impact areas of these systems are defined by the water management directorates based on technical and water resource management criteria and conditions, which were available in geodata (shape) files.

In addition, monthly and yearly climate reports of the OMSZ were used for the interpretation of the results.

3.2. Methods

The diversity of the analyses carried out required not only several data sources but also different methods and software. The recognized drought affected areas and the areas covered by crops relevant for HARMS were summarized for the LPIS blocks, and the queried data were then appended to the block layers (shape files). Drought-affected blocks in all three years (2018–2020) of the study were selected starting from the 2020 drought layer, from which drought-affected blocks for the other two years were selected (using the Select by Location – Have their centroid in method).

Water supply systems were assigned to blocks based on the largest proportion of their area that overlaps (Spatial join – Largest overlap). One of the supply systems belongs to two water directorates but was treated as one system during the further calculations. The impact areas of these systems vary considerably in size due to technical constraints, and the given boundary is a theoretical line. Therefore, the size of the accepted drought-affected areas was not compared to the size of these impact areas but to the total area of crops relevant for HARMS.

The causes of drought damage on parcels designated as irrigated were investigated by a questionnaire survey. Based on the 2018–2019 data, we selected the HARMS members who had accepted drought damage for their irrigated parcels. The contact details of the members concerned were provided by the MÁK, and farmers were first interviewed by e-mail and then by telephone. The short questionnaire focused on four questions:

- the use of water retention agrotechnical practices,
- taking water requirements into account when selecting the crop species or varieties to be grown,
- the purpose of irrigation,
- the causes of drought damage according to the farmer.

Except for the second question, farmers could check multiple answers from a list and an additional comment was also possible. Another questionnaire survey focused on farmers' current practices and future intentions related to irrigation in Szabolcs-Szatmár-Bereg County, which covers the Nyírség (I/10) and Upper Tisza region (I/6). This survey was carried out in collaboration with the FruitVeb Hungarian Interprofessional Organization for Fruit and Vegetables.

For simple calculations and diagrams, we used Microsoft Excel. Database management and queries were done in a PostgreSQL database, while ArcGIS Desktop was used for geospatial analysis and map visualization.

4. Results

4.1. Spatial distribution of the accepted drought damages

The majority of the 76,201 hectares accepted drought-affected area in 2018 fell in the Nyírség (I/10) and Upper Tisza region (I/6), additionally in the Danube–Tisza interfluve (I/2) (see *Fig. 1* for the numbers of the regions). The drought was more widespread in space and time in 2019 (138,928 ha), and significantly affected the Bácska Plain (I/3), the Körös–Maros interfluve (I/13), the Central Tisza region (I/7), and the Nyírség (I/10), as well as the Small Hungarian Plain (II). The 243,371 hectares of accepted drought-affected area in 2020 were 1.8 times higher than in the previous year and more than three times higher than in 2018. As in the previous year, the drought affected a large area of the Körös-Maros interfluve (I/13), the Central Tisza region (I/7), and the Nyírség (I/10), and covered most of the Small Hungarian Plain (II) (*Fig. 2*).

In all three years, the damaged areas were typically outside the impact areas of the water supply systems (89%, 70%, and 77% over the years) or on parcels covered by water supply systems but designated by farmers as non-irrigated (99%, 95%, and 97%). Areas, where accepted drought damage occurred in all three years were mainly located in the Nyírség (I/10), the Upper Tisza region (I/6), the Central Tisza region (I/7), and the Bácska Plain (I/3) (*Fig. 2*). Within the affected physical blocks – mainly due to crop rotation –, not always the same parcels were damaged.

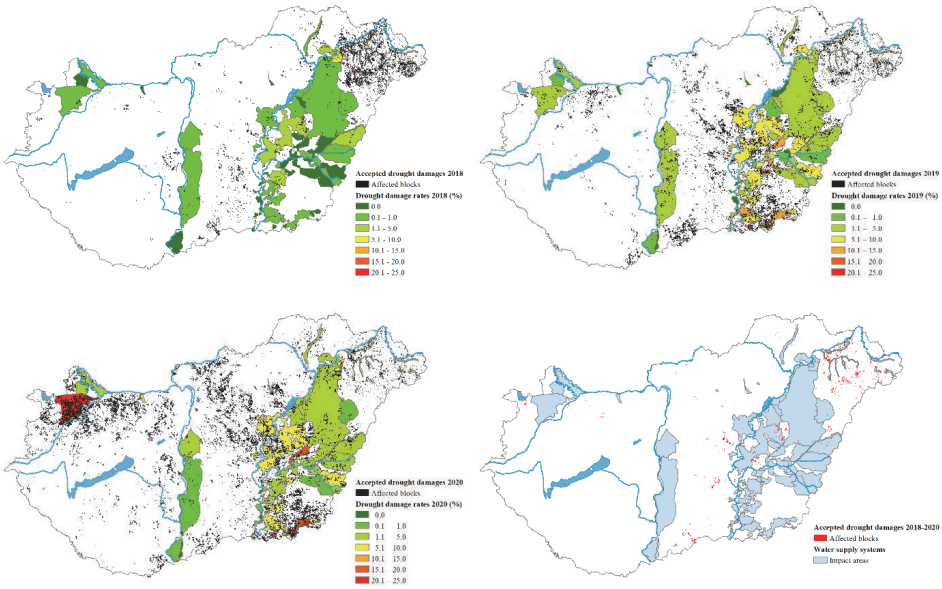

Fig. 2. The water supply systems and the spatial distribution of the accepted drought damages. *Source:* own calculations based on the HARMS database.

The impact areas of the water supply systems vary considerably in size (from 160 hectares to 343.5 thousand hectares) due to technical constraints. Therefore, for each supply system, the size of the accepted drought-affected areas was compared to the total area of crops relevant for HARMS.

In the less drought-prone 2018, 32 of the 67 water supply systems (48%) did not contain any accepted drought-affected area. There were five supply systems with more than 10% of accepted drought areas. These were small water supply systems in Nyírség (I/10) and Upper Tisza region (I/6), with a total of about 3,200 hectares of accepted drought area, of which only 2.5 hectares were on parcels marked as irrigated.

In the drier year 2019, the proportion of accepted claims also increased in areas covered by water supply systems. Of the 67 supply systems, only 12 (18%) had no drought-affected areas accepted, and the number of those with damage rates above 10% increased to eight. These were typically located in the Central Tisza region (I/7) and the south part of the Körös-Maros interfluve (I/13), with a total of almost 7,800 hectares of accepted drought area, of which 423 hectares were on parcels marked as irrigated. For a small supply system, the percentage of accepted drought-affected areas (581 ha) was slightly above 20%, but only non-irrigated parcels were damaged.

Owing to the most extensive drought in 2020, only seven small water supply systems did not contain accepted drought areas. As in the previous year, the 687 hectares damaged in the south part of the Körös-Maros interfluve had the highest percentage of damage (almost 25%), but only non-irrigated areas were damaged. With almost the same proportion (23%), however, more than 13,000 hectares were affected for one of the supply systems in the Small Hungarian Plain (II), but only 57 ha of this area was designated as irrigated. For other supply systems with a higher percentage of accepted damage (15–17%), all the damaged parcels were non-irrigated.

A significant difference is that in the years examined, accepted drought damage affected 35–43% of the non-irrigated areas, while 9–22% of the areas were marked as irrigated.

4.2. Crops affected by drought damage

In the years examined, drought damage showed different patterns, not only in spatial but also in temporal distribution, and these were closely linked to the crops damaged. Owing to cereals being sown in the autumn, the compensation year runs from November 1 of the preceding year to October 31 of the actual year. *Fig. 3* illustrates the temporal distribution of accepted drought areas and the main crops affected, broken down by month. Mitigation payments were paid for more than 100 crops in each year examined (for 106 in 2018, for 115 in 2019, and for 114 in 2020). For the total area, crops with over 500 hectares of damage have been highlighted, while for the irrigated areas, the threshold was 50 hectares. The damaged crops shown in *Fig. 3* reflect the periods of critical water demand for these crops (e.g., May-June for winter cereals, June-August for maize).

According to meteorological data, in 2018, the monthly mean temperature was higher than the 1981–2010 average in every month except February and March. The 4.8 °C difference in April was prominent, but the average temperature in May was also 3.1 °C higher. Precipitation in February and March was more than twice the multi-year average, and in June it was also above average (+35%), except in the eastern part of the country. However, in the other months of the year, there was a lack of rainfall, especially in April and October (37% and 42% less than the long-term average, respectively). Based on the damage events, the lack of rainfall in April was probably compensated by the earlier surplus of rainfall. More than half of the accepted drought areas were reported in August, when several crop species were severely affected by the drought. The October rainfall deficit was reflected in damage to winter cereals and rapeseed in November. The monthly mean temperature in 2019 was above the 1981–2010 average in all months except May. During the year, highest rainfall occurred in May and November, while March was extremely dry, with only 28% of the long-term average. More than 40% of the accepted drought areas were declared in April and mainly affected winter cereals, rapeseed, and lucerne.

As in the previous year, the monthly mean temperature in 2020 was higher than the long-term average in every month except May. The total annual precipitation was slightly higher than the long-term average (102%), but very unevenly distributed. During the year, June and October received outstandingly high rainfall, while April and November were extremely dry. In April, only 25% of the normal rainfall fell, and 54% in May. There were stations where no measurable rainfall fell during the whole month of April. Accordingly, over 61% of the accepted drought-affected areas were declared in May and nearly 25% in June. The drought damage in May affected a particularly large number of crops, with 20 crops having an accepted damage above 500 hectares.

The temporal distribution of the accepted drought damage in the areas designated as irrigated (*Fig. 3*) was essentially similar to that for all damaged areas, with some differences. Overall, the greatest damaged area for apple and Virginia tobacco in 2018 was in August, while the greatest damaged area designated as irrigated was in September. As most of the area under maize, sunflower, lucerne and soybean was non-irrigated, that significantly influenced the temporal distribution of drought damage. A smaller change can be seen in spring for green peas, which was affected by drought over a large area for both irrigated and non-irrigated parcels, but the damage was more severe in May than in the wetter June. The differences seen in July 2019 and August 2020 are due to damage to irrigated hybrid maize.

However, for agricultural risk management, not only the size of the damaged area should be considered, but also the yield loss and the value of the crop affected by the damage event (loss of production value). As a result, the value of the mitigation payment will be in many cases higher for a crop with a high value but smaller area damaged than for a crop with a larger area damaged but a lower price. Therefore, different crops may be considered the most drought-affected according to the accepted drought area, the paid area, and the value of the mitigation payment (*Table 2*). For example, in 2019, hybrid maize was not in the top ten in terms of drought area, while it was ranked fourth in terms of the value of the compensation paid. However, maize and sunflowers, whose critical water demand is in summer, as well as winter cereals and rapeseed, whose critical period is in May-June and which are cultivated over large areas, have been in the top ten in all aspects every year.

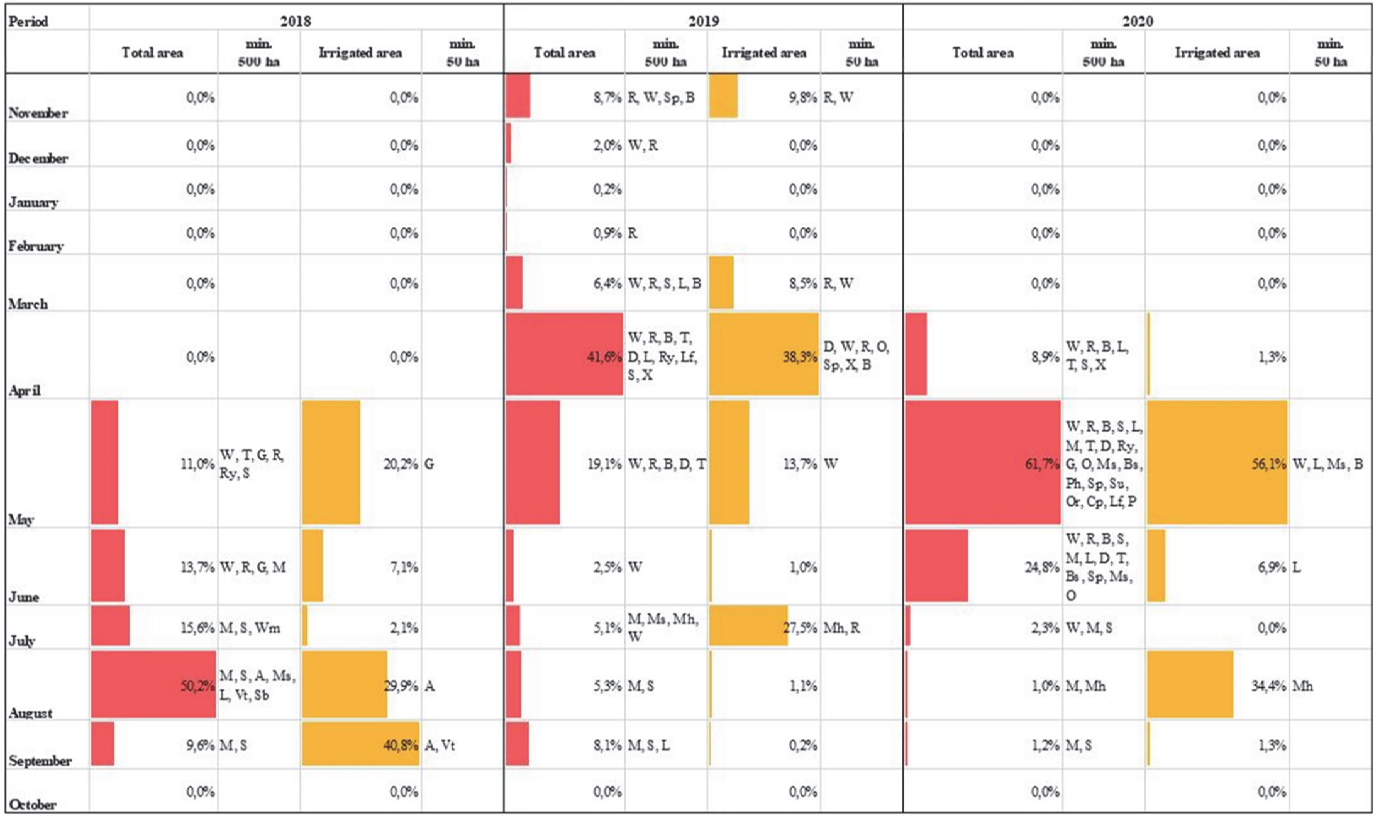

Fig. 3. Temporal distribution of accepted drought areas and the main crops affected. A - apple, B - winter barley, Bs - spring barley, Cp - purple clover, D - winter durum wheat, G -green peas, L - lucerne, Lf - lucerne fermented fodder, M - maize, Mh - hybrid maize, Ms - silage maize, O - oat, Or - oil radish, P - poppy, Ph - phacelia, R - rapeseed, Ry - rye, S - sunflower, Sb - soybean, Sp - spelt, Su - sugar beet, T - winter triticale, Vt - Virginia tobacco, W - winter wheat, Wm - watermelon, X - mixed culture. *Source:* own calculations based on the HARMS database

Table 2. Ranking of drought-affected crops according to the accepted drought area and the mitigation payment

2018		2019		2020	
Accepted drought area	**Mitigation payment**	**Accepted drought area**	**Mitigation payment**	**Accepted drought area**	**Mitigation payment**
Maize	Maize	Winter wheat	Rapeseed	Winter wheat	Winter wheat
Sunflower	Sunflower	Rapeseed	Winter wheat	Rapeseed	Rapeseed
Winter wheat	Green peas	Maize	Maize	Winter barley	Sunflower
Apple	Apple	Winter barley	Hybrid maize	Sunflower	Maize
Rapeseed	Watermelon	Winter triticale	Sunflower	Maize	Hybrid maize

Source: calculations based on the HARMS database

Of the more than 100 crops affected by drought mitigation payments, 8–12 crops were associated with payments of more than HUF 100 million, covering 70–80% of the payments, depending on the year. Crops damaged on irrigated fields (e.g., green peas, Virginia tobacco) generally have higher value and price, therefore drought mitigation payments per hectare were much higher than in non-irrigated areas.

Owing to eligibility criteria, slightly more than half of the members who reported drought damage received mitigation payment, but for them, the value of compensation payment significantly (23–31 times) exceeded the mitigation contribution they paid.

4.3. Causes of drought damage on irrigated fields

Based on the 2018–2019 data, 74 farms were identified having drought damage on parcels designated as irrigated, two of which suffered damage in both years. The causes of the damage were investigated by a questionnaire survey. Most farms had one or two damaged crops, but some of them reported drought damage for eight crops marked as irrigated. Some members responded separately for the different crops, resulting in 50 responses from 48 respondents. Of the responses, 70% were related to arable crops and 30% to orchards. Among the cases examined, the damage to apple and Virginia tobacco was prominent in 2018 in terms of the number of members affected as well as the area damaged, while in 2019, most responses were related to winter wheat and rapeseed (according to the results shown in *Fig. 3*). In the followings, we describe the farmers' attitudes toward irrigation and the causes of drought damage according to the farmers.

Most of the respondents use some water retention practices. Of the technologies surveyed, soil loosening is widespread among arable farmers (field

crops and field vegetables) but is also used by 20% of responding fruit growers. The use of cover crops and bacterial fertilization were mentioned by almost one third of arable farmers, while the use of cover crops was more common for fruit growers (40%). Other technologies applied included the use of organic fertilizers, as well as shoot-sorting in apple orchards.

Of the respondents, 66% consider the water needs of plants when choosing a plant species or variety. This figure is even higher among arable farmers, where the crop is rotated annually (71%), and slightly lower for longer lifespan orchards. Fruit growing is a special case, where the characteristics of the trees are determined by the combination of the rootstock and the grafted variety. Another problem for apple growers was that when the plantation was established, the weather was not so drought-prone, so this was not a factor in the choice of species.

Most respondents (72%) use irrigation primarily for crop safety, followed by the need to achieve higher yields, which accounted for nearly 50% of all responses, and 80% of fruit growers. Most of the winter wheat growers irrigate occasionally to reduce damage. Additional purposes of irrigation are typical of fruit growers, such as fertilization, in some cases frost prevention or achieving a more uniform fruit size.

Farmers were allowed to provide multiple answers for the effective reasons of drought damage. Of the respondents, 28% indicated that no irrigation had taken place on the field marked as irrigated, but this proportion was slightly higher among arable crop producers (31%) and lower among fruit growers (20%) (*Fig. 4*). In some cases, this was due to a technical problem (e.g., pump failure), in others it was considered that the crop was not worth irrigating – these were generally listed among the other reasons. Among the offered responses, the indications of damage in sensitive phenophase were prominent (51% for arable land and 47% for orchards), while the lack of available water, as a limiting factor, was mentioned by fewer than 15% of respondents.

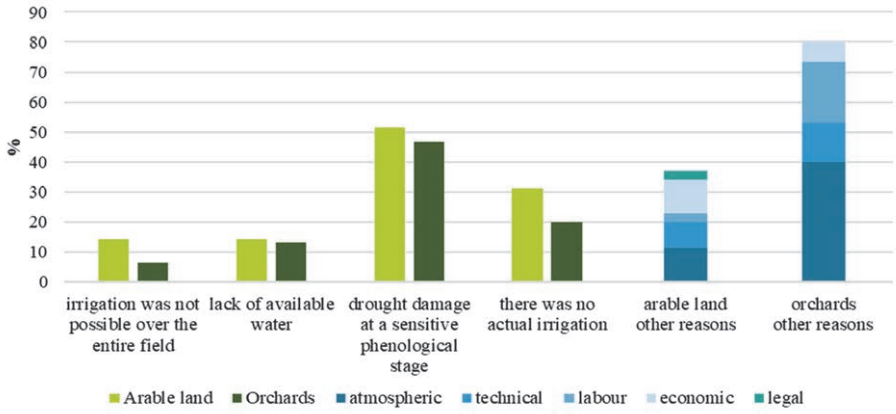

Fig. 4. Causes of drought damage on irrigated fields. *Source:* questionnaire survey.

For this question, farmers had more freedom to give answers other than the few pre-defined options. Half of the respondents took the opportunity to mention other reasons, which were particularly high (80%) among fruit growers. For an easier overview, the answers were grouped into atmospheric, technical (failure, outdated system), economic (operating costs, irrigate something else), labor (lack of labor and/or time), and legal (irrigation period) reasons (*Fig. 4*). There was a high prevalence of atmospheric drought, particularly among fruit growers using drip irrigation and vegetable growers in arable fields. Drip irrigation is not suitable for humidification and, especially in the case of prolonged drought and associated winds, the low humidity in the air will dry out the leaves of the plants despite irrigation. Other reasons mentioned repeatedly included lack of available labor and working time for winding drums and for old pumps requiring supervision. For crops damaged in autumn 2018 (winter cereals, rapeseed, poppy), some mentioned that the dry period fell outside the statutory irrigation season (from 2019 the irrigation season ran from 1 March to 31 October, previously from 15 April to 30 September), therefore they did not irrigate. Off-season irrigation is possible at an extra cost in consultation with the water supplier, but farmers usually do not undertake this. Those with little water available preferred to irrigate other, more water-intensive crops (e.g., vegetables instead of the old orchard) or could only irrigate intermittently. Thus, in several cases, these respondents also indicated that they were unable to irrigate the entire field.

4.4. Farmers' irrigation practices and plans in Szabolcs-Szatmár-Bereg County

Based on the spatial distribution of drought events (*Fig. 2*), Szabolcs-Szatmár-Bereg County, which covers the Nyírség (I/10) and the Upper Tisza region (I/6), was one of the 'hotspot' areas in the years examined. As this is the main fruit-growing region in Hungary, a questionnaire survey focused on current irrigation practices of orchards and farmers' attitudes towards sustainable irrigation development.

A total of 106 fruit growers participated in the survey, whose orchard area covered 7.4% of the total fruit-growing area of the county. More than half (58%) of the growers have irrigation equipment in their orchards. The main irrigated cultures are walnuts, apples, and sour cherries, with a share of irrigated areas above 60%; in addition, plums, cherries, pears, and quince with shares of irrigated areas of 30–40%. However, based on the responses, illegal irrigation (without water licenses) of commercial orchards is estimated at 20–30%. Orchards are irrigated mainly from groundwater (59% from stratum water and 20% from subsoil water), 19% of the areas are irrigated from reservoirs, and only 2% from surface water. The high percentage of stratum water use is unfavorable, because its recharge is much slower than that of subsoil water and raises both water quantity and quality issues. Of the irrigated orchards, 90% are equipped with a

water-saving drip system, and most of them (71%) are also suitable for fertilization.

Of the fruit growers who irrigate, 88% have a simple cylindrical rain gauge. Meteorological stations are used by 27% of the growers, while 23% use tensiometers to measure soil moisture. Almost half of them (46%) have also installed water purification units for their irrigation system, while only 23% use irrigation management software. Most of the respondents (89%) do not currently contact an irrigation advisor, and 34% do not plan to do so in the future. All these responses show that irrigation is more based on growers' experience and tradition rather than on objective measurements and control systems.

The limited water supply, the actual status of water bodies, and the protection of groundwater require a change in irrigation practices in the region. Therefore, fruit growers were also asked about their attitudes towards sustainable irrigation management. The vast majority (97%) of the respondents consider irrigation development important and would use water-saving technologies to reduce irrigation restrictions. Almost the same proportion (94%) would use conservation tillage methods, many of them would change to use surface water instead of groundwater (if made available through irrigation development), support or develop the construction of dual-function canals (inland drainage and irrigation) on their field, and would undertake the construction of reservoirs. The willingness to establish irrigation communities is lower than in other instruments, although Hungary now strongly supports this form of cooperation. Respondents are divided on the reuse of wastewater for irrigation purposes (*Fig. 5*).

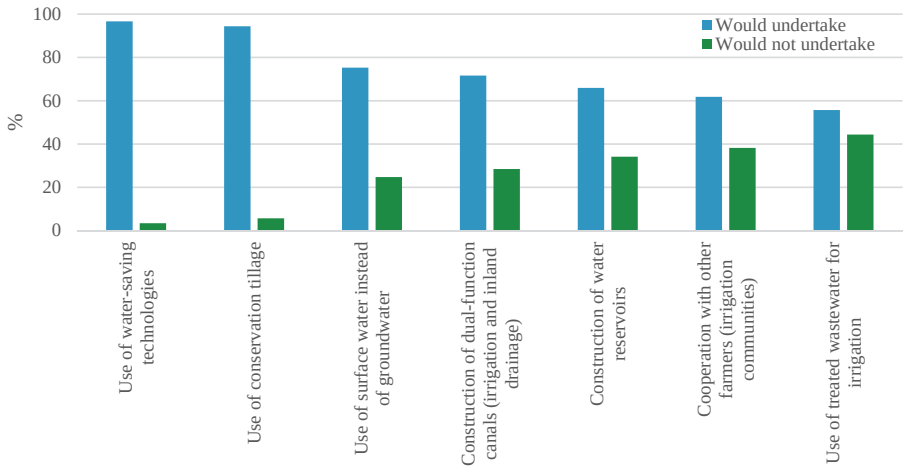

Fig. 5. Attitudes to manage limited irrigation possibilities (number of respondents is 89).
Source: questionnaire survey.

Most of the respondents (73%) plan some irrigation development (e.g., irrigation well, irrigation equipment, meteorological station, fertilizer unit, soil moisture meter) in the next five years, and more than half of them would require investment support for that purpose. The survey shows that farmers are trying to make water use in their area as efficient as possible with sustainable tools.

5. Discussion

Agriculture is one of the most important sectors in Hungary, therefore, agricultural drought events are a particularly important area to be examined. A significant share of Hungarian agricultural land is already considered to be affected by drought (*Kemény et al*., 2018) and most farmers experienced now reduced productivity due to drought periods (*Biró et al*., 2021). In addition, climate models predict a decrease in precipitation and an increase in the frequency and duration of droughts (*Mezősi et al.*, 2016; *Lakatos* and *Zsebeházi*, 2018). One of the main problems of studying drought is its delimitation in space, time, and intensity (*Tamás*, 2017). The present study was based on the 2018–2020 data of the Hungarian Agricultural Risk Management System, and accepted drought-affected parcels were analyzed. Drought damage showed different patterns, not only in spatial but also in temporal distribution, and these were closely linked to the crops damaged. The economic value of drought damage and the mitigation payment depends on the price of the crop. Therefore, different crops may be considered the most drought-affected according to the accepted drought area, the paid area, and the value of the mitigation payment.

Farming systems may play a fundamental role in the adaptation to adverse climatic conditions. Among the adaptation options, changes in crop species, cultivar, sowing date, fertilization, irrigation, use of cover crops, conservation tillage, and precision agriculture technologies seem to be the most appropriate. *Mitter et al*. (2019) found that adaptation intentions are only formed if farmers are aware of effective adaptation measures, accept personal responsibility for their farms, and evaluate adaptation costs positively. According to *Hanger-Kopp* and *Palka* (2021), whether a farmer irrigates or not partly depends on whether water for irrigation and the associated water rights are available. In Hungary, farmers often complain about the lengthy and difficult authorization procedure and the associated high costs. The water licenses are underexploited; only around the half of the potentially irrigable land is irrigated. Crops that are regularly and extensively damaged (e.g., maize, sunflower, and winter cereals) are mainly rain-fed. To avoid drought damage, a proactive approach should be pursued, such as increasing soil water retention capacity, increased groundwater storage, improvement of irrigation techniques, investment in water-saving technologies, and improvements in water supply (*Musolino et al*., 2018; *Vogt et al*., 2018). The results showed that irrigated areas have a lower rate of drought damage than non-

irrigated areas, demonstrating that irrigation can be an effective drought mitigation tool. Most of the damaged areas were outside the impact areas of the water supply systems, or on parcels covered by water supply systems but designated by farmers as non-irrigated. Based on the questionnaire survey, most of the respondents use irrigation primarily for crop safety. However, planned irrigation management not only mitigates the adverse effects of extreme weather anomalies and reduces yield variability, but can also increase yields and, in most cases, improve product quality. Most of the agricultural experts agree that the increase of irrigated areas could provide a huge potential for field crop production in Hungary (*Kemény et al*., 2018). According to other experts, irrigation is primarily justified when and where other agrotechnological means cannot provide the necessary water for the crops (*Kolossváry*, 2021). Our surveys show that most of the farmers consider the water needs of plants when choosing a plant species or variety, many of them use some water retention practices and are open to use new solutions to manage limited irrigation possibilities. It should be highlighted that the water-saving drip irrigation is not suitable for humidification, and therefore, against prolonged atmospheric drought. This is a serious problem for fruit and vegetable growers.

Hanger-Kopp and *Palka* (2021) found that farmers consider irrigation a strenuous and tedious job, and equipment needs regular checks, therefore, the location (i.e., whether they are close together) and size of the fields may also influence the adoption of irrigation. Technical problems (e.g., pump failure, outdated system), as well as lack of available labor and working time for winding drums and for supervising old pumps were also mentioned by farmers responding the causes of drought damage on irrigated fields. The other survey revealed that automation and use of irrigation management software is not widespread, only 23% of the respondents use it.

Adaptation to climate change is one of the critical points of the long-term sustainability of Hungarian agriculture. According to *Trnka et al*. (2022), to influence the strategic decisions of the farmers positive incentives are needed rather than regulations. The compensation paid through the risk management system is a great help for the farmers, but farmers should be encouraged to invest in preparedness and private insurance instead of the risk and ex-post damage compensation (*Leitner et al*., 2020). Sustainable water management would require the spread of new technologies and digitalization. *Biró et al*., (2021) emphasized that it is necessary to bring technological developments closer to farmers, support them in sustainable innovation investments and practical application. They identified 27 Climate-Smart Agriculture tools, which may strengthen environmental sustainability, among them the drought monitoring system and water-saving smart irrigation systems. *Zubor-Nemes* (2021) analyzed the relationship between crop insurance take-up, technical efficiency, and investment in Hungarian farming. According to her results, total subsidies (including direct payments) decrease technical efficiency, while targeted subsidies, i.e., premium

support, encourage crop insurance demand, and investment subsidies stimulate investment significantly. Financial support to help farmers invest in climate-smart practices and technologies is considered important, and there are now such investment support schemes in Hungary (e.g., support for precision agriculture and for irrigation development).

Information about the drought-vulnerable areas and analyses of drought impact on agriculture are crucial to adapt agricultural practices to the weather extremes. Such information will potentially help to adapt irrigation and land management strategies, application of any drought management measures (*Crocetti et al*., 2020; *Drisya* and *Sathish Kumar,* 2022), as well as to establish adequate insurance and mitigation policies. Owing to the different vulnerability and adaptive capacity of different regions, impacts and problems should also be managed in a differentiated way, with customized solutions based on each area and its capabilities. *Buzási et al*. (2021) developed an indicator that categorizes the Hungarian counties based on their drought-related exposure (relative Pálfai drought index), sensitivity (topsoil sand content), and adaptability (irrigation water use). Their results showed that many counties are not adequately prepared for the impacts of drought, despite their high vulnerability index. They found that the drought vulnerability of Szabolcs-Szatmár-Bereg County is in the top quartile, but the county's strategy considers drought in a typical forward-looking response. Our results confirm that this county should receive special attention. This area suffered significant drought damage in the years examined, and the impact area of the surface water-based supply systems is small. The biggest problem in the county is the excessive stratum water use. Reducing the wasteful use of groundwater and protecting the status of aquifers are important to ensure that drinking water needs are met in the long term. The protection of aquifers is not only quantitative but also has a water quality issue, preventing the flow of locally contaminated groundwater into deeper layers. Therefore, only micro-irrigation from stratum water should be allowed.

6. Conclusions

Among the different forms of agricultural damage in Hungary, drought poses a remarkably high risk. In the years examined, drought mitigation payments accounted for 40.6–50.7% of the total payments. In 2019–2020, the value of the drought mitigation payments exceeded the total value of the contributions paid by farmers. The National Water Strategy (Jenő Kvassay Plan) also draws attention to the fact that a substantial proportion of agricultural subsidies is spent on compensation, rather than on more efficient irrigation, which would generate higher revenues and make better use of the water supply (*Reich,* 2019). The current risk management system contributes to mitigating the damage caused by extreme weather events but does not encourage farmers to mitigate risk. The risk

management system should be modified to transform it into a preventive system, which encourages farmers to use water retentive soil cultivation methods, appropriate cropping systems, sustainable water management, and efficient and reasonable levels of irrigation. Accordingly, fewer mitigation benefits would be paid through less drought damage. Currently, annual membership contributions are calculated per area unit, but it is recommended to examine whether the amount of contribution may take into account the drought sensitivity of the given area, and the irrigation and water retention agrotechnical practices used by the farmer. Investigations in this direction have started at Institute of Agricultural Economics. In addition to the financial support (subsidized insurance, ex-post damage compensation, investment support), irrigation advisory and knowledge management should be strengthened.

Several initiatives, projects and online tools have been established to facilitate drought monitoring and management in the Pannonian Basin (*Gregorič et al*., 2019; *Nagy et al.*, 2019, *Szabó et al.*, 2019; *Crocetti et al*., 2020). The Hungarian Agricultural Risk Management System is based on its own drought definition and the measurements of the OMSZ. However, the OVF has also established a national drought management monitoring system and developed the Hungarian Drought Index. The main purpose of this system is to determine intervention levels and to define precisely the operational activities and related measures for legislative harmonization. Additionally, data are published on a web portal, delivering information for decision makers, professionals, or farmers (*Fiala et al*., 2018). However, different methodologies show different results, and it would be beneficial to synthesize the research results and create a national drought risk map.

Acknowledgements: The research presented in this paper was supported by the Hungarian Ministry of Agriculture. We are grateful to the FruitVeB Hungarian Interprofessional Organization for Fruit and Vegetables for the collaboration in the survey.

References

Alsafadi, K., Mohammed, S.S., Ayugi, B., Sharaf, M., and *Harsányi, E.*, 2020: Spatial-Temporal Evolution of Drought Characteristics Over Hungary Between 1961 and 2010. *Pure Appl. Geophys. 177*, 3961–3978. https://doi.org/10.1007/s00024-020-02449-5

Antal, J., Berzsenyi, Z., Birkás, M., Bocz, E., Csík, L., et al., 2005: Növénytermesztéstan 1. Mezőgazda Kiadó, Budapest. (In Hungarian)

Berényi, A., Pongrácz, R., and *Bartholy, J*., 2021: Csapadékszélsőségek változása Európa déli alföldi régióiban az 1951–2019 időszakban [Changes in extreme precipitation patterns in the southern lowland regions of Europe during the 1951–2019 period]. *Modern Geográfia 16*(4), 58–101. (In Hungarian) https://doi.org/10.15170/MG.2021.16.04.05

Biró, K., Szalmáné Csete, M., and *Németh, B.*, 2021: Climate-Smart Agriculture: Sleeping Beauty of the Hungarian Agribusiness*. Sustainability 13*(18), 10269. https://doi.org/10.3390/su131810269

Blanka, V., Mezősi, G., and *Meyer, B.*, 2013: Projected changes in the drought hazard in Hungary due to climate change. Időjárás 117(2), 219–237.

Blauhut, V., Stoelzle, M., Ahopelto, L., Brunner. M.I., Teutschbein, C., et al., 2021: Lessons from the 2018–2019 European droughts: A collective need for unifying drought risk management, *Nat. Hazards Earth Syst. Sci. Discuss.* [preprinthttps://doi.org/10.5194/nhess-2021-276

Buzási, A., Pálvölgyi, T., and *Esses, D.*, 2021: Drought-related vulnerability and its policy implications in Hungary. *Mitig. Adapt. Strateg. Glob. Change. 26*,11. https://doi.org/10.1007/s11027-021-09943-8

Cammalleri, C., Naumann, G., Mentaschi, L., Formetta, G., Forzieri, G. et al., 2020: Global warming and drought impacts in the EU. JRC PESETA IV project – Task 7. https://doi.org/10.2760/597045 29

Crocetti, L., Forkel, M., Fischer, M., Jurečka, F., Grlj, A., et al., 2020: Earth Observation for agricultural drought monitoring in the Pannonian Basin (southeastern Europe): current state and future directions. *Reg. Env. Change 20*, 123. https://doi.org/10.1007/s10113-020-01710-w

Drisya, J. and *Sathish Kumar, D.*, 2022: Evaluation of the drought management measures in a semi-arid agricultural watershed. *Environ Dev Sustain 25*, 811–833. https://doi.org/10.1007/s10668-021-02079-4

EC, 2021: Forging a climate-resilient Europe – the new EU Strategy on Adaptation to Climate Change. COM(2021) 82 final

EDO, 2020: Drought in Europe – June 2020. *EDO* Analytical Report. JRC European Drought Observatory (EDO). Accessed 17 February 2022 https://edo.jrc.ec.europa.eu/documents/news/EDODroughtNews202006_Europe.pdf

Eurostat, 2019: Agri-environmental indicator – irrigation. Statistics Explained 16/04/2019. https://ec.europa.eu/eurostat/statistics-explained/pdfscache/14965.pdf

Fiala, K., Blanka, V., Ladányi, Z., Szilassi, P., Benyhe, B., et al., 2014: Drought severity and its effect on agricultural production in the Hungarian-Serbian cross-border area. *J. Environ. Geography 7(3-4)*, 43–51. https://doi.org/10.2478/jengeo-2014-0011

Fiala, K., Barta, K., Benyhe, B., Fehérváry, I., Láng, I., et al., 2018: Development of an Operational Drought and Water Scarcity Monitoring System in Hungary. GWP. Accessed 17 February 2022 https://www.gwp.org/globalassets/global/gwp-cee_files/idmp-cee/idmp-drought-monitoring-hungary.pdf

Gregorič, G., Moderc, A., Sušnik, A., Žun, M., (2019) Better prepared for drought – Danube drought strategy. Slovenian Environment Agency, Ljubljana, Slovenia

GWP (2019) How to Communicate Drought. A guide by the Integrated Drought Management Programme in Central and Eastern Europe. GWP EE. https://www.gwp.org/globalassets/global/gwp-cee_files/idmp-cee/how-to-communicate-drought-guide.pdf Accessed 18 March 2022

Hanger-Kopp, S. and *Palka, M.*, 2021: Decision spaces in agricultural risk management: a mental model study of Austrian crop farmers. *Environ. Dev. Sustain. 24*, 6072–6098. https://doi.org/10.1007/s10668-021-01693-6

Hari, V., Rakovec, O., Markonis, Y., Hanel, M., and *Kumar, R.*, 2020: Increased future occurrences of the exceptional 2018–2019 Central European drought under global warming. *Sci. Rep. 10*, 12207. https://doi.org/10.1038/s41598-020-68872-9

IPCC, 2021: Summary for Policymakers. In: Climate Change 2021: The Physical Science Basis. Contribution of Working Group I to the Sixth Assessment Report of the Intergovernmental Panel on Climate Change [(eds. *Masson-Delmotte, V., Zhai, P., Pirani, A., Connors, S.L., Péan, C. et al.*)

Jaagus, J., Aasa, A., Aniskevich, S., Boincean, B., Bojariu, R., et al., 2021: Long-term changes in drought indices in eastern and central Europe. Int. J. Climatol. 42, 225–249. https://doi.org/10.1002/joc.7241

Kemény, G., Lámfalusi, I., Molnár, A., (eds) 2018: Az öntözhetőség természeti-gazdasági korlátainak hatása az öntözhető területekre [An assessment of the potential for increasing the irrigated area in Hungary as determined by natural and economic constraints]. AKI, Budapest. (In Hungarian) http://repo.aki.gov.hu/3153

KSH, 2021: Land area of Hungary by land use categories. Accessed 21 February 2022. https://www.ksh.hu/stadat_files/mez/en/mez0008.html

Kolossváry, G., 2021: A mezőgazdaság és a rendelkezésre álló víz – az öntözés és a természetvédelem konfliktusa [Agriculture and available water – the conflict between irrigation and nature conservation]. *Hidrológiai Közlöny 101*, 55–60. (In Hungarian)

Lakatos, M. and *Bihari, Z.*, 2011: A közelmúlt megfigyelt hőmérsékleti- és csapadéktendenciái. In (eds. *Batholy, J., Bozó, L., Haszpra, L.*) Klímaváltozás – 2011: Klímaszcenáriók a Kárpátmedence térségére. MTA and ELTE Meteorológiai Tanszék, Budapest. 146–169. (In Hungarian)

Lakatos, M., Bihari, Z., Szentimrey, T., Spinoni, J., and *Szalai, S.*, 2016: Analyses of temperature extremes in the Carpathian Region in the period 1961–2010. *Időjárás 120*, 41–51.

Lakatos, M. and *Zsebeházi, G.* 2018: Az éghajlat megfigyelt tendenciái és várható alakulása Magyarországon. In: (eds. *Ságri Zs, Pál K.*) Mérsékelt öv? Felelős cselekvési irányok a hatékony klímavédelemért, Klímabarát Települések Szövetsége, Budapest. 31–49. (In Hungarian) http://klimabarat.sreter.eu/images/kiadvany/kotet.pdf

Lámfalusi, I. and *Péter, K.* (eds) 2021: A mezőgazdasági kockázatkezelési rendszer működésének értékelése 2020 [Evaluation of the operation of the agricultural risk management system, 2020]. AKI, Budapest. (In Hungarian)

Leitner, M., Babcicky, P., Schinko, T., and *Glas, N.*, 2020: The status of Climate Risk Management in Austria. Assessing the governance landscape and proposing ways forward for comprehensively managing flood and drought risk. *Clim. Risk Manage. 30*, 100246. https://doi.org/10.1016/j.crm.2020.100246

Mezősi, G., Blanka, V., Ladányi, Z., Bata, T., Urdea, P., et al., 2016: Expected mid-and long-term changes in drought hazard for the South-Eastern Carpathian Basin. *Carpathian J. Earth Environ. Sci. 11*, 355–366.

Mitter, H., Larcher, M., Schönhart, M., Stöttinger, M., and *Schmid, E*. 2019: Exploring Farmers' Climate Change Perceptions and Adaptation Intentions: Empirical Evidence from Austria. *Environ. Manage. 63*, 804–821. https://doi.org/10.1007/s00267-019-01158-7

Musolino, D.A., Massarutto, A., and *de Carli, A.* 2018: Does drought always cause economic losses in agriculture? An empirical investigation on the distributive effects of drought events in some areas of Southern Europe. *Sci. Total Environ. 633*, 1560–1570. https://doi.org/10.1016/j.scitotenv.2018.02.308

Mutua Ndue, K. and *Goda, P*., 2021: Multidimensional assessment of European agricultural sector adaptation to climate change. *Stud. Agric. Econ. 123*, 8–22. https://doi.org/10.7896/j.2095

Nagy, A., Tamás, J., Szabó, A., Gálya, B., and *Fehér, J.*, 2019: Mezőgazdasági aszály monitoring és aszály előrejelzés távérzékelt adatok alapján a Tisza vízgyűjtőn [Monitoring and prediction of agricultural drought in the Tisza River Basin based on remote sensing data]. *Hidrológiai Közlöny 99*(4):61–68. (In Hungarian)

Reich, Gy., 2019: Nemzeti Vízstratégia (Kvassay Jenő terv). Nemzeti Közszolgálati Egyetem, Budapest (In Hungarian)

Spinoni, J., Naumann, G., Vogt, J., and *Barbosa, P*., 2016: Meteorological Droughts in Europe: Events and Impacts – Past Trends and Future Projections. Publications Office of the European Union, Luxembourg, EUR 27748 EN. https://doi.org/10.2788/450449

Szabó, Sz., Elemér, L., Kovács, Z., Püspöki, Z., Kertész, Á., et al., 2019: NDVI dynamics as reflected in climatic variables: spatial and temporal trends – a case study of Hungary, *GISci. Remote Sens. 56*, 624–644. https://doi.org/10.1080/15481603.2018.1560686

Tamás, J., 2017: Az aszály. *Magyar Tudomány 178*, 1228–1237. (In Hungarian) https://doi.org/10.1556/2065.178.2017.10.6

Trnka, M., Bartošová, L., Grammatikopoulou, I., Havlík, P., Olesen, J.E., Hlavinka, P., Marek, M.V., Vačkářová, D., Skjelvĺg, A., and *Žalud, Z.*, 2022: The Possibility of Consensus Regarding Climate Change Adaptation Policies in Agriculture and Forestry among Stakeholder Groups in the Czech Republic. *Environ. Manage. 69*, 128–139. https://doi.org/10.1007/s00267-021-01499-2

Vogt, J.V., Naumann, G., Masante, D., Spinoni, J., Cammalleri, C., et al., 2018: Drought Risk Assessment. A conceptual Framework. EUR 29464 EN, Publications Office of the European Union, Luxembourg. https://doi.org/10.2760/057223

Webber, H., Ewert, F., Olesen, J.E., et al., 2018: Diverging importance of drought stress for maize and winter wheat in Europe. *Nat. Commun. 9*, 4249. https://doi.org/10.1038/s41467-018-06525-2

Zubor-Nemes A., 2021 The relationship between crop insurance take-up, technical efficiency, and investment in Hungarian farming. Stud in Agric Econ, 123:122–130. https://doi.org/10.7896/j.2210

DOI:10.28974/idojaras.2023.2.2

IDŐJÁRÁS

Quarterly Journal of the Hungarian Meteorological Service
Vol. 127, No. 2, April – June, 2023, pp. 167–197

Retrieval of atmospheric trace gases from satellite infrared limb sounding data

Shaomin Cai[1], **Weijia Zhang**[2,*],and **Yizhou Zhao**[3]

[1] *School of Medicine, Shaoxing University*
312,000, Zhejiang Province, China

[2] *Shaoxing University*
No.508, Huancheng West Road, Shaoxing 312000, China

[3] *Department of Astronautics*
Nanjing University of Aeronautics and Astronautics
No. 169, Sheng Tai West Road, Nanjing 211106, China

Corresponding author E-mail: zhangw@usx.edu.cn

(Manuscript received in final form June 7, 2022)

Abstract— The Michelson Interferometer for Passive Atmospheric Sounding (MIPAS) instrument which operated in the near-to-mid infrared on the Envisat satellite from 2002–2012 is a Fourier-transform spectrometer for the measurement of high-resolution atmospheric emission spectra at the Earth's limb. The initial operational products are profiles of temperature, H_2O, O_3, CH_4, N_2O, HNO_3, and NO_2, and this list is extended to include the important GHG (greenhouse gases) and ODS (ozone depleting substances) species using MORSE (orbital retrieval processor).

This paper discusses retrievals of minor trace species of HCFC-22, HOCl, OCS, C_2H_6, COF_2, HCN, CF_4, SF_6, and CCl_4. Preliminary zonal mean results of these retrievals are satisfactory except for HCN and CF_4 species. We then use MIPAS to estimate the total F and Cl budget in the atmosphere. Comparisons with SLIMCAT are also discussed, with the results consistent.

Finally, we focus on improving the retrieval method for minor trace species, COF_2, by adjusting correlation length and a priori constraint, as well as the chi-square method introduced to analyze noise. Tests have shown that our improvement could get more information from the measurements.

Key-words: MIPAS, atmospheric trace gases, HCFC-22, SLIMCAT (chemical transport model), chi-square test

1. Introduction

1.1. Ozone depleting sustances, ODS and greenhouse gases, GHG

It is known that the stratospheric fluorine and chlorine both have important effects on the atmosphere, especially the chlorine on the ozone depletion and the fluorine on the long-lived greenhouse gases. Accurate knowledge of the distribution and trends relevant atmospheric trace gases is crucial for the validation of numerical model simulations, which are used to study the climate system. However, until now, not much stratospheric data has been available.

In this study, the measurement of trace gases for the Michelson Interferometer for Passive Atmospheric Sounding (MIPAS) is extended to include the important GHG and ODS species, whose retrieval is challenging using an Oxford-specific state-of-the-art retrieval scheme, known as MORSE. The instrument, MIPAS, is a Fourier-transform spectrometer for the measurement of emission spectra from the Earth's limb operating in the infra-red spectrum region (*Fischer et al.*, 2008). Itwill be introduced in Section 2. With the ESA MICAL processor, the MIPAS L1 dataset has been available since 2019. MORSE is known as MIPAS optimal estimation using sequential estimation, which will be introduced in Section 3.

In this paper, the minor trace species, which will be investigated, are hydrogen cyanide (HCN), carbon tetrafluoride (CF_4), HCFC-22, carbonyl fluoride (COF_2), carbon tetrachloride (CCl_4), sulphur hexafluoride (SF_6), carbonyl sulphide (OCS), hypochlorous acid (HOCl), and ethane (C_2H_6). Concerning these species, work has been done for the retrieval as well as validation of HCN (*Wiegele et al.*, retrieval, 2012; *Glatthor et al.*, 2009), HCFC-22, CCl_4, SF_6, OCS, HOCl (*Clarmann et al.*, 2009) and C_2H_6 (*Wiegele et al.*, 2012; *Glatthor et al.*, 2009).

The preliminary results are presented in Section 4, together with initial validation with the SLIMCAT model. Section 5 establishes the results of the total chlorine and fluorine budgets measured by MIPAS, which including these newly retrieved minor trace species and all the chlorine or fluorine-containing species that have been retrieved using MORSE.

An investigation of improving the COF_2 retrieval has been made in Section 6. Diagnostics and chi-square tests are introduced to analyze the retrievals.

1.2. Trace gases from MIPAS

A brief introduction of the minor trace species retrieved via Oxford MORSE is presented with a summary table, *Table 1*.

Table 1.Basic information of minor trace gases

Species	**Source**	**Sink**	**Tropospheric VMRs [pptv]**	**Stratospheric Lifetime**
HCFC-22	air conditioning, refrigeration (*Domanski*, 1999)	reaction with OH and photolysis (*Midgley* and *Fisher*, 1993)	200 (AGAGE for 2010 March)	12 years (*Reimann et al*., 2013)
CF_4	primary aluminium Production *(Harnisch* and *Eisenhauer*, 1998)	reaction with OH (*Watson et al*., 1992)	78 (AGAGE for March 2010)	25,000-50,000 years (*Zander et al*., 1996)
CCl_4	anthropogenic emission (*Altshuller*,1976)	photolysis (*Helas* and *Wilson*, 1992)	90 (AGAGE for 2010 March)	44 years (*Reimann et al.*, 2013)
OCS	biomass burning (*Notholt et al*., 2003)	dry soil (*Yi et al*., 2008)	520 ±15 (*Mahieu et al*., 2003)	4-5 years (*Mahieu et al*., 2003)
C_2H_6	biomass burning and natural gas emissions (*Rinsland et al*. 2005)	reaction with OH *(Rinsland et al*., 2005)	400 (*Wiegele et al*., 2012)	50 days (*Glatthor et al*., 2009)
COF_2	degradation product of CFCs (*Muhle et al*., 2010)	photolysis (*Sze*, 1978)	150 (*Kaye et al*., 1991)	12 minutes (*McCann et al*., 2000)
HCN	biomass burning (*Singh et al*., 2003)	ocean take up, atmospheric oxidation and photolysis (*Hickson et al*., 2007)	300 (*Tereszchuk et al.*, 2013)	a few years (*Cicerone* and *Zellner*, 1983)
SF_6	anthropogenic emission and natural minerals (*Harnisch* and *Eisenhauer*, 1998)	electron absorption (*Singh et al*., 1977)	7 (AGAGE for 2010 March)	3200 years (*Forster et al*., 2007)
HOCl	reaction of ClO and HO (*Hicksonet al*., 2007)	photolysis (*Hickson et al*., 2007)	150 (*Clarmann et al*., 2009)	1 hour (*Mishalanie et al.*, 1986)

2. The MIPAS Instrument

The Michelson Interferometer for Passive Atmospheric Sounding (MIPAS) is a Fourier-transform spectrometer for the measurement of emission spectra from the Earth's limb (*Fischer et al*., 2008). MIPAS was operated from July 2002 to March 2004 at full spectral resolution (0.025 cm^{-1}) with 17 measurements for a complete limb scan. After numerous interferometer anomalies, it operated at a reduced spectral resolution (0.0625 cm^{-1}) from January 2005 until April 2012, thereby providing 10 years of data of species for investigation. The altitude coverage for the optimized resolution measurement mode, what we used in this study, is 5 to 70 km at the poles and 12 to 77 km,7 km higher at the equator. For a complete limb scan at reduced spectral resolution, the number of measurements increased to 27 with a vertical spacing of approximating 4.5 km at higher altitudes and 15 km at lower altitudes. *Fig. 1* shows a typical day's sampling profile locations, which is useful for studying global climatology. There are 14 orbits within one day's operation, producing large sample of measurements, about 1300 profiles per day. The major instrumental characteristics of MIPAS are summarized in *Table 2.*

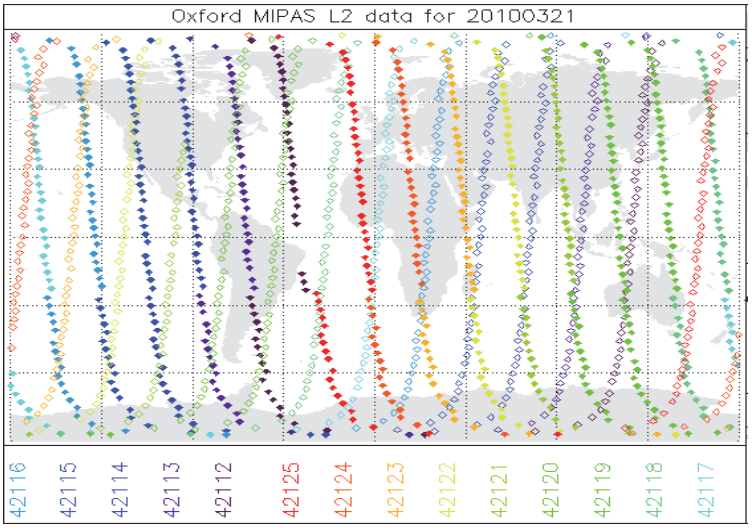

Fig.1. One day's sampling profile locations on March 21, 2010. Different colours represent different orbits with the number list below, while symbols are profile locations. Open symbols represent daytime measurements while solid symbols are nighttime measurements.(Source from http://www.atm.ox.ac.uk/group/mipas/L2OXF/20100321/)

Table 2. MIPAS instrumental characteristics

Spectral range	685 – 2410 cm^{-1} (infrared)
OR mode spectral resolution	0.0625 cm^{-1}
Tangent altitude range	5–150 km
Vertical resolution	~ 3 km
Field-of-view	3 km × 30 km
Orbit	sun-synchronous polar orbit
Orbit inclination	inclination of 98.40 degrees
Orbital period	about 100 minutes with a descending node mean local solar time (LST) of 10:00 am
Operational period	July 2002 toApril 2012

3. Retrieval method

3.1. Forward model and RFM

The atmosphere emits, absorbs, and scatters electromagnetic radiation, and the detailed spectrum depends on the gas molecules and temperature present. In the infrared spectral region, most of the molecular species have their own characteristic spectrum. Therefore, measurements of the infrared emission can be used to determine the atmospheric composition via radiative transfer.

The Reference Forward Model (RFM) is a line-by-line radiative transfer model, that originally developed by Oxford as FORTRAN program used to generate monochromatic limb emission radiances. It is a derivative of GENLN2 (*Edwards*, 1992), which is a general-purpose line-by-line atmospheric transmittance and radiance model. RFM is used as the forward model for Oxford MORSE retrieval algorithm.

As RFM is aline-by-line model, the transmission through the atmosphere is built up by subdividing the atmospheric path into a number of path segments. Each path segment can be considered to be homogeneous with respect to temperature, pressure, and gas concentration. Absorption coefficients are obtained by summing over a number of transitions for each molecule:

$$k(\upsilon) = \sum_i S_i(T) f\big((\upsilon - \upsilon_{0i}, p, T)\big), \quad (1)$$

where $S_i(T)$ is the line strength, f is the line-shape, and υ_0 is the central position of line i.

3.2. Inverse method and MORSE

The Levenberg-Marquardt method is applied to the Oxford MORSE retrieval algorithm. The Levenberg-Marquardt method can be used when the iterative process is unstable, because there is a significant degree of nonlinearity or when the iterative process begins far from the true solution. The method introduces a Levenberg-Marquardt parameter into the variation of the unknown, to stabilize the iteration. The solution is given by:

$$x_{i+1} = x_i + [(1+\gamma)S_a^{-1} + K_i^T S_y^{-1} K_i]^{-1}[K_i^T S_y^{-1}(y - F(x_i)) - S_a^{-1}(x_i - a)], \quad (2)$$

where *i* is the iteration number; γ is the tuneable parameter which can be adjust to achieve local minimum of cost so the retrieval may be generated towards the true solution.

In the optimal sequential estimation of the MORSE algorithm, the state vector retrieved from one measurement set is adopted as the *a priori* estimate during the inversion of the next set. Given that an equivalent solution can be derived without the simultaneous inversion of all measurements, the weighting function matrix is reduced, thereby enhancing memory efficiency. The solution is calculated sequentially at the profile level. Starting from the top of the atmosphere, the *a priori* estimate is updated by using values retrieved at previous tangent heights.

For MIPAS, the MORSE code takes a series of measurements from a single limb scan from the apodized Level 1b radiances, to retrieve vertical profiles of atmospheric parameters (e.g., temperature, VMRs, etc.). The *a priori* estimates required for the optimal estimation approach are taken from the climatology of *Remedios et al*. (2007). The internal forward model is based on the RFM model but using pre-tabulated monochromatic absorption coefficients rather than a full line-by-line calculation. The radiative transfer equation for MORSE additionally applies spectral and spatial convolutions to the radiance:

$$R(\upsilon_i, z_i) = \int\int L(\upsilon)\psi(\upsilon - \upsilon_i)\phi(z - z_i)dzd\upsilon\ , \quad (3)$$

where ψ is the (apodized) instrument line shape (AILS), ϕ is the field-of-view, ν is the spectral point, and *z* is the nominal tangent height.

Retrievals in this study were performed using v1.3 of the MORSE algorithm, ESA v5 L1B radiance data, together with the cloud index technique developed by *Spang et al.* (2004) to identify cloud-contaminated scans. The minor trace gases are retrieved with their corresponding microwindow lists, as shown in *Fig.2*. A microwindow is a small spectrum range containing molecular features used for retrieval.

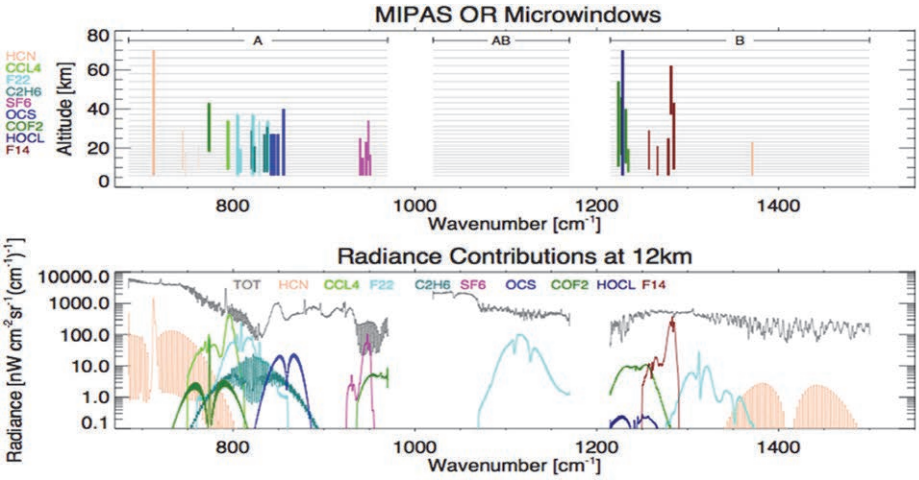

Fig. 2. The upper panel is the microwindows for different minor trace gases in this paper. The lower panel is their radiance contributions at 12km tangential height, with the grey spectrum representing the total background radiance. Adapted from (*Cai* and *Duhnia*, 2013).

4. Zonal mean databases comparison

4.1. MIPAS zonal mean

With the initial retrievals generated as stated in Section 3.2, one month of data (March 2010) of the minor trace gases are analyzed in this paper. A smoothing method is applied to the retrieval results in order to eliminate the anomaly data, which in this case is defined as cloud contamination, or a significant *a priori* contribution (the random error greater than 70% of the retrieved value). A 5σ global spike test is then applied to each species to all the remaining data in order to eliminate anomalous retrievals. The percentage of profiles removed by the spike test is shown in *Table 3*. The largest percentage is 22.3% from CF4. The removed profiles appear to be randomly located, independent of latitudes. Reasons for these spike test failures have yet to be investigated. As the total number of profiles for each species for one month is over 32,000, there still remain over 25,000 profiles, sufficient for statistical analyses.

Using the screened MIPAS data listed in *Table 3*, the monthly zonal means of the species are constructed, together with a standard deviation of profiles contributing to each grid point, which is a combination of random error and atmospheric variability. Here we only considered a monthly zonal mean for

March 2010, with 5° latitude grid and pressure range from 0.1 hPa to 1000 hPa with 6 points/decade. The modeled data from the SLIMCAT chemical transport model, which will be introduced in Section 4.3, are provided in the same grid conditions.

Table 3. March 2010 MIPAS retrieval basic information

Species	**Spike (%)**	**Max VMR (pptv)**	**Min VMR (pptv)**	**Pressure range (hPa)**	**spectral range (cm-1)**	**spectral range (cm-1)**
HCFC-22	0.79	260	9	0.1~560	803~839	-
CF_4	22.31	170	40	0.1~316	1256~1286	-
CCl_4	2.10	200	0.01	4~316	792~795	-
OCS	1.98	1000	0.01	1~400	840~857	2050~2053
C_2H_6	14.00	1000	0.0007	0.1~560	819~845	-
COF_2	3.79	430	0.09	0.1~560	772~775	1230~3750
HCN	5.68	440	110	0.1~560	711~762	1370~1372
SF_6	13.73	8	2	0.1~380	938~951	-
HOCl	0.00	280	0.01	0.1~560	1226~1229	-

Spike is representing the percentage of profiles that removed by the global 5σ spike test, max and min VMRs are the maximum and minimum values of the zonal mean after the spike test, andspectral ranges are those used in the Oxford MORSE retrieval.

MIPAS results for HCFC-22, CCl_4, C_2H_6, OCS, and SF_6 are shown in *Fisg. 3–7*. The greatest concentrations occur roughly over the equator. Lower stratospheric concentrations are significantly higher over the equator compared to higher latitudes. Zonal mean plots of species HCFC-22, CCl_4, C_2H_6, OCS, and SF_6, shown in *Figs.3–7*, all have this pattern. This pattern can be attributed to the Brewer-Dobson circulation (a slow upwelling of stratospheric air in the tropics, followed by a pole-ward drift through the mid-latitudes, and a descent in the mid-and-high latitudes).The general appearance is typical of long-lived gases such as CFCs that have tropospheric sources and are destroyed in the stratosphere. The standard deviation plots also show similar structure, which implies that MIPAS errors are approximately proportional to the retrieved values under the assumption that atmospheric variability is negligible. *Fig. 3* shows that the tropospheric concentration for HCFC-22 is roughly 200pptv (red color), which is consistent with the value shown in *Table 1*. *Fig. 4* shows that the concentration of CCl_4 in troposphere region is roughly 100pptv with a standard deviation of 10 pptv, i.e., 100±10pptv, which is consistent with the value (90pptv) of CCl_4 shown in *Table 1*. The zonal mean retrievals of C_2H_6have smaller VMR in the troposphere,

of about 200pptv (shown in *Fig. 5*), than the value of 400 shown in *Table 1*. The tropospheric VMR of SF_6 is about 6±0.8 pptv in *Fig.7*, which is close to the value shown in *Table 1*. The retrievals for these 5 minor species are reasonable, however, further validations are required.

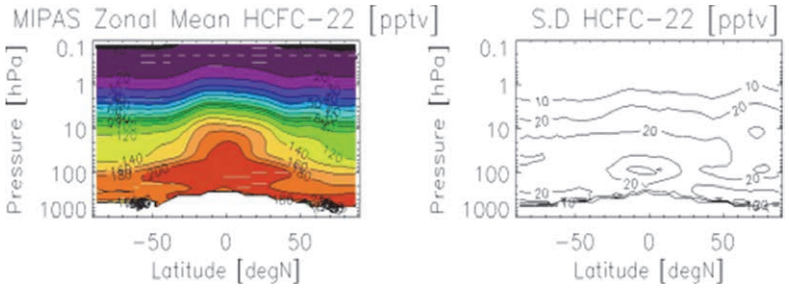

Fig. 3. MIPAS zonal mean and standard deviation of HCFC-22in March 2010.

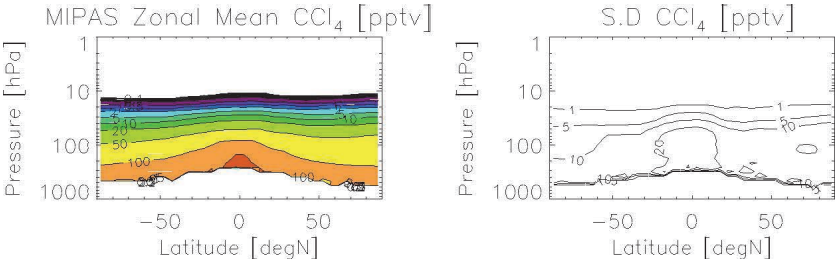

Fig. 4. MIPAS zonal mean and standard deviation of CCl_4in March 2010.

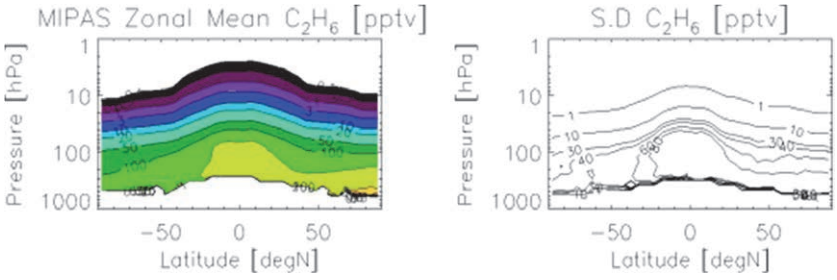

Fig. 5. MIPAS zonal mean and standard deviation of C_2H_6in March 2010.

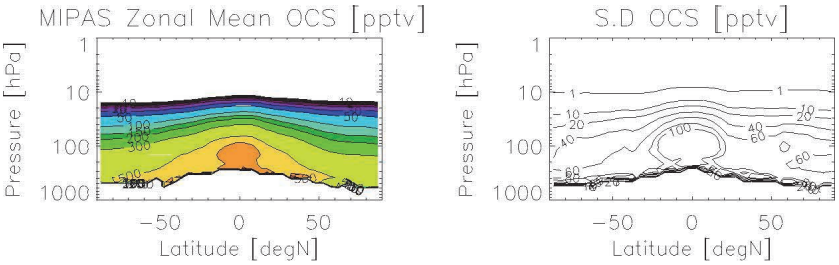

Fig. 6. MIPAS zonal mean and standard deviation of OCSin March 2010.

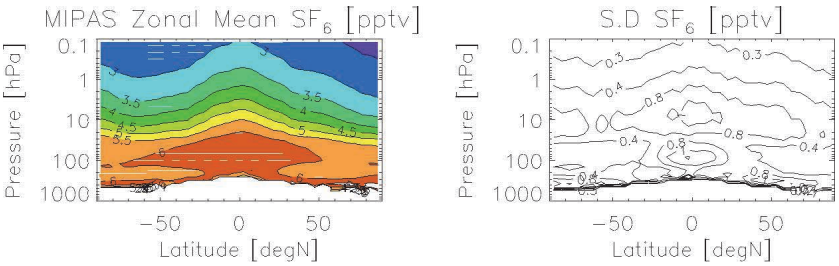

Fig. 7. MIPAS zonal mean and standard deviation of SF_6in March 2010.

The plot of COF_2 (*Fig.8*) shows a maximum of VMR around the middle of the stratosphere over the equator. This occurs, because COF_2 is an intermediate product in the degradation of CFCs in the stratosphere, which results in an increase in concentration. Also, because COF_2 is destroyed by photolysis and reaction with O(1D) in the upper stratosphere, the concentration decreases at higher altitudes. There is a second maximum of VMR in the stratosphere over the southern hemisphere (SH) polar region. As the data we obtained for this zonal mean plot is March 2010, which is the end of summer in SH. Then photochemical production of COF_2 extends to the pole in the middle stratosphere (i.e., in polar day).

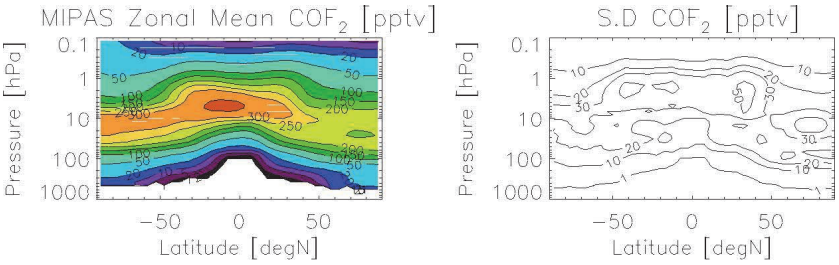

Fig. 8. MIPAS zonal mean and standard deviation of species COF_2in March 2010.

The VMR of HOCl shown in *Fig. 9* shows almost symmetric structure with high VMRs over mid-latitude regions at about 5hPa. HOCl is a product of ClO and HO, but destroyed by photolysis. As March is springtime, both north and southpoles have the same amount of sunlight which may be the reason of the symmetry between the north and south hemispheres. In March, when most of the sunlight is over the equator region, where there is more HOCl, thephotolysis results in relatively small VMR. However, the South Pole region has higher VMRs at about 30hPa than the north. The reason requires further investigation.

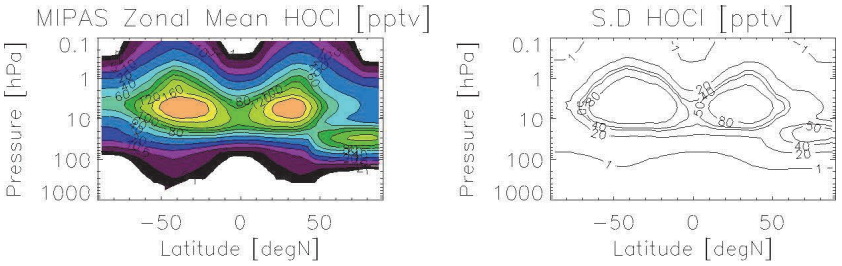

Fig. 9. MIPAS zonal mean and standard deviation of HOClin March 2010.

4.2. The SLIMCAT model

SLIMCAT is a 3D off-linechemical transport model (CTM) using winds and temperatures from meteorological analyses (e.g., from the UK Met Office or ECMWF) to specify the atmospheric transport and temperatures, and calculates the abundances of chemical species in the troposphere and stratosphere (*Chipperfield*, 2006). The model also uses a specified surface VMR of the source gases as boundary condition. These surface VMRs are time-dependent monthly values and based on surface measurements. The data used here for comparisons are provided by Sandip Dhomse and Martyn Chipperfield from output of a standard SLIMCAT stratospheric chemistry run for March 2010.

4.3. Zonal mean comparisons

SLIMCAT also models the species HCFC-22, CCl4, COF2, HOCl, and HCN. However, the HCN tropospheric concentration is not yet sorted out for SLIMCAT model, leaving four species. These are shown in *Figs. 10–13*.

For species HCFC-22, SLIMCAT and MIPAS agree well with each other. The maximum difference is 30 pptv, about 15%, around 20 hPa and 100 hPa in the southern hemisphere.

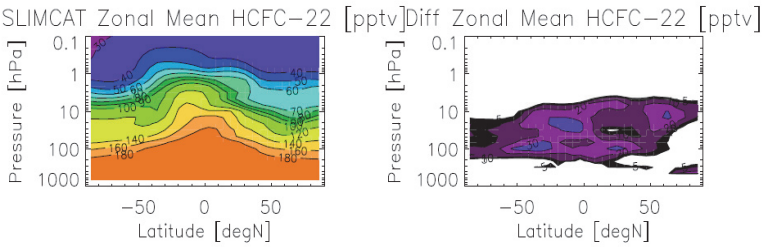

Fig. 10. SLIMCAT zonal mean of HCFC-22, and the (MIPAS – SLIMCAT) differencein March 2010.

Differences in CCl_4 between MIPAS and SLIMCAT are very small over the equator in the stratosphere, but about 50 pptv, about 33%, in the lower troposphere, with MIPAS larger. Also, MIPAS is also larger in high latitude regions in the troposphere and has more details of variation of the VMRs. Since the SLIMCAT is the modeled with stratospheric chemistry scheme, better results will be obtained for stratosphere than for troposphere. The variation of CCl_4 VMRs in the troposphere is not well modeled.

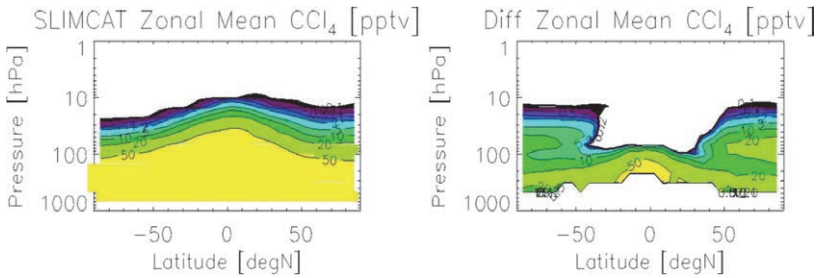

Fig. 11. SLIMCAT zonal mean of CCl4, and the (MIPAS – SLIMCAT) differencein March 2010.

SLIMCAT and MIPAS values of HOCl have larger differences than the other three species in the March 2010 zonal mean plots. Zonal means from SLIMCAT and MIPAS only consistent with each other at large VMR in the upper stratosphere region and around 50 hPa in northern high latitude region.

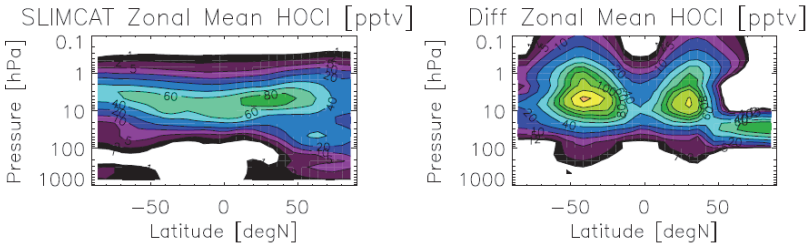

Fig. 12. SLIMCAT zonal mean of HOCl, and the (MIPAS – SLIMCAT) differencein March 2010.

The differences in COF_2 between MIPAS and SLIMCAT are very small over the equator in the stratosphere, but about 0~5 pptv, about 5%, in the lower troposphere, with MIPAS larger. Larger differences occur mainly in the stratospheric region with the percentage of about 40%.

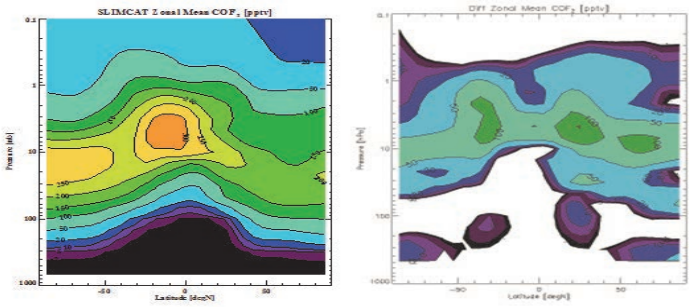

Fig. 13. SLIMCAT zonal mean of COF_2, and the (MIPAS – SLIMCAT) differencein March 2010.

5. Some preliminary results

5.1. Fluorine and chlorine budgets

As MIPAS can measure many of the halogenated compounds in the stratosphere, it is useful to study the fluorine and chlorine budgets with MIPAS data. The fluorine species measured by MIPAS are COF_2, CFC-11 (CCl_3F), CFC-12 (CCl_2F_2), CF_4, HCFC-22 ($CHClF_2$), and SF_6 from which the total fluorine measured by MIPAS can be computed as:

$$[F]_m = 2[COF_2] + [CCl_3F] + 2[CCl_2F_2] + 4[CF4] + 2[CHClF_2] + 6[SF_6], \quad (4)$$

where '[ ]'represents the volume mixing ratio (VMR) of each species.

Mahieu et al. (2008) show that most of the stratospheric fluorine species eventually form hydrogen fluoride [HF], which is not measured by MIPAS. Other fluorine containing species are negligible compared with these. Hence the total fluorine considered here is represented as following:

$$[F] = [F]_m + [HF]. \quad (5)$$

Fig.14 shows the vertical profiles with global average of all the fluorine species and total fluorine measured by MIPAS. In the lower stratosphere and upper troposphere, the atmospheric fluorine is mainly contributed by CFC-12. COF_2 contributes nearly half of the fluorine at the 10 hPa pressure level, while CF_4 dominates in the upper stratosphere.

The total $[F]_m$ decreases with altitude as fluorine ends up as HF. The expected HF zonal plot for March 2010 is constructed by the following:

$$[HF]_m = [F_m]_{max} - [F]_m, \quad (6)$$

where $[F_m]_{max}$ is the maximum value of $[F]_m$.

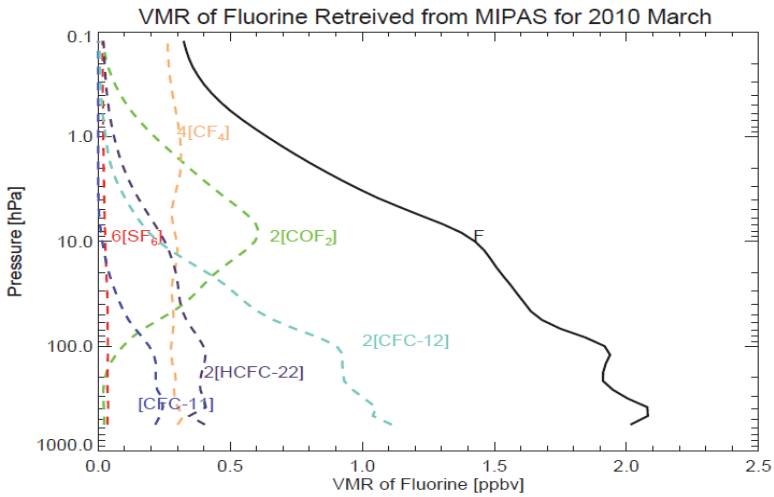

Fig. 14. Global fluorine contained in species measured by MIPAS (*Cai et al.*, 2013).

Constructing the monthly zonal mean for expected HF from MIPAS, $[HF]_m$, is compared with the zonal mean from SLIMCAT, $[HF]_a$ in *Fig.15*. The plots are consistent with each other. Adding the vertical profile of HF modeled by SLIMCAT (see *Fig.14*) should result in constant total [F].

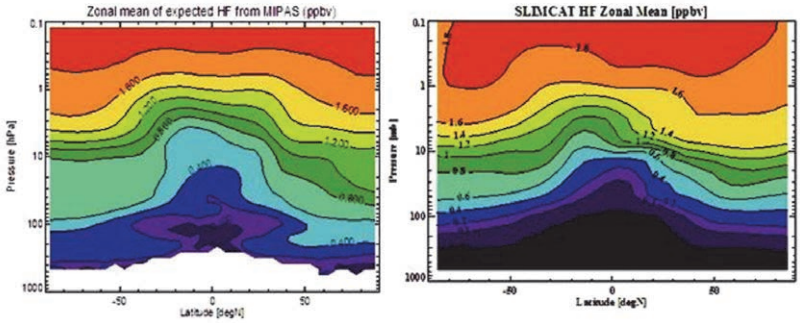

Fig. 15. Zonal mean of HF deduced from MIPAS and modelled by SLIMCATin March 2010.

Similarly, for chlorine budget, the species measured by MIPAS are CFC-11, CFC-12, CFC-22, CCl_4, HOCl, and $ClONO_2$, from which the total chlorine measured by MIPAS can be computed as:

$$[Cl]_m = 3[CCl_3F] + 2[CCl_2F_2] + [CHClF_2] + 4[CCl_4] + [ClONO_2] + [HOCl]. \quad (7)$$

There are three major chlorine species, HCl, CH_3Cl, and CFC-113 that are not measured by MIPAS. However, CH_3Cl has spectral feature at about 700 cm^{-1} and CFC-113 has features at 780–995 and 1005–1232 cm^{-1} spectral ranges, and so they are the potential retrieval candidates of MIPAS. *Fig. 16* shows the global averaged vertical profiles of all the chlorine species and total chlorine $[Cl]_m$ measured by MIPAS. The solid line, representing the amount of $[Cl]_m$, is decreasing with altitude, starting with about 2.4 ppbv in the troposphere. In the troposphere, around half of the total chlorine is contributed by CFC-12 and around one third of it is contributed by CFC-11. $ClONO_2$ dominates the chlorine VMR at around the 20 hPa pressure level without considering the concentrations of HCl, CH_3Cl, and CFC-113.

The approach of constructing expected [HF] can be applied for expected [HCl]+[CFC-113]+[CH_3Cl]. Data provided by ACE-FTS will be included for comparison in the future.

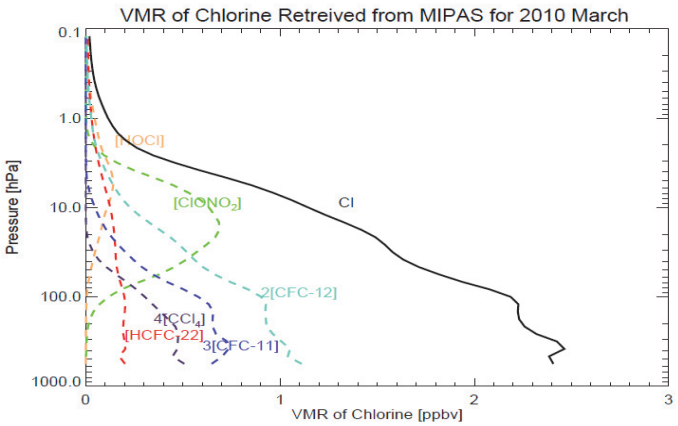

Fig. 16. Global chlorine contained in species measured by MIPAS.

6. COF_2 MIPAS retrieval method study and improvement

6.1. Modifications of the retrieval method

The problem of retrieving minor traces gases with Oxford MORSE algorithm and current parameters set for MORSE code is that these gases have relatively small signal-to-noise ratio in the emission spectrum compared with atmospheric major gases, such as O_3 and CH_4, which are retrieved by Oxford MORSE. The minor trace gas retrieval problem can be shown mathematically as follows:

From Section 3.2, the retrieval covariance general solution for optimal estimation is $S_x = (\mathrm{K}^T S_y^{-1} K + S_a^{-1})^{-1}$. Let

$$S_n^{-1} = K^T S_y^{-1} K, \tag{8}$$

where $\boldsymbol{S}_y$is the instrument noise in the level1 spectrum, $\boldsymbol{S}_n$ is the measurement error transferred into VMR space by the Jacobian, i.e., $\boldsymbol{S}_n$ is the covariance of the measurements.

Eq.(8) can be simplified as:

$$S_x = (S_n^{-1} + S_a^{-1})^{-1}. \tag{9}$$

For major atmospheric gases, who have strong emission signals, retrieval errors, S_x, is dominate by the measurement noise, S_n, covariance of *a priori* is negligible. Hence the retrieval is mainly contributed by the measurements.

However, for minor trace gases, for example, COF_2, whose emission signal is small,the measurement errors are at the same magnitude scale as the *a priori* errors. From Eq.(9) we can see that in order to obtain better retrievals, one can either reduce the measurement noise or increase the*a priori* covariance, in other word, reduce S_n or increase S_a.

Reducing measurement noise can be achieved by retrieved with more measurements, for example, retrieved COF_2 with monthly spectrum instead of individual profiles. Increasing the*a priori* covariance simply means relaxing the*a priori* constrains in our study. In this paper, we focus on the second method.

Two ways can be considered to change the *a priori* covariance matrix in the MORSE code: one is by changing the correlation length and the other is by changing the *a priori* uncertainty for each gas. The correlation length can be considered a parameter representing the vertical smoothing of retrievals. *Table 4* shows three different parameter settings for studying the effect of relaxing the*a priori* constraints for COF_2 retrievals. The default setting (cur) has a strong correlation length of 50 km, which provides regularization at the expense of vertical resolution. The vertical resolution of COF_2 retrievals can be improved by reducing the correlation length to 5 km (cor5km). Initially, the *a priori* uncertainty is set to 100% to avoid overconstraining the retrieval for major species. An *a priori* uncertainty of 1000% (apun) is selected to test the effect of increasing *a priori* assumed errors. These three settings of COF_2 retrievals are all generated with the same spectral microwindows, which are associated with different altitude ranges and are shown in *Table 5*.

Table 4. Three different parameter settings for COF_2retrievals

Name	**Correlation length**	***A priori* uncertainty**
cur (default)	50km	100%
cor5km	5km	100%
apun	50km	1000%

Table 5. The microwindow set and associated altitude ranges for COF_2

Microwindow	**Spectral range (cm^{-1})**	**Altitude (km)**
COF20301	1230.3750 ~ 1233.3750	12.0 ~ 40.0
COF20302	1233.6875 ~ 1235.8125	7.5 ~ 19.5
COF20303	772.0000 ~ 775.0000	18.0 ~ 43.0
COF20304	1225.7500 ~ 1228.6875	16.5 ~ 46.0
COF20305	1222.4375 ~ 1225.4375	10.5 ~ 54.0

6.2. Evaluation parameters

6.2.1. Averaging kernels

Averaging kernels describe how the true state ($\underline{\mathbf{x}}$) of the atmosphere has been distorted by the retrieval (**x**):

$$\underline{\mathbf{x}} = \mathbf{A}\mathbf{x}, \quad (10)$$

which is defined as the rows of matrix **A:**

$$\mathbf{AK} = \mathbf{I} - \mathbf{S_x}\mathbf{S_a}^{-1}. \quad (11)$$

The rows of **A** are the averaging kernels (smoothing functions) that map the true state into the retrieval space. The width of the kernel is a measure of the retrieval resolution. The area of the averaging kernel is roughly unity where the retrieval is accurate and can be thought of as a rough measure of the fraction of the retrieval, that comes from the measurement rather than the *a priori* estimate (*Rodgers*, 2000).

6.2.2. Degrees of freedom (DOF)

The number of degrees of freedom (DOF) is a scalar measure of the number of independent quantities that can be measured. The largest number of degrees of freedom possible is clearly determined by the number of elements in the measurement vector (or, indeed, the state vector – whichever is the smaller), and it is defined as the trace of **AK**:

$$DOF = tr(AK) \quad (12)$$

6.2.3. Shannon information content

The Shannon information content is a scalar quantity originally conceived to describe the information carrying capacity of communications channels (*Shannon* and *Weaver*, 1962). It is also a useful quantity for the optimization of observing systems. The information content of a measurement can be defined qualitatively as the factor by which knowledge of a quantity is improved by making the measurement (*Rodgers*, 2000). It is defined as:

$$IC = -\frac{1}{2} ln|I_n - AK| \ . \quad (13)$$

6.3. Results

Data for the three aforementioned retrieval settings for 1 day are generated. *Figs. 17–19* show the zonal mean of COF_2 for 1 day. These three figures all capture the maximum concentration at the mid-stratosphere over the equatorial region of COF_2 in March. A decrease in the correlation length with increasing COF_2 concentration is shown over the North Pole at around the 30 km altitude (*Fig. 18*). The same finding is also captured by increasing the*a priori* uncertainty, as shown in *Fig. 19. Fig. 19* shows more fluctuations of retrievals at higher altitudes, especially over the equatorial region. The concentration of COF_2 in *Fig. 18* is roughly smaller than that in *Fig. 17* at the same altitude. Overall, the concentrations are consistent with one another.

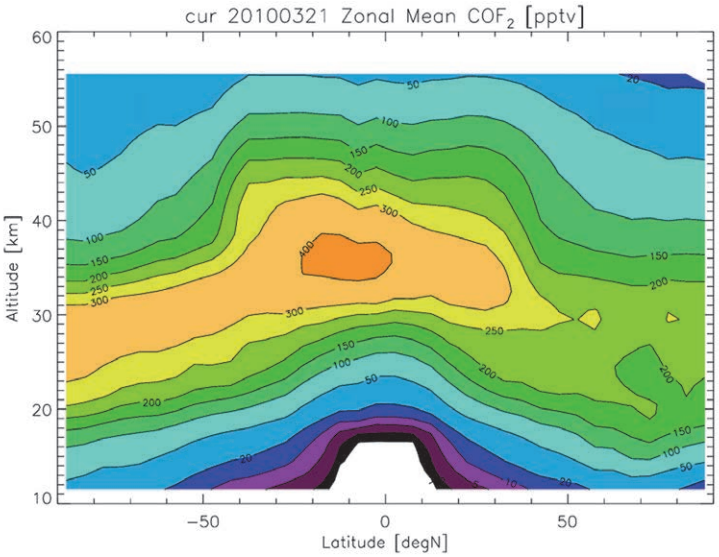

Fig. 17. Zonal mean of COF_2 with 1 day of data under "cur(default)" setting.

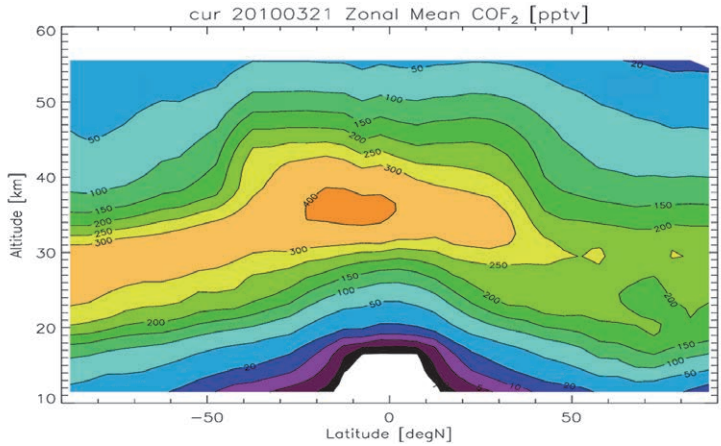

Fig. 18. Zonal mean of COF_2 with 1 day of data under "cor5km" setting, which changes the correlation length to 5 km.

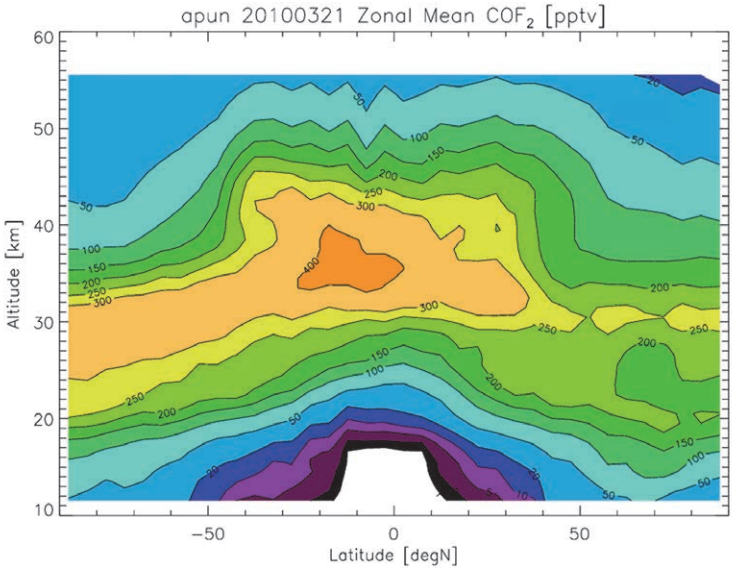

Fig. 19. Zonal mean of COF_2 with 1 day of data under "apun" setting, which changes the *a priori* uncertainty to 1000%.

The averaging kernels are derived within the 30–60N latitude band for these three sets of retrievals. The averaging kernels are the rows of matrix **A** as mentioned in Section 6.2.1. *Figs. 20–22* show the averaging kernel and vertical resolution of three different setting retrievals of COF_2. The resolution at each altitude is defined as the ratio of the grid spacing to the diagonal of the averaging kernel matrix, which is only meaningful where averaging kernels have distinct peaks at the tangent points.

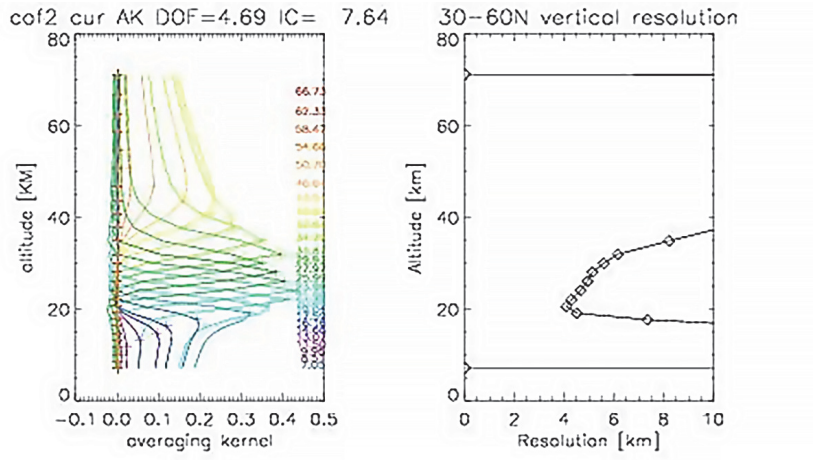

Fig. 20. Left panel: Averaging kernels for retrievals with default setting over the 30–60N region on March 21, 2010. The measurement altitude of each averaging kernel is indicated by a cross with matching color, with the values of DOF= 4.69, IC=7.64. Right panel: Vertical resolution as a function of altitude of this averaging kernel. Resolutions are lower than the MIPAS field of view of ~3 km.

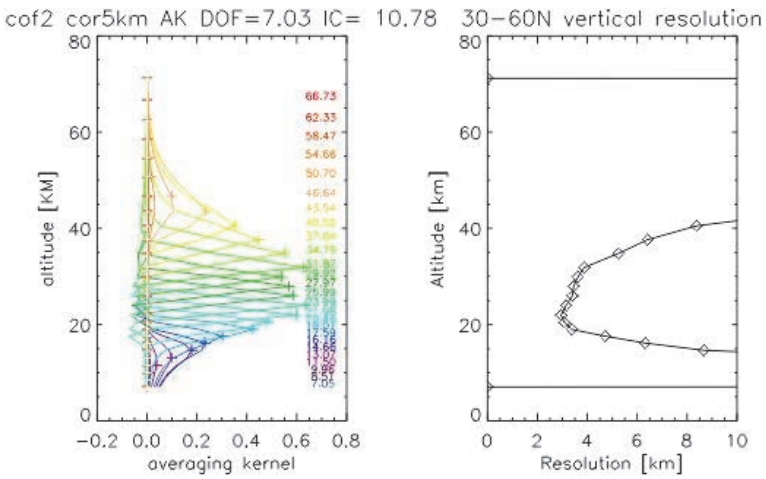

Fig. 21. Averaging kernels and vertical resolution for COF_2 retrieval after changing the *a priori* correlation length to 5 km. DOF=7.03, IC=10.78.

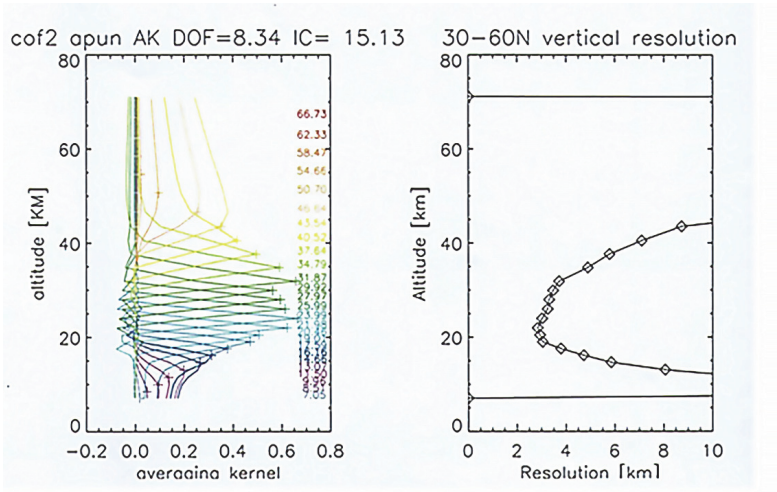

Fig. 22. Averaging kernels and vertical resolution for COF_2 retrieval after changing *a priori* uncertainty to 1000%. DOF=8.34, IC=15.13.

A direct comparison of the vertical resolution of the three retrievals is shown in *Fig.23*. The best vertical resolution is achieved at around the 20-30 km altitude for all three retrievals, which is as expected as the concentration of COF_2 is largest at these altitudes over the north mid-latitude region. Vertical resolutions for "cor5km" and "apun" retrievals are clearly better than that for "cur" retrieval. At around 20 km altitude, the vertical resolution is about 4 km, thereby indicating "cur" (default) retrieval. Meanwhile, vertical resolutions for the other two retrievals are about 3 km, which is the best resolution that can be achieved, matching of MIPAS field of view height. From the perspective of resolution, reducing the correlation length to 5 km or increasing the*a priori* uncertainty to 1000% can achieve better retrieval results for COF_2.

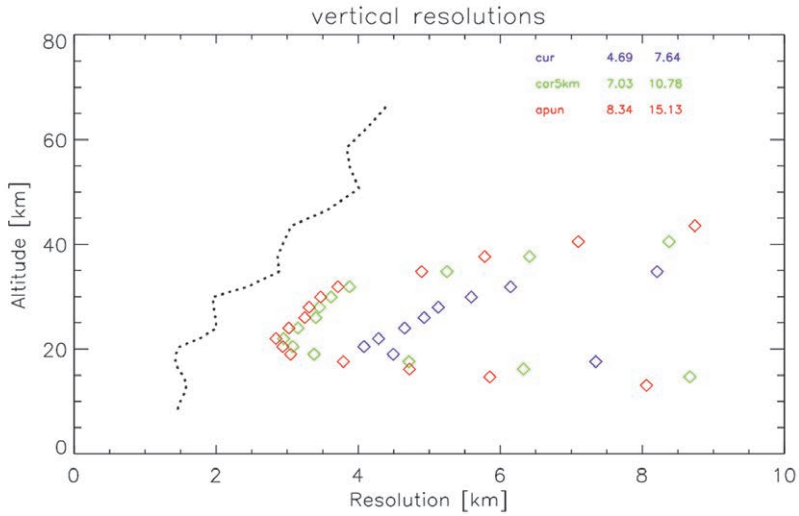

Fig. 23. Vertical resolutions of the three different retrievals. The black dotted line shows the vertical spacing of the retrieval grid (which is also the measurement tangent height spacing) for the mid-latitude profile.

Table 6 lists the degrees of freedom (DOF) and information content (IC) for three different retrievals, which are derived from the corresponding AK. As it was expected, relaxing the*a priori* constraints ("cor5km" and "apun") results in a higher DOF and inmore information from measurements. In other words, the DOFs for "cor5km" and "apun" are higher than that for the default setting of retrievals. Similarly, the same trend is observed for IC.

Table 6. DOF and IC for the three different COF_2 retrievals

settings	**DOF**	**IC**
cur(default)	4.69	7.64
cor5km	7.03	10.78
apun	8.34	15.13

6.4. Chi-square test

The diagnostics only depend on the retrieval and *apriori* covariance, havinglittle information about the consistency of the individual retrieved profiles. In theory, with relaxing the*apriori* constrains, the noise will increase linearly. But in reality, the noise always increases nonlinearly, and the chi-square is a quantity to measure the uncertainty of individual retrieved profiles in order to make sure that the noise is not amplified too much.

The chi-square test is introduced to analyze the consistency of the individual profiles and is defined as follows:

$$\chi^2 = \frac{1}{N}\sum_{i=0}^{n} \delta p_i^T \cdot S_\delta^{-1} \cdot \delta p_i \ , \tag{14}$$

where δp_i is the difference between the retrieval profile *i* and the reference profile;S_δ is the measurement noise of the difference between the retrieval profile and the reference profile; there are *N* profiles in total.

There are different applications of the chi-square test by choosing different reference profiles. In this study, we consider the following applications.

Application 1: Reference profile = interpolation profile, with assumption that linear interpolation is valid for the three adjacent retrieval profiles. Then δp_i and S_δ^{-1} are defined as follows:

$$p_{in} = \frac{(p_{i-1}+p_{i+1})}{2} \ , \tag{15}$$

$$\delta p_i = (p_i - p_{in}) \ , \tag{16}$$

$$\delta S_i = (S_i + S_{in}) = \frac{3}{2} S_i \ , \tag{17}$$

where S_{in} is the covariance of interpolation profile, which is derived as $S_{in} = \frac{1}{4}(S_{i+1} + S_{i-1}) \approx \frac{1}{2} S_i$, where S_i is the measurement covariance of profile *i*, the inverse of S_i is the differences of the inverse retrieval covariance and the inverse

of the*a priori* covariance. In mathematical term, $S_i^{-1} = S_{xi}^{-1} - S_{ai}^{-1}$, where S_{xi} and S_{ai} represent the covariance of retrieval and the *a priori* for profile *i*.

Hence, chi-square value in Eq.(14) for this application is derived as follows:

$$\begin{aligned}\chi^2 &= \frac{1}{N}\sum_{i=0}^{n} \delta p_i^T \cdot \frac{2}{3}(S_{xi}^{-1} - S_{ai}^{-1}) \cdot \delta p_i = \\ &= \frac{1}{N}\sum_{i=0}^{n} (p_i - p_{in})^T \cdot \frac{2}{3}(S_{xi}^{-1} - S_{ai}^{-1}) \cdot (p_i - p_{in}) = \\ &= \frac{1}{N}\sum_{i=0}^{n} [p_i - \frac{(p_{i-1}+p_{i+1})}{2}]^T \cdot \frac{2}{3}(S_{xi}^{-1} - S_{ai}^{-1}) \cdot [p_i - \frac{(p_{i-1}+p_{i+1})}{2}] .\end{aligned} \quad (18)$$

6.5. Chi-square test results

The chi-square value for application 1 in this report is constructed using 1day (March 21, 2010) of retrieval data for COF_2. As previously conducted, cloud accumulation profiles are eliminated. *Fig. 24* shows the distribution of chi-square values for the three different retrieval settings. Most chi-square values are relatively small, except for some anomalies (large chi-square value). Distributions of the chi-square value fall roughly exponentially as the chi-square value increases for all three retrievals. *Table 7* summarizes the mean and median values for the chi-square values in *Fig. 24*. The median value is a more sensible quantity to describe the chi-square value because of the anomalies in the chi-square values. The median of the chi-square value is larger for relaxingthe *a priori* constraint retrievals. The mean of "apun" is almost three times larger than the mean of default retrievals, whereas the mean of "cor5km" is almost twice as much as that of „cur(default)".

*Table 7.*The mean and the median values of chi-square values

settings	**Mean**	**Median**
cur(default)	12.65	7.45
cor5km	22.00	12.96
apun	38.13	20.24

To better understand the distributions, locations of anomalies need to be identified. As shown in *Fig*s. *25(a)* and *25(b)*, the distribution of chi-square values for default setting retrievals only has two chi-square values that are larger than the threshold. This result implies two anomaly profiles of the retrieval. From *Fig. 25(b)*, these two anomaly profiles are in the south polar region. *Fig*s. *25(c)*

and *25(d)* show the distribution of chi-square values and location of anomaly profiles for the 5 km correlation length. Anomaly profiles mainly lie within the 80–90S latitude band. One profile exists in the north polar region. *Figs. 25(e)* and *25(f)* illustrate the distribution of chi-square values and locations of anomaly profiles for the 1000% *a priori* uncertainty retrieval. The chi-square values are more varied than the previous two retrievals and contain more anomalies. Anomaly profiles occur mainly at around the 60N latitude in the northern hemisphere, which may correspond to the oscillations at the same latitude range in the zonal mean plot (*Fig. 19*). In the southern hemisphere, half of the anomalies lie over the South Pole. Data are retrieved in March, which is summer in the southern hemisphere. Temperature is more varied in the south polar region, which would have influence as COF_2 is mainly from the temperature-dependent reaction of HCFC-22+OH. One possible reason for the anomalies is temperature uncertainty, which needs to be confirmed through further investigations.

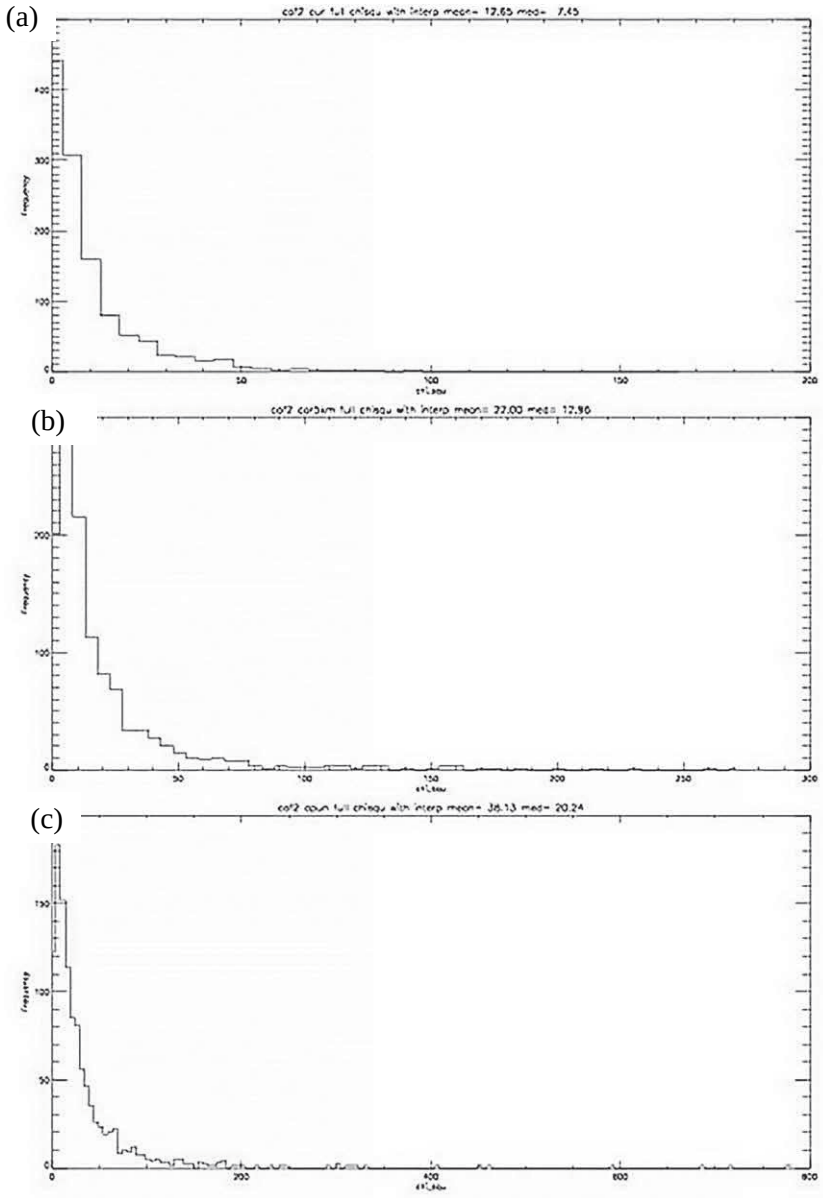

Fig. 24. The distribution of chi-square values for (a) cur(default) setting, (b) cor5kmsetting, and (c) apun setting of retrievals on date March 21, 2010. The y axis is the frequency and the x axis is the chi-square value.

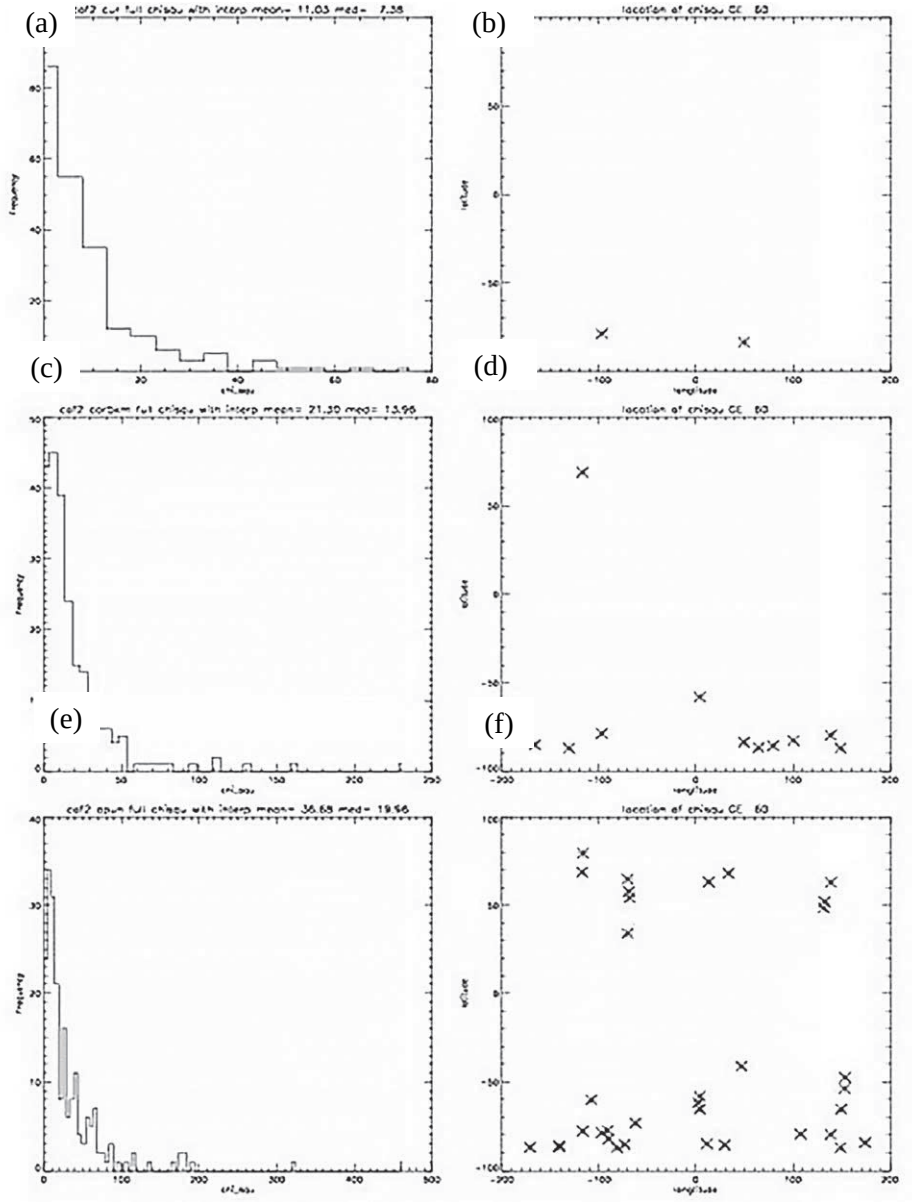

Fig. 25.(a), (c), and (e) are distributions of chi-square values with the band of 5 for the three different setting retrievals. The y axis is the frequency (i.e., number of counts) and the x axis is the chi-square value. (b), (d), and (f) are the locations of profiles that have chi-square value larger than the threshold of 60. The y axis is the latitude and the x axis is the longitude.

7. Conclusions and future work

In this paper, we discussed retrievals of minor trace species of HCFC-22, HOCl, OCS, C_2H_6, COF_2, HCN, CF_4, SF_6, and CCl_4. Preliminary zonal mean results of these retrievals are satisfactory except for HCN and CF_4 species, which have some anomalies requiring further investigation. Comparison with SLIMCAT results are also discussed. CCl_4, COF_2, HCFC-22, and HOCl zonal mean plots of MIPAS and SLIMCAT seem consistent. We then used MIPAS to estimate the total F and Cl budgets in the atmosphere, and also compared the result with SLIMCAT.

The expected zonal mean HF produced from MIPAS fluorine budgets agrees with the SLIMCAT results. The vertical profiles of both fluorine and chlorine budgets need to be compared with other satellite results, like ACE-FTS and other MIPAS processors.

Finally, we focus on improving the retrieval method for minor trace species, COF_2, by adjusting correlation length and *a priori* constraint, as well as chi-square introduced to analyze noise. Results shown that we did make improvement and could get more information from the measurements.

Comparison with ACE-FTS, other MIPAS processor, and model results are required for further validation.

Acknowledgments: I would like to take this chance to express my gratitude to those who assisted me in many ways during the writing of this study. My deepest thank goes to Professor Anu Dudhia from Department of AOP Physics, University of Oxford, for his explicit advice on sharpening my ideas and improving the accuracy of this paper. I shall extend my thanks to relevant MIPAS and SLIMCAT team members for their ground-breaking work. Also, I'm obliged to my family and colleges who accompanied me these years, giving me the support that I will never forget.
Finally, my sincere gratitude goes to those who have devoted time reading this paper and given me many suggestions, which will benefit my study and work in the future.

References

Altshuller, A.P., 1976: Average tropospheric concentration of carbon tetrachloride based on industrial production, usage, and emissions. *Environ. Sci.Technol.10,* 596–598. https://doi.org/10.1021/es60117a007

Cai, S. and *Dudhia, A.,* 2013: Analysis of new species retrieved from mipas. *Ann.Geophys. 56,* 969–975.https://doi.org/10.4401/ag-6340

Chipperfield, M.P. 2006: New version of the TOMCAT/SLIMCAT off-line chemical transport model: Intercomparison of stratospheric tracer experiments. *Q. J. the Roy.Meteorol. Soc.132,* 1179–1203.https://doi.org/10.1256/qj.05.51

Cicerone R.J. and *Zellner, R.,* 1983: The atmospheric chemistry of hydrogen cyanide (HCN). *J. Geophys. Res.: Oceans 88,* 10689–10696.https://doi.org/10.1029/JC088iC15p10689

Von Clarmann, T., Glatthor, N., Ruhnke, R., Stiller, G. P., Kirner, O., Reddmann, T., and*Funke, B.,* 2009: HOCl chemistry in the antarctic stratospheric vortex 2002, as observed with the michelson interferometer for passive atmospheric sounding (MIPAS). *Atmos. Chemist. Phys.9,* 1817–1829.https://doi.org/10.5194/acp-9-1817-2009

*Domanski, P.A.,*1999: Evolution of refrigerant application. In Proceedings of the Inter-national Congress on Refrigeration.

Edwards, D.P., 1992. GENLN2: A general line-by-line atmospheric transmittance and radiance model. National Center for Atmospheric Research.

Fischer, H., Brik, M., Blom, C., Carli, B., Carlotti, M., Von Clarmann, T., and *Zander, R.*2008: MIPAS: an instrument for atmospheric and climate re-search. *Atmos. Chemist. Phys.8*, 2151–2188. https://doi.org/10.5194/acp-8-2151-2008

Forster, P., Ramaswamy, V., Artaxo, P., Berntsen, T., Betts, R., Fahey, D., and *Averyt, K.*,2007: Changes in atmospheric constituents and in radiative forcing. IPCC Fourth Assessment Report: Climate change 2007.

Glatthor N., Von Clarmann, T., Stiller, G.P., Funke, B., Koukouli, M. E., FischerH., Grabowski, U., Höpfner, M., Kellmann, S., and *Linden, A.* 2009: Large-scale upper tropospheric pollution observed by MIPASHCN and C_2H_6 global distributions. *Atmos. Chem. Phys.9*, 9619–9634. https://doi.org/10.5194/acp-9-9619-2009

*Harnisch J.*and *Eisenhauer, A.*,1998: Natural CF_4 and SF_6 on earth. *Geophys.Res. Lett.25*, 2401–2404. https://doi.org/10.1029/98GL01779

Helas, G. and *Wilson, S.R.*,1992: On sources and sinks of phosgene in the troposphere. *Atmos.Environ. Part A. General Topics 26*, 2975–2982.https://doi.org/10.1016/0960-1686(92)90289-W

Hickson, K.M., Keyser, L.F., and *Sander, S.P.*,2007: Temperature dependence of the HO_2+ClO reaction. 2. reaction kinetics using the discharge-flow resonance-fluorescence technique. *J. Phys. Chem. A, 111*, 8126–8138.https://doi.org/10.1021/jp0689464

Kaye, J.A., Douglass, A.R., Jackman, C.H., Stolarski, R.S., Zander, R., Roland, G., 1991: Two-dimensional model calculation of fluorine-containing reservoir species in the stratosphere. *J. Geophys. Res.: Atmospheres 96*, 12865–12881.https://doi.org/10.1029/91JD01178

Mahieu, E., Duchatelet, P., Demoulin, P., Walker, K.A., Dupuy, E., Froidevaux, L., Randall, C., Catoire, V., Strong, K., Boone, C.D.,Bernath, P.F., Blavier, J.F., Blumenstock, T., Coffey, M., De Mazière, M., Griffith, D., Hannigan, J., Hase, F., Jones, N., Jucks, K.W., Kagawa, A., Kasai, Y., Mebarki, Y., Mikuteit, S., Nassar, R., Notholt, J., Rinsland, C.P., Robert, C., Schrems, O., Senten, C. Smale, D., Taylor, J., Tétard, C., Toon, G. C., Warneke, T., Wood,S.W., Zander, R,.and *Servais, C.*,2008: Validation of ACE-FTS v2.2 measurements of HCl, HF, CCl_3F and CCl_2F_2 using space-, balloon- and ground-based instrument observations. *Atmos. Chem. Phys.8*, 6199–6221.https://doi.org/10.5194/acp-8-6199-2008

Mahieu, E., Rinsland, C. P., Zander, R., Duchatelet, P., Servais, C., and *Mazière, M.De.*, 2003: Tropospheric and stratospheric carbonyl sulfide (OCS): long-term trends and seasonal cycles above the jungfraujoch station.EUR 20650.

Mccann, P., Chao, I-Na., Namjou, K., 2000: Measurement of NO, COF_2, and H_2O with a single mid-infrared laser. In Laser Applications to Chemicaland Environmental Analysis, Optical Society of America.https://doi.org/10.1364/LACEA.2000.SaB6

Midgley, P.M. and *Fisher, D.A.*, 1993: The production and release to the atmosphere of chlorodiuoromethane (HCFC-22). *Atmos. Environ. Part A. General Topics27*, 2215–2223. https://doi.org/10.1016/0960-1686(93)90051-Y

Mishalanie, E.A., Rutkowski, C.J., Hutte, R.S., and *Birks, J.W.*, 1986: Ultraviolet absorption spectrum of gaseous HOCl. *J. Phys. Chem.90*, 5578–5584.https://doi.org/10.1021/j100280a021

*Molina, M.J.*and *Rowland, F.S.*, 1974: Stratospheric sink for chlorofluoromethanes: chlorine atom-catalysed destruction of ozone. *Nature249*, 810–812.https://doi.org/10.1038/249810a0

Muhle, J., Ganesan, A.L., Miller, B.R., Salameh, P.K., Harth, C.M., Greally, B.R., Rigby, M., Porter, L.W., Steele, L.P., Trudinger, C.M., Krummel, P.B., O'Doherty, S., Fraser, P.J., Simmonds, P.G., Prinn, R.G., and *Weiss, R.F.*,2010: Perfluorocarbons in the global atmosphere: Tetrafluoromethane, hexafluoroethane, and octafluoropropane. *Atmos. Chem. Phys.10*, 5145–5164.https://doi.org/10.5194/acp-10-5145-2010

Notholt, J.,Kuang, Z., Rinsland, C.P., Toon, G.C., Rex, M., Jones, N., Albrecht, T., Deckelmann, H., Krieg, J., Weinzierl, C., Bingemer, H., Weller, R.,and *Schrems,O.*,2003: Enhanced upper tropical tropospheric COS: Impact on the stratospheric aerosol layer.*Science 300*, 307–310. https://doi.org/10.1126/science.1080320

Reimann, S., Ko, M., Newman, P., and *Strahan, S.*, 2013: Re-evaluation of the lifetimes of ozone-depleting substances and related trace gases. In *EGU Gener. Ass.Conf. Abst.15*, 1106.

Remedios, J.J., Leigh, R.J., Waterfall, A.M., Moore, D.P., Sembhi, H., Parkes, I., Greenhough, J., Chipperfield, M.P., and *Hauglustaine. D.*,2007: Mipas reference atmospheres and comparisons to v4.61/v4.62 MIPAS level 2 geophysical data sets. *Atmos. Chem. Phys. Discuss.7*, 9973–10017.https://doi.org/10.5194/acpd-7-9973-2007

Rinsland, C.P., Gunson, M.R., Wang, P.H., Arduini, R.F., Baum, B.A., Minnis, P., Goldman, A., Abrams, M.C., Zander, R., Mahieu, E., Salawitch, R.J., Michelsen, H.A., Irion, F.W., and *Newchurch, M.J.*,1998: ATMOS/ATLAS 3 infrared profile measurements of trace gases in the November 1994 tropical and subtropical upper troposphere. *J. Quantit. Spectros. Radiat. Trans.60*, 891–901. https://doi.org/10.1016/S0022-4073(98)00092-2

Rinsland, C.P., Dufour G., Boone, C.D., Bernath, P. F., Chiou, L.,2005: Atmospheric chemistry experiment (ACE) measurements of elevated southern hemisphere upper tropospheric CO, C_2H_6, HCN, and C_2H_2 mixing ratios from biomass burning emissions and long-range transport. *Geophys. Res. Lett.32*, L20803.https://doi.org/10.1029/2005GL024214

Rodgers, C.D., 2000. Inverse methods for atmospheric sounding: theory and practice (Vol. 2). World scientific.

Shannon, C.E. and Weaver, W., 1962. The mathemtical theory of communication. Paperback edition, University of Illinois Press, Urbana.

Singh, H.B., Salas, L.J. and *Cavanagh, L.A.*,1977: Distribution, sources and sinks of atmospheric halogenated compounds. *J. Air Pollut. Cont. Assoc.27*, 332–336. https://doi.org/10.1080/00022470.1977.10470427

Singh, H.B., Salas, L., Herlth, D., Kolyer, R., Czech, E., Viezee, W., Li, Q., Jacob, D. J., Blake, D., Sachse, G., Harward, C. N., Fuelberg, H., Kiley, C. M., Zhao, Y., and *Kondo, Y.*,2003: In situ measurements of HCN and CH_3CN over the pacific ocean: Sources, sinks, and budgets. *J. Geophys.Res. 108*, 8795.https://doi.org/10.1029/2002JD003006

Spang, R., Remedios, J.J. and Barkley, M.P., 2004. Colour indices for the detection and differentiation of cloud types in infra-red limb emission spectra. Advances in Space Research, 33(7), pp.1041-1047.

Sze, N.D., 1978: Stratospheric fluorine: A comparison between theory and measurements. *Geophys. Res. Lett.5*, 781–783.https://doi.org/10.1029/GL005i009p00781

*Tereszchuk, K.A., González Abad, G., Clerbaux, C., Hadji-Lazaro, J., Hurtmans, D., Coheur, P.-F.*and *Bernath, P.F.*, 2013: ACE-FTS observations of pyrogenic trace species in boreal biomass burning plumes during BORTAS. *Atmos. Chem. Phys.13*, 4529–4541. https://doi.org/10.5194/acp-13-4529-2013

Watson, R.T., Meira Filho, L.G., Sanhueza, E., and*Janetos, A.*,1992: Greenhouse gases: sources and sinks. *Climate Change*, 25-46.

Wiegele, A., Glatthor, N., Höpfner, M., Grabowski, U., Kellmann, S., Linden, A., Stiller, G., and *von Clarmann, T.*, 2012: Global distributions of C_2H_6, C_2H_2, HCN, and pan retrieved from MIPAS reduced spectral resolution measurements. *Atmos. Measur. Tech.5*, 723–734. https://doi.org/10.5194/amt-5-723-2012

Yi, Z., Wang X., Sheng G., Fu, J.,2008: Exchange of carbonyl sulfide (OCS) and dimethyl sulfide (DMS) between rice paddy fields and the atmosphere in subtropical china.*Agric.Ecosyst.Environ.123*, 116–124.https://doi.org/10.1016/j.agee.2007.05.011

Zander, R., Solomon, S., Mahieu, E., Goldman, A., Rinsland, C.P., Gunson, M. R., Abrams, M. C. Chang, A. Y., Salawitch, R. J., Michelsen, H. A., Newchurch, M.J., and *Stiller, G.P.*,1996: Increase of stratospheric carbon tetra fluoride (CF_4) based on ATMOS observations from space. *Geophys.Res. Lett. 23*, 2353–2356.https://doi.org/10.1029/96GL00957

DOI:10.28974/idojaras.2023.2.3

IDŐJÁRÁS

Quarterly Journal of the Hungarian Meteorological Service
Vol. 127, No. 2, April – June, 2023, pp. 199–216

Wind speed estimation for the correction of wind-caused errors in historical precipitation data

Tibor Rácz

Hungarian University of Agriculture and Life Sciences
Institute of Environmental Sciences
Department of Water Management and Climate Adaptation

Author E-mail: raczt167@gmail.com

(Manuscript received in final form August 4, 2022)

Abstract— The wind has a significant impact on the accuracy of precipitation measurement in the case of collecting gauges. As widely known, the velocity field of wind suffers a deformation over and around the precipitation gauges, which causes deviations in the measured quantities. This error must be corrected if it is possible. Thanks to numerous researches, correction formulas give tools for adjusting precipitation data in the function of the wind speed and raindrop distribution (DSD) relationship, gauge parameters, and for the case of snow and temperature. The measured intensity of precipitation in historical data allows estimating the DSD, but in most cases, there are no simultaneously measured wind speed data coupled to the historical precipitation data.

Characteristic data of wind speed can be estimated based on the wind speed statistics, and these data can be utilized for the statistical correction of the precipitation measurements. The statistical correction means that the rainfall data can be adjusted with the expected value of the wind speed for a more extended observation period, assuming a stationarity of wind speed statistics for the given location. After the statistical correction, the unique data will not be unbiased, but statistically they will be closer to the actual value, and the correction will be statistically correct in inherited perecipitation cheracteristics, as for example the IDF curves. For this correction, an investigation is necessary to find the adequate wind statistics for the rainfall correction. This paper shows the results of a study about the relation of statistics of wind speeds during precipitation, based on a 10-minute sampling period. The wind speed data were independent of the rain depth (or intensity) data. The result of the study shows that the distribution of wind speeds differs of the wind speed distribution measured in the precipitation events. This difference can be treated easily using the stable rate of the means of these distributions. This result gives a step toward correcting the wind-affected error of historical precipitation data.

Key-words: rainfall, rainfall measurement, historical data, wind-caused error, correction

1. Introduction

The measurement of precipitation, and especially the rainfall intensity, has a significant role in hydrology with relevant effects on technical, agrotechnical and other fields. A lot of research have been performed worldwide related to the adjustment of the data collected in the past decades by some measurement devices.

For some kinds of systematic errors, there are correction procedures, mainly for tipping bucket rain gauges (*Vuerich et al.*, 2009; *Luyckx* and *Berlamont*, 2001) and for the level-measurement-based gauges (*Luyckx* and *Berlamont*, 2002), or also for their partially processed, selected data (*Rácz*, 2021a). These processes target the systematic errors coming from the construction of the gauge. Researchers have studied the under-measurement phenomena caused by the wind in daily or longer sampling period data; meanwhile, this kind of investigation is rare for the sub-daily historical rainfall data. (The adjective 'historical' covers here the data measured before 2000 with several minutes sampling or with analogous, continuously registering devices.)

In 1769, Heberden called attention to the phenomenon that the result of a rain depth measurement in the same site, but in different heights, differ in most of cases. The differences were explained by Jevons in 1861, who proved that deviations occur by a wind-caused error, and since the wind speed changes with the heights, the deviation in precipitation measurements diverge similarly. (*Strangeways*, 2010). The wind-caused error can be disappear by prevention or correction.

The prevention can be achieved by arranging a measurement site (pit gauge) free from wind disturbance or using some solution to diminish the wind effect on the measurement, like the Nipher shield (*Strangeways*, 2010), or as the most advanced result, using an aerodynamically neutral gauge (*Strangeways*, 2010; *Rodda et al.*, 1985; *Folland*, 1985, 1988).

The correction shows a significant advance in daily or longer sampling data from the 1950s (*Sevruk*, 1982, 1985). Intercomparisons and field measurements have been performed in the late 1900s and in the first decades of the 2000 (*Pollock et al.*, 2015, 2018). As the sampling period shortens, the actual rainfall intensity and the drop-size distribution (DSD) have growing importance. The DSD shows a relation with the character of the rainfall and the rainfall intensity, as it was constated in the middle of the 20th century (*Laws* and *Parsons*, 1943; *Marshall* and *Palmer*, 1948). Later, the approach was modified for more detailed temporal models, using Gamma distribution in the DSD (*Ulbrich*, 1983; *Ulbrich* and *Atlas*, 1984; *Williams et al.*, 2014).

The wind effect depends on the aerodynamical character of the rain gauges, so it is different in the case of different devices. The loss or correction function should be determined to correct the historical rainfall data at least for the most extensively used gauges. These functions can be determined by wind tunnel

experiments and by computational fluid dynamics (CFD) modeling. These experiments were done for a limited group of gauges during the past decades. Many researchers have studied this field, and they took steps forward in the research on the wind effect (*Strangeways*, 2010). In the 1980s, Folland reached significant results using a simplified mathematical model of the wind-caused loss in 2D and 3D cases (*Folland*, 1985, 1988). Particle transport process was investigated in wind tunnels and by CDF models to determine the relation to approach the losses of devices (*Ralph* and *Barret*, 1984; *Nešpor*, 1996; *Nešpor* and *Sevruk*, 1999; *Habib et al.*, 1999; *Cauteruccio* and *Lanza*, 2020).

Duchon and Essenberg compared the results of a free-standing tipping bucket gauge, a weight measurement-based gauge, Nipher-shielded gauges, and a pit gauge (*Duchon* and *Essenberg*, 2001).

Vuerich and his colleagues performed intercomparison measurements during the fourth campaign of the WMO, focusing mainly on the systematic errors of the unique gauges (*Vuerich et al.*, 2009). According to their experimental results, they found the wind-caused error lower than the sum of the measurement inaccuracy of the given rain gauge and the pit gauge used as a reference. This consideration can be satisfying for highly accurate, ultimately used gauges, but in the case of the historical data and the less accurate devices, efforts must be made to adjust the wind-caused errors. Adjusting historical data would be important to ensure more accurate reference data to the investigation of crucial issues such the climate change.

Since 2010, there has been continued field experiment in Norway by Wolff and his colleagues to determine the measurement issues of solid and fluid precipitation. They constructed a correction formula using standard meteorological stations' precipitation, wind speed, and air temperature data (*Wolff et al.*, 2015). As the result of the experiment, a correction factor, *CF* and a catch efficiency value, *CE* have been developed. Kochendorfer's research team used this result to process a data series registered between 2009–2014 (*Kochendorfer et al.*, 2017a). Based on the results, they proposed a less complex correction equation. The investigation has also been performed on six further rain gauges (*Kochendorfer et al.*, 2017b).

As a general formula, the correction factor can be written as the function of the w wind speed, the *DSD*, the p set of device-dependent aerodynamical parameters, and the t temperature. The air temperature data is to separate the solid and fluid phases of precipitation, in the formulas adequate to make this distinction:

$$CF = F(w, DSD, p, t) \ . \tag{1}$$

As it can be considered, there has been a significant development in the field of wind-caused rainfall measurement issues, but for the devices used in the 20th century, the determination of the *CF* is not performed yet.

To achieve an adequate correction in the application of Eq.(1), it is necessary to have highly detailed temporal resolution wind speed data (highly detailed wind speed, HDWS) and rain depth data with a similar (or better) sampling. In the case of historical data, there is no way to complement the data series with wind speed in the necessary resolution, so the adjustment of the high temporal resolution precipitation data is going to be performed with statistical methods.

The statistical correction results in an adjusted dataset from the point of view of statistical parameters, but it does not result in a corrected time series, since the wind data can only be assumed. Corrections can be used for the processed data products, such as the IDF curves, where the corrected data can provide more realistic information. The statistical correction can be applied for a unique gauge, using the locally measured wind speed's statistics to the locally measured historical data, or using a regionally accepted wind statistics of another station, assuming the temporal and spatial stationarity of the wind speed statistics.

2. Materials and method

2.1. Mathematical considerations

Let t be a 1–30 minutes long sampling period of rain and wind speed observations. Let w be the wind speed data of some t (HDWS data), as an independent and identically distributed (iid) random variable with a probability density function (PDF) as its $f(w)$ function. Let, furthermore, r be the wind speed of those t periods when rainfall has occurred (P-HDWS data) with its PDF $f(r)$. Let us assume that the probability distributions of both variables are time-invariant. For the t intervals of precipitation more than 0 mm, a conditional PDF can be written as

$$f(w|r) = (f(wr))/(f(r)) \, . \tag{2}$$

If w and r are independent, then

$$f(w|r) = f(w) \, . \tag{3}$$

In this case, the cumulative distribution function (CDF) of the wind speed measured in the t sampling period is identical to the CDF of wind speed data of every t period, and the correction can be performed with the statistics of w data, regarding Eq.(3).

If the independence of both variables cannot be verified, further analysis is necessary to find some statistical relationship between the statistics of w and r variables. In this case, some kind of proportional relation is to be found, so

$$f(w|r) \quad \propto \quad f(w) \tag{4}$$

The only remaining question is, in this case, the mathematical character of proportionality.

In practice, samples of w and r are available. Let us assume, that the data were recorded in the same sampling period. The arithmetic means of the w and r variables can be calculated.

The arithmetic mean of a specific data population's sample is the unbiased estimation of the expected value of the real probability distribution of the given population. When we got a wind speed time series of a given station, we have only one sample for the data population, because some 10 km distance stations' wind speed data can show a statistically significant difference. It means that we have only one sample for every station, although the number of elements can be in the magnitude of 10^4–10^5. The consequence of Glivenko's theorem is that if the number of elements is high enough, the arithmetic mean of the sample is a good estimation of the real CDF's expected value (*Reimann*, 1989). Similarly, the median is a good estimation of the real CDF's median. However, the standard deviation (SD) is a biased estimation of the variation, in such a high number of the elements, the estimation with SD can be accepted too.

Following the above described way, data series of the investigated stations with similar length can be analyzed, and inferences can be found between the general wind statistics and the rainy wind speed statistics.

Since there are several ways of modeling the real CDF of the wind speed data (*Shi et al.*, 2021), and the selection of method depends on specific targets or toolkits of a well defined task, in this study the distribution fitting was not performed.

2.2. The planned steps of the research

As mentioned in the Section 1, for the historical data, the possible way of adjusting wind-caused error is the statistical correction of data. The correction cannot restore the realistic rainfall data for every investigated moment, but it modifies the data to set them closer to the most probable (realistic) value. The correction will be precise in the statistical parameters of the resulting dataset.

The primary hypothesis for the statistical correction comprises the following surmises:

1. A database with high temporal resolution wind speed and rain depth data is available.
2. Let us surmise that the wind statistics are robust; they change in time slowly, if they change at all.
3. Let us surmise that the conditional probability relation between statistics of wind speed (HDWS) and wind speed during rainfall events (P-HDWS) is robust.

This way, the expected value of the wind speed for the rainfall adjustment is estimable.

From the HDWS data series, the P-HDWS data subseries can be selected by the similar sampling period of a known data series. It is given in the majority of the presently used meteorological stations. The further steps are detailed in this Section. In the investigation, some of the statistical parameters of the homogenized data series have been studied, and a conclusion can be made. The flow chart of the research is shown in *Fig. 1*:

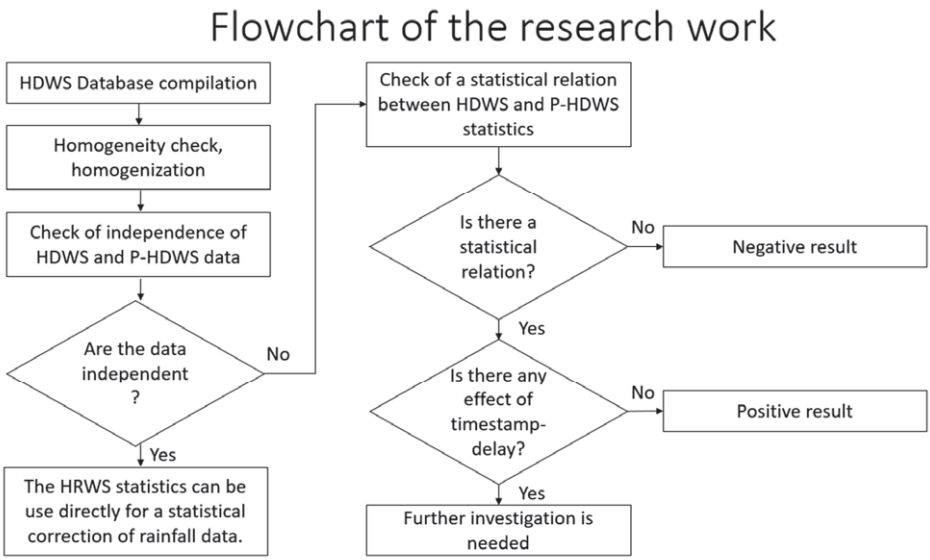

Fig. 1. Flowchart of the present research.

There are three possible favorable outputs of the research. The most favourable would be if the independence of HDWS and P-HDWS data were verified. If the data are not independent, a further investigation is needed to find some mathematical (statistical) relation between the relevant parameters (mean, median, standard deviation) of both data series. There is also a possible negative output if a later detailed problem of data would not be solvable.

2.3. Data description

The origin of the data is the Climate Data Center of the German Weather Service. The selected data comprise 10 minutes sampled wind speed and rain depth. The length of the time series could have reached 30 years, but for better homogeneity of a later analysis of rain depth data, the 2010–2019 years were selected, only because a similar type of rain gauge was used for all stations. The metadata of the time series is available, and papers show the applied methods of the data quality check process (*Kaspar et al*., 2013). The quality check has occured in several

steps, using manual and automatized procedures. The wind speed measurement was performed by Windsensor Classic 4.3303 and 3D Ultrasonic Anemometers.

The homogeneity testing could not have been performed for the higher resolution then one month, and the better-detailed data were homogenized using the correction of the monthly inhomogeneities. The available metadata is adequate to surmise some inhomogeneities, such as the change of instrument or the moving of the meteorological station.

According to the metadata, there is a delay between the wind speed and rain depth data, so its probable effect is to be investigated. The cause of this delay is that the rain depth measurement in these time series was performed with a real-time (RT) or a non-real-time (NRT) method. Before 2008, the applied rain gauges used the RT method, where the delay depended on the rainfall intensity. The delay of data registration in high-intensity rain has been some seconds only, but by the decreasing of the intensity, the time delay could have grown even to several minutes, in some situations reaching the 30 minutes value. Since 2008, the rain gauges were changed to OTT Pluvio devices, which follows the NRT method of measurement with 5 minutes delay, so the time delay has become constant.

The investigated data were collected in 116 stations. The location of the stations is shown in *Fig. 2.*

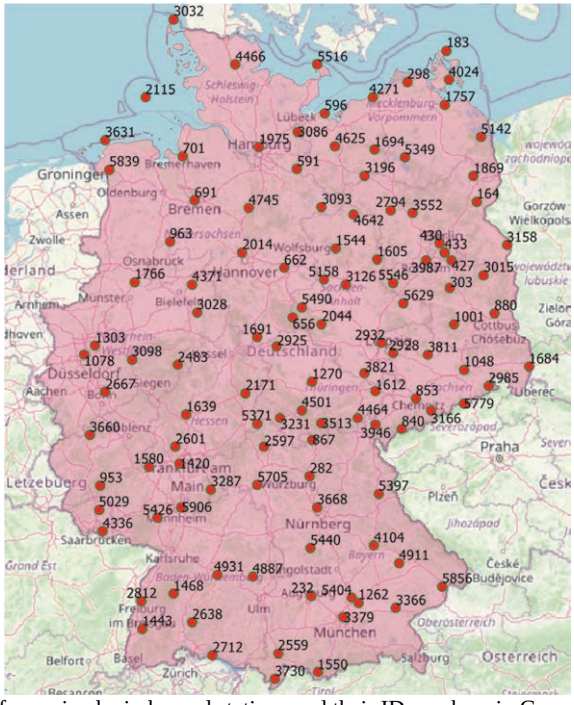

Fig. 2. Map of examined wind speed stations and their ID numbers in Germany.

2.4. Homogeneity and homogenization of data

For testing the homogeneity and for correction of the casual inhomogeneities, the MASH package was used (*Szentimrey*, 2014). The MASH is a relative homogeneity test, so the investigation is based on a simultaneous analysis of several time series measured in the same period but in different stations. For the test, in the case of homogeneity, the similarity of changes in statistical parameters is assumed in the meteorological station close to each other. The analysis takes into consideration the relative distance of the investigated stations. If any inhomogeneity can be observed, its position in time and its measure can be known, so the necessary correction can be performed. The analysis was done for the monthly average wind speed values, and the corrections were redistributed onto the 10-minute data.

2.5. Investigation of HDWS and P-HDWS statistics

Based on the homogenized data, the empirical frequency curve and some chosen statistical parameters of the HDWS data can be determined. The same is to be performed with the P-HDWS data. Comparing the two statistics, the identicalness of the HDWS and P-HDWS data, their independence can be judged, with its consequence, following the flow chart.

2.6. Investigation of the time delay of wind and precipitation measurements

The metadata of the wind and rainfall measurement shows that in reality, the 10-minute rain data is related to a 5 minutes earlier ending 10-minute period. Since this issue can affect the goodness of the investigation, a check was made about it.

The effect of time delay on P-HDWS data was investigated in all data. The comparison was extended to the mean, median, and standard deviation. The examined time shifts were 10 minutes back and forward, and 1440 and 2880 minutes forward.

3. Results and discussion

3.1. Homogeneity examination and homogenization

For the investigation, those data were used only, where both wind speed and rain data were available. Those data, where any of wind or rain data was unavailable (NA signed data), were not considered.

In the examination of the homogeneity, 25 of the 116 investigated time series were found homogenous. The 91 further time series were homogenized.

3.2. Independence of HDWS and P-HDWS data

The frequency curve of the HDWS and P-HDWS data were made using 0.1 m/s clusters. The mean, median, and standard deviation of both group of data were determined.

To demonstrate the results, the empirical frequencies of the HDWS and P-HDWS data of station No. 5705 (49.7704 °N, 9.9576 °E, Würzburg) are presented (*Fig. 3*). At the first glance, a difference can be seen between the empirical frequency curves. In P-HDWS data the rate of higher wind speeds is higher, so the mass of the plot is shifted towards the higher values, so the mean and the median are higher than at HDWS data (*Table 1*).

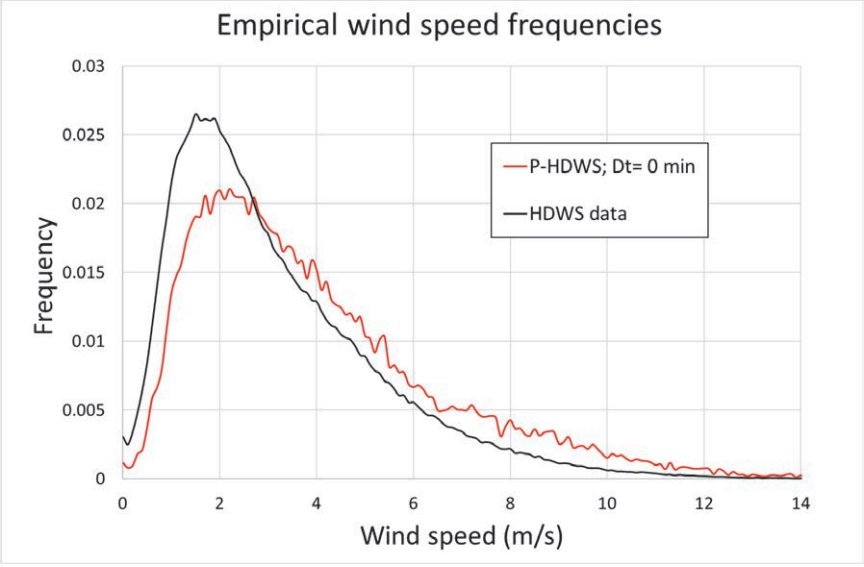

Fig. 3. Wind speed frequencies of station No.5705 (Würzburg) in 2010–2020.

Table 1. Statistical parameters of the complete dataset and the precipitation data of station No.5705

Data	**HDWS data**	**P-HDWS data**
Number of data	524841	30686
Mean (m/s)	3.19	4.01
Median (m/s)	2.60	3.40
SD	2.15	2.57

The results show that the statistics of the HDWS and P-HDWS data are different, so the conditional probability of the investigated 10-minute data is not identical to that of the HDWS data. The statistics of the HDWS data cannot be used directly to correct the wind-caused error.

The result of the investigation for the other stations is similar, with some spreading of course. There was only one station, where the P-HDWS's mean was lower than the HDWS's (No.1550). This station is situated in a relatively deep valley in the Bayern Alps.

The means of P-HDWS data are presented in *Fig. 4*. The spatial distribution of the means resembles the earlier investigations of wind speed distribution surveyed and modeled for wind energy production (*Blankenhorn* and *Resch*, 2014).

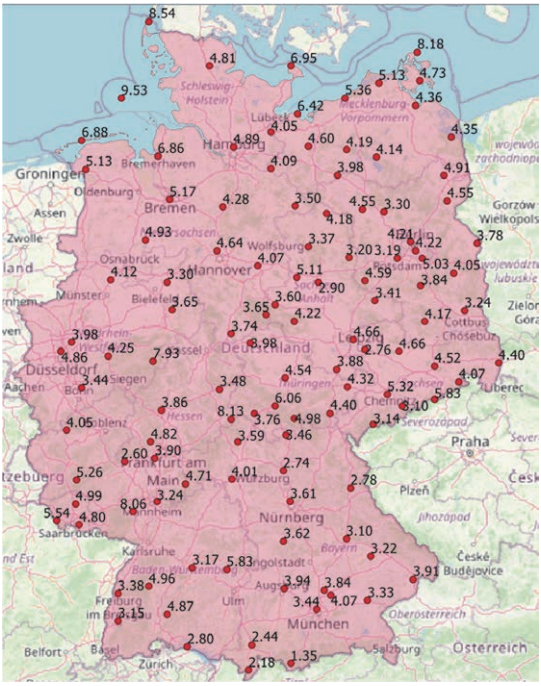

Fig. 4. Means of P-HDWS statistics of the investigated stations.

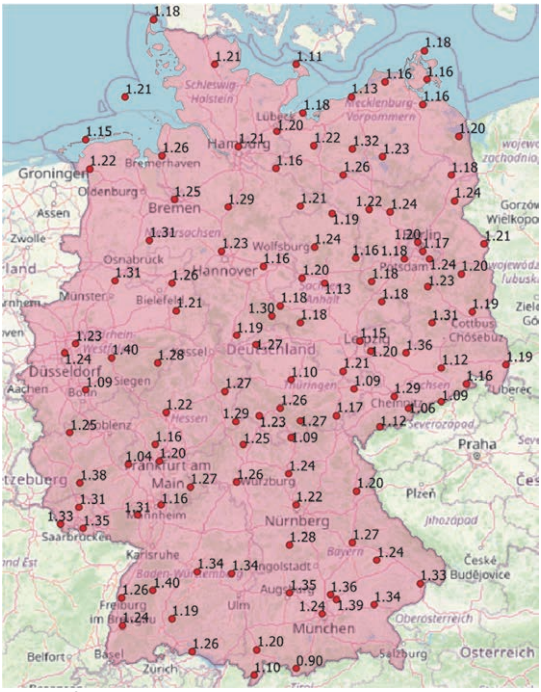

Fig. 5. Rate of means of P-HDWS and HDWS data.

Fig. 5 shows the spatial distribution of the rates of P-HDWS and HDWS values. The values do not depend significantly on the station's latitude, longitude, or geodetic height data. The most frequent values are around 1.20–1.25, with some low and high-value spots in this average field. Interestingly, nearby the river Danube in Bavaria, a consequent 1.30–1.35 value can be observed.

The further step of the investigation was a searching for a statistical relation between the HDWS and P-HDWS data. In this phase, regression has been looked for. On the plot of the data, strong linear regression can be seen in the case of the means (*Fig. 6*). A similar result can be found for the medians (*Fig. 7*) and SD values (*Fig. 8*). The regression lines have a convincing correlation for the three parameters in the 94–96% range.

The linear regression equations for the means, medians, and SDs are

$$MEAN_{P-HDWS} = 1.1952 \cdot MEAN_{HDWS} + 0.0915\,, \tag{4}$$

$$MEDIAN_{P-HDWS} = 1.2106 \cdot MEDIAN_{HDWS} + 0.1551\,, \tag{5}$$

$$SD_{P-HDWS} = 1.1590 \cdot SD_{HDWS} - 0.0799\,. \tag{6}$$

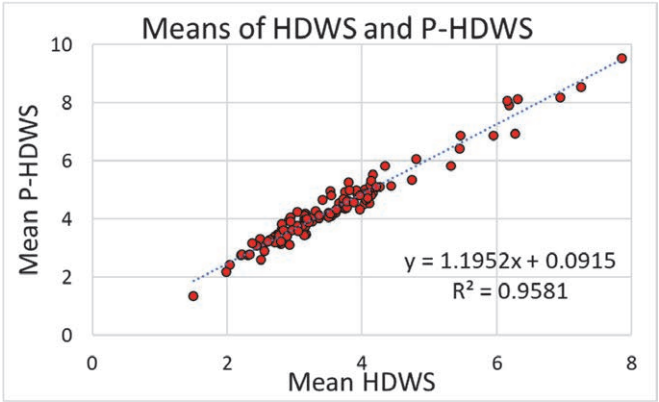

Fig. 6. Comparison of coupled Means of HDWS and P-HDWS data.

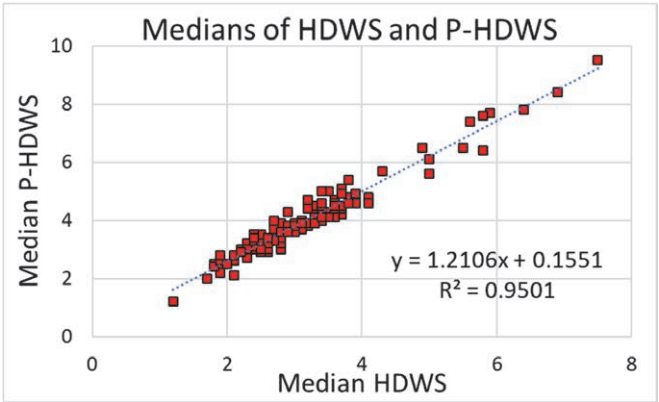

Fig. 7. Comparison of coupled Medians of the HDWS and P-HDWS data.

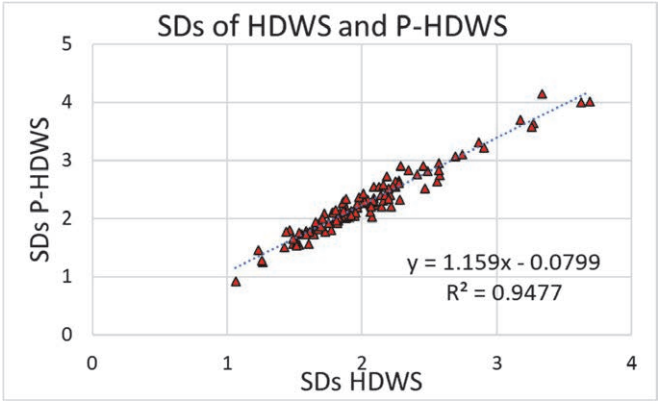

Fig. 8. Comparison of coupled Standard Deviations of the HDWS and P-HDWS data.

Another question was the stability of the statistics. In order to get information about it, the relation between means and medians of the unique station's P-HDWS data were investigated. The data showed pretty strong linearity with 0.9922 steepness and a 99% correlation, so the rate between the means and medians was quasi-stationary in the range of the investigated data. The difference between the means and medians is -0.29 m/s (*Fig. 9*).

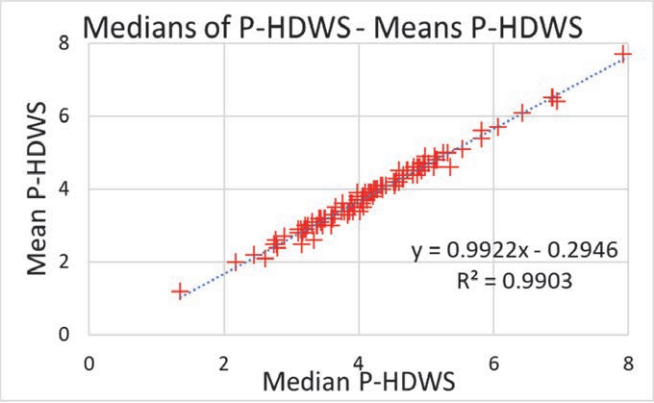

Fig. 9. Regression between the medians and means of P-HDWS data.

Geographical relation with latitude, longitude, and height above sea level with the means of P-HDWS values and rate of P-HDWS and HDWS means was not found. It means that other local factors influence the variability of the means and the rate of means.

Based on the investigations, a strong linear correlation can be constated between the HDWS and P-HDWS data. The linearity of the relationship between means and medians (with the linearity of the SD) gives hope that a fitted CDF of the parameters show the same relationship.

Supposing that the wind speed data is stationary for extended periods, Eq.(4) can be used to determine the mean of wind speeds for the correction of the wind-caused error of 10-minute sampled historical precipitation data, possessing the adequate correction factor function (e.g., Eq.(1)).

The possibility of correction is also valid for those precipitation data in which measurement records can be reshaped to 10-minute sampled data format. For different sampling periods, the investigation must be repeated to determine a relation of means of HDWS and P-HDWS data, of course.

3.3. The effect of time delay between wind and precipitation data

As it was shown in metadata, the precipitation data were detected in a 5-minute time delay, so the theoretical coincidence of the measurements was not correctly fulfilled. It was necessary to analyze the effect of this time delay, demonstrating how it influences the statistical parameters.

Shifting data by 5 minutes was impossible, since the dataset contains 10-minute data only. The possible least shift of data can be 10 minutes. For the first, the -10 and +10 minutes shifted datasets were produced. The three dataset's statistical parameters were calculated, and these are shown in *Table 2* for the station No.5705.

Table 2. Statistical parameters of P-HDWS data with Dt minutes time shift of wind speed data, station No.5705

Parameters	**Dt = -10 min**	**Dt = 0 min**	**Dt = 10 min**
Number of data	30686	30686	30686
Mean	3.91	4.01	3.95
Median	3.30	3.40	3.30
SD	2.54	2.57	2.53

As the statistical parameters show, the parameters of the shifted datasets have decreased for both shifted datasets. For the case of some minutes shift, the similarity of wind data can be assumed; the wind characteristics may have been similar to the P-HDWS data, independently of the backward or forward direction of shifting. The frequencies of maximum wind speeds increased as the time was shifted (*Fig. 10*).

When the time shift has been chosen to be more extended (1440 and 2880 minutes, so one and two days) than the characteristic precipitations, the frequencies are getting closer to the statistics of HDWS data (*Fig. 11*). The cause of this effect can be that the wind data coincided with the non-precipitation periods in most cases.

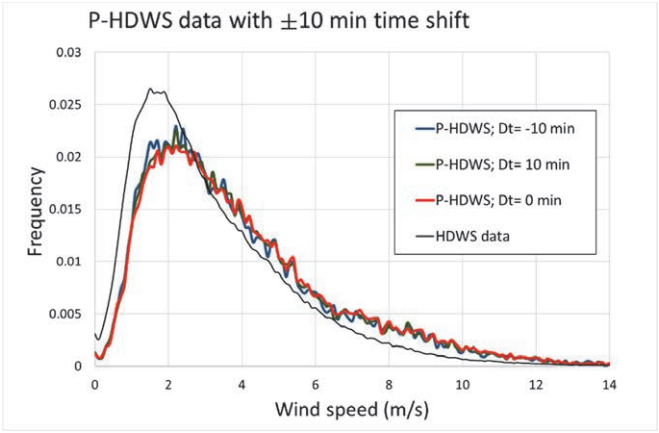

Fig. 10. PHDWS data with ±10 min time shift, station No.5705.

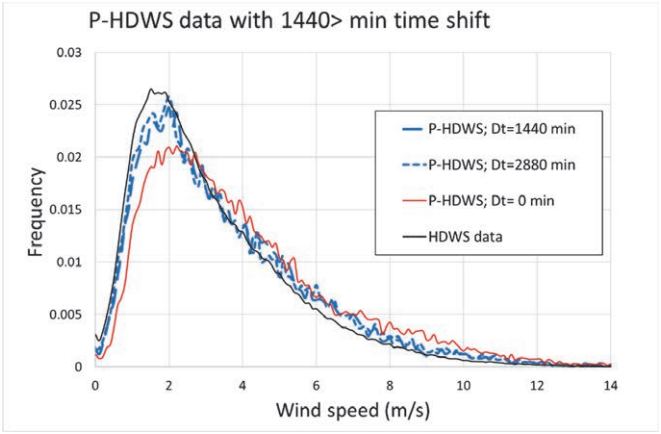

Fig. 11. P-HDWS data with 1440 and 2880 min time shift, station No.5705.

Fig. 12 presents the means of variously shifted P-HDWS data. As the investigated data show, the non-shifted data resulted in the highest mean, and for the means of shifted data by -30 to 160 minutes, lower means can be observed. This decrease of the value, however, are not cosequent, the non-shifted value seems to show an exeptional position. The result does not verify a need of time shifting in the investigation. The results show that the P-HDWS data seems to be adequate for the investigation despite the 5 minutes of data shifting between the HDWS and P-HDWS data.

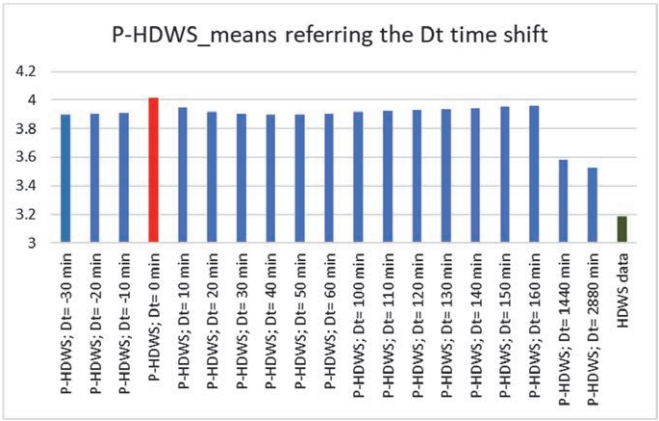

Fig. 12. Ratio of P-HDWS and Dt shifted P-HDWS means, red column: not shifted P-HDWS data; green column: HDWS data, station No.5705.

4. Consequences and further investigations

The investigation results demonstrate that the HDWS statistics cannot be used as a substitution for the P-HDWS statistics in Germany. Further study is needed to proove a generality of this result. The investigation resulted in a robust linear regression between the two statistics for the mean, the median, and the standard deviation. The correlation between the investigated parameter couples is around 95%. Since the arithmetic mean of a large sample is the unbiased estimate of the real distribution's expected value, the mean can be used directly in the ultimately developed correction formulas to adjust statistically the effect of the wind-caused bias of precipitation measurements. Despite that the proposed procedure does not supply corrected time series, the statistical parameters of the adjusted data are good estimations of them.

If there is no wind data for a certain location, the neighboring station’s wind data, or a reginally accepted value can supply an acceptable arithemtic mean for the statistical correction, if the neighborhood stations’s wind data are acceptabe for this approach, regarding the distance and geographic circumstances. For those stations, where the wind statistics are available, the correction can be performed easily by the poposed method.

For the correction of the historical data, the determination of the correction factors for the earlier used gauges is necessary. For this aim, model experiments or CDF modeling must be done.

Another essential point must be taken care of during the further data processing, such as the inaccuracy by the several minutes long sampling period data. This effect can result in underestimating of wind speed and precipitation data (*Rácz,* 2021b). The correction of this kind of error is not solved yet. Despite these

issues, the proposed statistical correction method for the wind-caused error assists in achieving more accurate historical precipitation and rainfall intensity data.

Funding: The research was performed without external funding.

References

Blankenhorn, V. and *Resch, B.*, 2014: Determination of suitable areas for the generation of wind energy in Germany: potential areas of the present and future. ISPRS *Int. J. Geo-Inf. 3*, 942–967. https://doi.org/10.3390/ijgi3030942

Cauteruccio, A. and *Lanza L.G.*, 2020: Parameterization of the collection efficiency of a cylindrical catching-type rain gauge based on rainfall intensity. *Water 12*, 3431. https://doi.org/10.3390/w12123431

Duchon, C.E. and *Essenberg, G.R.*, 2001: Comparative rainfall observations from pit and aboveground rain gauges with and without wind shields. *Water Resour. Res. 37*, 3253–3263. https://doi.org/10.1029/2001WR000541

Folland Ch.K., 1985: A simple numerical model of the loss of rainfall due to wind from a conicallly-shaped collector and a suggested new collector shape. Proc. ETH/WMO/IAHS Workshop on Correction of Precipitation Measuremnts, Zurich, 1-3 April, 1985, WMO TD No104, 233–238.

Folland Ch.K., 1988: Numerical models of the raingauge exposure problem, field experiments and improved collector design. *Quart. J. Roy. Meteorol. Soc. 114*, 1485–1516. https://doi.org/10.1002/qj.49711448407

Habib, E., Krajewski, W.F., Nešpor, V., and *Kruger, A.*, 1999: Numerical simulation studies of rain gage data correction due to wind effect. *J. Geophys. Res. 104*, 19723–19733. https://doi.org/10.1029/1999JD900228

Kaspar, F., Müller-Westermeier, G., Penda, E., Mächel, H., Zimmermann, K., Kaiser-Weiss, A., and *Deutschländer, T.*, 2013: Monitoring of climate change in Germany – data, products and services of Germany's National Climate Data Centre. *Adv. Sci. Res., 10*, 99–106. doi:10.5194/asr-10-99-2013. https://doi.org/10.5194/asr-10-99-2013

Kochendorfer, J., Rasmussen, R., Wolff, M., Baker, B., Hall, M.E., Meyers, T., Landolt, S., Jachcik, A., Isaksen, K., Brækkan, R., and *Leeper, R.*, 2017a: The quantification and correction of wind-induced precipitation measurement errors. *Hydrol. Earth Syst. Sci., 21*, 1973–1989. https://doi.org/10.5194/hess-21-1973-2017

Kochendorfer, J., Nitu, R., Wolff, M., Mekis, E., Rasmussen, R, Baker, B., Earle, M.E., Reverdin, A., Kai, W., Smith, C.D., Yang, D., Roulet, Y-A., Buisan, S., Laine, T., Lee, G., Aceituno, J.L.C., Alastrué, J., Isaksen, K, Meyers, T., Brækkan, R., Landolt, S., Jachcik, A., and *Poikonen, A.*, 2017b: Analysis of single-Alter-shielded and unshilded measurements of mixed and solid precipitation from WMO-SPICE. *Hydrol. Earth Syst. Sci., 21*, 3525–3542. https://doi.org/10.5194/hess-21-3525-2017

Laws, J.O. and *Parsons D.A.*, 1943: The relation of raindrop size to intensity. *Transact. Amer. Geophys. 24*, 452–460. https://doi.org/10.1029/TR024i002p00452

Luyckx, G. and *Berlamont J.*, 2001: Simplified method to correct rainfall measurements from tipping bucket rain gauges. In (Eds.: *Brashear, R.W.* and *Maksimovic, C.*) Urban Drainage Modeling. 767–776. https://doi.org/10.1061/40583(275)72

Luyckx, G. and *Berlamont J.*, 2002: Accuracy of siphoning rain gauges. In (Eds.: *Strecker, E.W.* and *Huber, W.C.*) Global solutions for urban drainage. 1–12. https://doi.org/10.1061/40644(2002)251

Marshall, J.S. and *Palmer, W.McK.*, 1948: The distribution of raindrops with size. *J. Meteorol. 5*, 165–166. https://doi.org/10.1175/1520-0469(1948)005<0165:TDORWS>2.0.CO;2

Nešpor, V., 1996: Investigation of wind-induced error of precipitation measurements using a three-dimensional numerical simulation. Zürcher Geographische Sehriften 63.

Nešpor, V. and *Sevruk, B.*, 1999: Estimation of wind induced error of tainfall gauge measurements using numerical simulation. *J. Atmos. Ocean.Technol. 16*, 450–464. https://doi.org/10.1175/1520-0426(1999)016<0450:EOWIEO>2.0.CO;2

Pollock, M., Colli, M., O'Donnel, G., Black, A., Stagnaro, M., Dutton, M., Lanza, L., Quinn, O., and *O'Connell, E.*, 2015: Evaluating wind-induced uncertainty on rainfall measurements by means of CFD modelling and field observations. Rainfall in Urban and Natural Systems, 10th International Workshop on Precipitation in Urban Areas. Pontresina, 1-5 December 2015 (UR15-61) ETH-Zürich. DOI: 10.3929/ethz-a-010549004

Pollock, M.D., O'Donnell, G., Quinn, P., Dutton, M., Black, A., Wilkinson, M.E., Colli, M., Stagnaro, M., Lanza, L.G., Lewis, E., Kilsby, C.G., and *O'Connel, P.E.*, 2018: Quantifying and mitigating wind-induced undercatch in rainfall measurements. *Water Resour. Res. 54*, 3863–3875. https://doi.org/10.1029/2017WR022421

Rácz, T., 2021a: On the correction of processed archive rainfall data of siphoned rainfall. *Időjárás 125*, 513–519. https://doi.org/10.28974/idojaras.2021.3.9

Rácz, T., 2021b: A mintavétel és az adatfeldolgozás szerepe a csapadékmaximum függvények megbízhatóságában és összehasonlíthatóságában. *Hidrológiai közlöny 100*(4), 52–59. (In Hungarian)

Ralph, M.O. and *Barret, C.F.*, 1984: A wind tunnel study of the efficiency of three deposit gages. Warren Spring Laboratory, Stevebage, UK, Rep.Nr. LR 499 (AP).

Reimann, J., 1989: Mathematical statistics with application in flood hydrology. Akadémiai Kiadó, Budapest, 1989. ISBN 963 05 4832 1

Rodda, J.C., Smith, S.W., and *Strangeways, I.C.*, 1985: On more realistic measurements of rainfall and their impact on assessing acid deposition. Proc. ETH/WMO/IAHS Workshop on Correction of Precipitation Measurements, Zurich, 1-3 April, 1985, WMO TD No104, 245–249.

Sevruk, B., 1985: Effect of wind and intensity of rain ont he rain catch. International comparison of national preciptation gauges with a reference pit gauge (Evaluation stations). Proc. ETH/WMO/IAHS Workshop on Correction of Precipitation Measurements, Zurich, 1-3 April, 1985, WMO TD No104, 251–256.

Sevruk, B., 1982: Methods of correction for systematic error in precipitation measurement for operational use. (Operational Hydrology Report No. 21) WMO, Geneva.

Shi, H., Dong, Z., Xiao, N., and *Huang, Q.*, 2021: Wind Speed Distributions Used in Wind Energy Assessment: A Review: Front. *Energy Res. 9*, 769920. https://doi.org/10.3389/fenrg.2021.769920

Strangeways, I., 2010: A history of rain gauges. *Weather 65*(11). 311. https://doi.org/10.1002/wea.726

Szentimrey, T. 2014: Manual of homogenization software MASHv3.03. Hungarian Meteorological Service, Budapest, Hungary.

Ulbrich, C.W., 1983: Natural variations in the analitical form of the raindrop size distribution. *J. Climate Appl. Meteorol. 22*, 1764–1775. https://doi.org/10.1175/1520-0450(1983)022<1764:NVITAF>2.0.CO;2

Ulbrich, C.W. and *Atlas, D.*, 1984: Assessment of the contribution of differential polarization to improved rainfall measurements. *Radio Sci. 19*, 49–57. https://doi.org/10.1029/RS019i001p00049

Vuerich, E., Monesi, C., Lanza, L.G., Stagi, L., and *Lanziger, E.*, 2009: WMO field intercomparison of rainfall intensity gauges. Instruments and observing methods. Report No.99. WMO, Geneve.

Williams, C.R., Bringi, V.N., Carey, L.D., Chandrasekar, V., Gatlin, P.N., Haddad, Z.S., Meneghini, R., Joseph Munchak, S., Nesbitt, S.W., Petersen, W.A., Tanelli, S., Tokay, A., Wilson, A., and *Wolff, D.B.*, 2014: Describing the Shape of Raindrop Size Distributions Using Uncorrelated Raindrop Mass Spectrum Parameters. *J. Appl. Meteorol. .53*, 1282–1296. https://doi.org/10.1175/JAMC-D-13-076.1

Wolff, M.A., Isaksen, K., Petersen-Øverleir, A., Ødemark, K., Reitan, T., and *Brækkan, R.*, 2015: Derivation of a new continuous adjustment function for correcting wind-induced loss of solid precipitation: results of a Norwegian field study. *Hydrol. Earth Syst. Sci. 19*, 951–967. https://doi.org/10.5194/hess-19-951-2015

DOI:10.28974/idojaras.2023.2.4

IDŐJÁRÁS

Quarterly Journal of the Hungarian Meteorological Service
Vol. 127, No. 2, April – June, 2023, pp. 217–231

Analysis of the correlation between the incidence of food-borne diseases and climate change in Hungary

Tímea Kocsis [1,*], **Kinga Magyar-Horváth** [2], **Zita Bihari** [3], and **Ilona Kovács-Székely** [4]

[1] *Eötvös Loránd University Faculty of Science,*
Centre of Environmental Sciences
H-1117 Budapest, Pázmány Péter sétány 1/A

[2] *Budapest Business School - University of Applied Sciences*
Faculty of Commerce, Hospitality and Tourism
Department of Hospitality
H-1054 Budapest, Alkotmány utca 9-11.

[3]*Hungarian Meteorological Service*
H-1024 Budapest, Kitaibel Pál utca 1.

[4]*Budapest Business School - University of Applied Sciences*
Faculty of Commerce, Hospitality and Tourism
Department of Methodology for Business Analysis
H-1054 Budapest, Alkotmány utca 9-11.

**Corresponding author E-mail: timea.kocsis@gmail.com*

(Manuscript received in final form July 11, 2022)

Abstract— It is increasingly accepted globally, that many food-borne diseases are associated with climate change. The goal of the present research is to investigate whether changes in the annual number of the registered food-borne diseases in Hungary can be correlated to any climate parameter, as it is reasonable to suppose that it can be linked to climate change. Ten climate parameters and indices were examined as potential influencing factors. A multiple linear regression model was employed, using the backward elimination method to find the climate factors that have a significant effect on the annual number of food-borne diseases. It was found that the annual mean temperature was the only significant predictor of the annual number of registered food-borne diseases, and that 22.0% of the total variance in the annual number of food-borne diseases can be explained by the annual mean temperature. It should be noted that this relationship is negative, given that they are derived from time series with opposite trends. This phenomenon may be explained by the process of evolution and adaptation of the infecting fauna.

Key-words: annual number of food-borne diseases, climate factors, correlation, multiple regression, Hungary

1. Introduction

Probably climate change is one of the most urgent problems of humanity to solve, because it affects several parts of our current way of life. The Sixth Assessment of the *IPCC* (2021) gives accurate details about the physical driving forces of climate change and summarizes the possible effects that it is likely people will have to meet in the future. Global climate change probably cannot be prevented (*Fawzy et al.*, 2020; *van Meijl et al.*, 2018); therefore, adaptation and mitigation are in the priority.

It has long been recognized that increasing food-borne diseases are correlated with climate change through microbial adaptation by natural selection (*van de Venter*, 2000). Climate change should exacerbate the challenges for the public health sector for both food-borne and water-borne diseases (*Cissé*, 2019). Rises in air and water temperature, extreme precipitation events, seasonal changes, and the storms, droughts, and flooding associated with climate change will clearly have implications for food- and water-borne diseases in Europe. One obvious example is the adverse effect of high air temperatures on food quality during transport, storage, and handling (*EEA*, 2016). The most prevalent food-borne disease in Europe is campylobacteriosis, and this is known to be associated with several meteorological variables. Peaks in the incidence of campylobacteriosis may shift in time, as it displays strong seasonality, thereby making it subject to any changes in climate. Rise in temperature also have a pronounced impact on the occurrence of salmonellosis and food poisoning notifications in Europe (*ECDC*, 2012).

A rise in mean global temperature may be expected, bringing about a concomitant increase in the incidence of food-borne diseases (*Cullen*, 2009). The WHO considers that warming and changes in precipitation are already claiming human lives and climate-health relationship pose increasing health risk, as many human diseases are linked to climate fluctuation (*Patz et al.*, 2005) and overexploitation (*Patz et al.*, 2008). Climate conditions strongly affect the incidence and transmission of many water-borne and food-borne diseases (*Schuster-Wallace et al.*, 2014). Changing climate alters the living conditions for every species, and this includes pathogens, and will affect different food-borne parasites in various ways (*Utaaker* and *Robertson*, 2015). Food is a conventional vector for pathogens to reach hosts. Street food is a major source of food-borne diseases, and increasing temperature is likely only to intensify this, by accelerating the growth rates of microorganisms (*Bastien-Olvera et al.*, 2017). *Lake* (2017) examined the likely impact of climate change upon food-borne diseases in the UK and found a strong positive association between *Salmonella* spp. cases and ambient temperature. Infection with *Salmonella* spp. leads to diarrhoea, fever, and abdominal cramps, usually 1–3 days after the initial infection. Symptoms generally last for 4–6 days, but in some cases, the person affected may need to be hospitalized. It must be said, however, that the

relationship between changing climatic conditions and food-borne diseases is still poorly understood (*Kim et al.*, 2015). This relationship and, hence, any impacts on any associated illnesses are uncertain, making it difficult to estimate which pathogens will be affected and what changes might occur (*Lake* and *Barker*, 2018). A linear association can be demonstrated between the environmental temperature and the number of reported cases of *Salmonella* spp. infections above a threshold of 6 °C as found by *Kovats et al.* (2004).

Fluctuations in climatic conditions are a frequent phenomenon in the history of the Earth, but the ongoing climate change is supposed to be accelerated by the human activity. A warming trend may be clearly seen in data obtained by CarpatClim for the Carpathian region between 1961 and 2010 (*Lakatos et al.*, 2016), and temperature extremes show significant changes in the Carpathian region over the same period, in particular the increasing incidence of warm nights (*Lakatos et al.*, 2016). Not only warming is to be projected in the region, but also severe modifications in precipitation (*Kis et al.*, 2017; *Bartholy et al.*, 2015; *Pongrácz et al.*, 2014). Therefore, the intensity and frequency of extreme precipitation events in the region has increased (as measured on the basis of extreme indices) during the 20th century in the Carpathian Basin (*Bartholy* and *Pongrácz*, 2005). Regional climate model outputs suggested that considerably less precipitation should be expected in summer, with a rising frequency of drought. In winter, slightly more rainfall is to be projected. It should be kept in mind that more recent studies warned that hydroclimate projections for East-Central Europe diverge to a great extent, and those models, which better represent land-atmosphere feedbacks actually project less summer drying in the near future (*Topál et al.*, 2020). Modification of the intra-annual distribution of the precipitation is supposed. The frequency of heavy precipitation is projected to decrease in summer, but to rise in the other seasons (*Bartholy* and *Pongrácz*, 2010).

Changes in annual mean temperature projected for the Carpathian Basin based on model runs by four different regional models (ALADIN, REMO, PRECIS, RegCM) are 1.1–1.9 °C for 2021–2050 and 3.1–4.0 °C for 2071–2100 (the reference period is 1961–1990). These model runs projects (-7) – 0% change in annual precipitation to 2021–2050 and (-21) – +3% for 2071–2100 with the same reference period (*Krüzselyi et al.*, 2011).

The aim of the present research is to investigate whether the annual number of registered food-borne diseases may correlate to any climatic factor, as it is supposed that it can be linked to climate change. Ten climate parameters and indices are examined as potential impact factors. While the evolution of food-borne diseases depends on various factors, in this research other potentially influencing factors were not examined.

2. Material and methods

6.1 Data used

The climate data time series were provided by the Hungarian Meteorological Service. These time series were derived from the *CARPATCLIM Database* (2013) and represent extrapolated gridded and homogenized data covering the territory of Hungary for the period 1961–2010. The following climatic data and extreme indices were used: annual mean temperature (°C), annual precipitation sum /R/ (mm), annual mean relative humidity (%), annual total number of days when the daily maximum temperature was higher than 30 °C (days), annual total number of days when the daily minimum temperature was higher than 20 °C (days), annual total of number of days when the daily precipitation sum was higher than 10 mm (days), annual absolute maximum of diurnal precipitation (mm), duration of the longest dry period during a year (days), duration of the longest wet period during a year (days), annual maximum of 5-day-long precipitation sums /RX5/ (mm).

The Hungarian Public Health Service provided the time series of the total annual number of food-borne diseases between 1961 and 2010. Covering a short period between 2011 and 2017, a detailed database also provided information on the number of food-borne diseases classified according to bacteria genus.

6.2 Statistical methods

Multiple linear regression was fitted to the data and backward-elimination method was used, in which the annual total number of food-borne diseases was chosen as the dependent variable. As predictors, the climatic data and climate extreme indices were used. For the details of the statistical method see *Aczel* and *Sounderpandian*, 2006; *Helsel* and *Hirsch*, 2002; *Osborne* and *Waters*, 2002. The goal was to estimate whether the number of food-borne diseases correlated with any of the ten climate factors selected for examination. As a preliminary requirement, the normal distribution of the dependent variable was checked using the Kolmogorov-Smirnov test at a significance level of 5%. The dependent variable fulfilled this requirement. Although it could have been an approach to consider numerous parameters (e.g., *O'Brien*, 2007) to backward eliminate the different predictors, however, the significance of the partial regression coefficient was chosen as the bottleneck parameter at 5% significance level.

3. Results

A multiple linear regression model was used to investigate if any of the predictor parameters have a significant effect on the total annual number of food-borne diseases. Applying the backward-elimination method based to the results of the

t-test's *p*-values, all the while paying attention to the potential multi-collinearity of the predictors, the multiple linear regression model was reduced to a simple linear regression model (*Appendix 1*), in which the annual mean temperature is a significant predictor of the annual number of food-borne diseases. The linear correlation coefficient is -0.486, and therefore, the relationship is negative between variables. The adjusted coefficient of determination means that 22.0% of the variance of the annual number of food-borne diseases is explained by the annual mean temperature (*Appendix 1*). As only one significant independent variable was found among the ten predictors examined, in the course of the final check, the linear relationship between the two variables was explored (*Fig. 1a*), the normal distribution of the residuals was analyzed, and homoscedasticity was visually controlled (*Fig. 1b*). The normality of the residuals was tested using the Kolmogorov-Smirnov test, and it can be accepted that the residuals followed a significantly normal distribution (the *p*-value was 0.2). All these checks fulfilled the requirements.

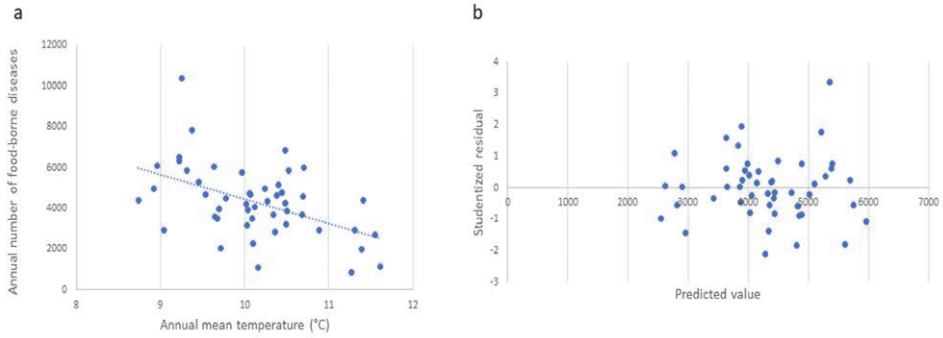

Fig. 1. Linear relationship between the variables (a) and check for homoscedasticity (b).

Between 1961 and 2010, a negative correlation can be detected: as the annual mean temperature rises, the annual number of registered food-borne diseases decreases over the examined time period (*Fig. 2*). Unfortunately, only indirect evidence of this theory can be found as detailed information about the vectors causing food-borne diseases are obtained for the period of 2011–2017.

As the annual mean temperature was the only significant predictor of the annual number of registered food-borne diseases, the question arises of whether the significance of this relationship is enhanced in time. The examined time series was therefore split into two equally long segments. Between 1961 and 1985 the regression model is not significant, and the annual mean temperature as predictor

is not significant. Between 1986 and 2010, however, the regression model is significant at a significance level of 5%, and annual mean temperature is a significant predictor at a significance level of 10%. These results suggest the enhancing influence of annual mean temperature. For the years 1981–2010, annual mean temperature remained the only significant predictor of the annual number of registered food-borne diseases.

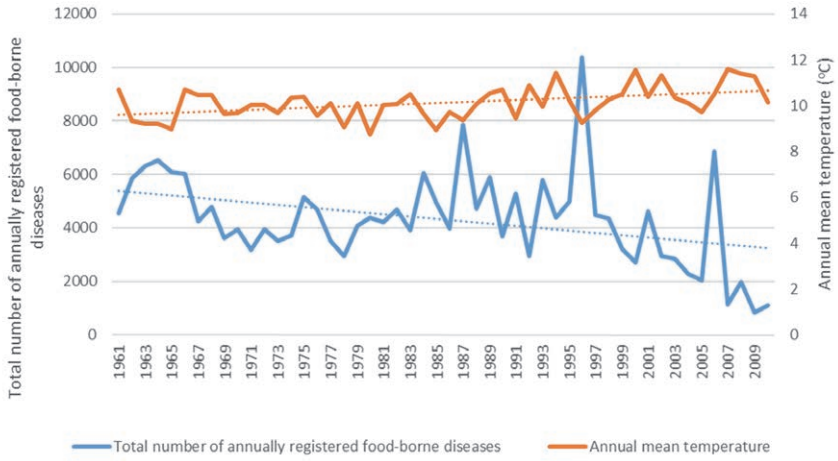

Fig. 2. Tendencies in time of the examined variables.

The share of salmonellosis (light blue) noticeably decreased, while that of the *Calici virus* (dark grey) infections increased with time and between 2015 and 2017 *Clostridium perfingens* (light green) appeared, not having been present previously (*Fig. 3*). Despite the relatively short period for which the detailed data by bacteria genus are available (2011–2017), they clearly indicate a change in the type and frequency of occurrence of bacteria causing food-borne diseases. The *Salmonella* spp. has been the most common food borne disease bacteria in Hungary in recent decades. The frequency of occurrence of salmonellosis decreased during this period, while types of food-borne bacteria previously not encountered locally have appeared. The frequency of occurrence of *Clostridium botulinum* and *Clostridium perfingens* increased between 2015 and 2017. The *Salmonella* spp. is a mesophilic bacterium, but *Clostridium botulinum* and *Clostridium perfingens* are thermotolerant bacteria.

From 2011 to 2017, detailed monthly data on the number of food-borne diseases were provided by the Hungarian Public Health Service. The question arises of whether seasonal patterns can be found in the monthly data that might be linked to temperature changes. The absence of any typical seasonal pattern in the monthly number of food-borne diseases can be seen in *Fig.4*.

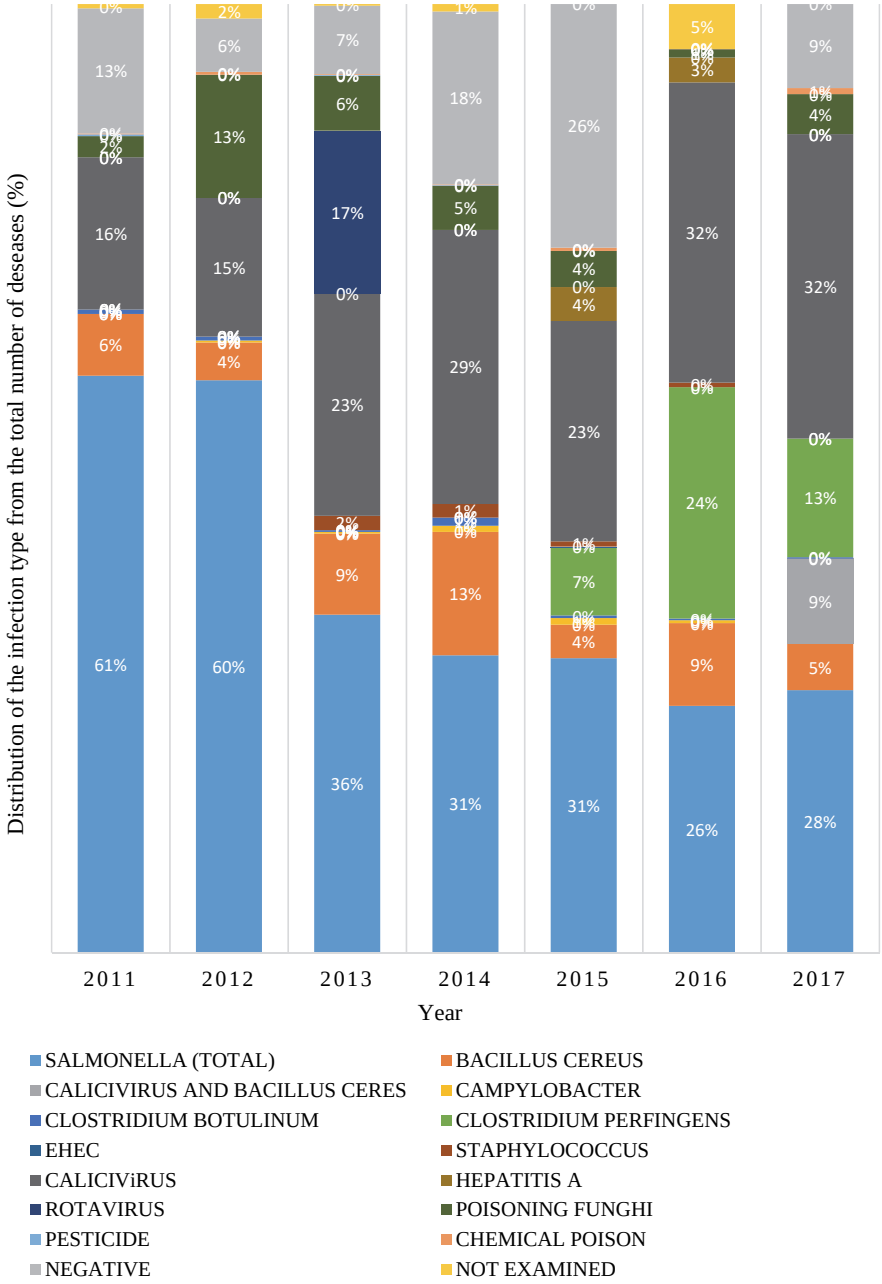

Fig. 3. Distribution of the different infecting vectors in the annual number of registered food-borne diseases.

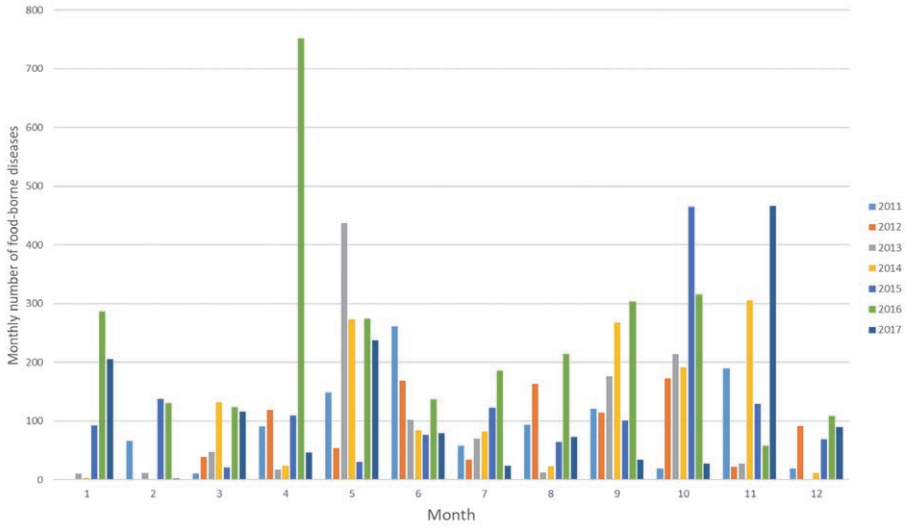

Fig. 4. Monthly number of food-borne diseases year-by-year between 2011 and 2017.

As no typical seasonal pattern can be discerned, an interesting question was to see the changes of the annual distribution of the number of food-borne diseases on a monthly basis, even if the period in question (2011-2017) is short. *Fig. 5* lends some support to the validity of this approach.

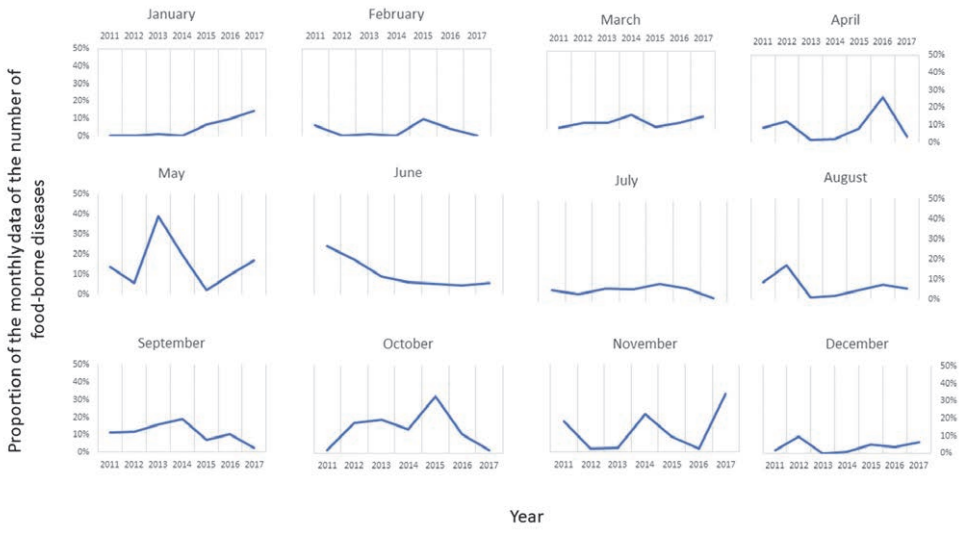

Fig. 5. Proportion (%) of the monthly data of the number of food-borne diseases (2011–2017).

It is interesting to note the varying degrees to which the number of food-borne diseases displays a seasonal pattern, as shown in *Fig. 6*. The seasons are as follows: spring: March, April, May; summer: June, July, August; autumn: September, October, November; and winter: December, January, February. In the seasonal data, temperature rises in the summer and winter may cause favourable conditions in winter and limiting conditions in summer. The proportion of the number of diseases in summer declines, while in winter it increases. These phenomena should be linked to the temperature changes due to climate change.

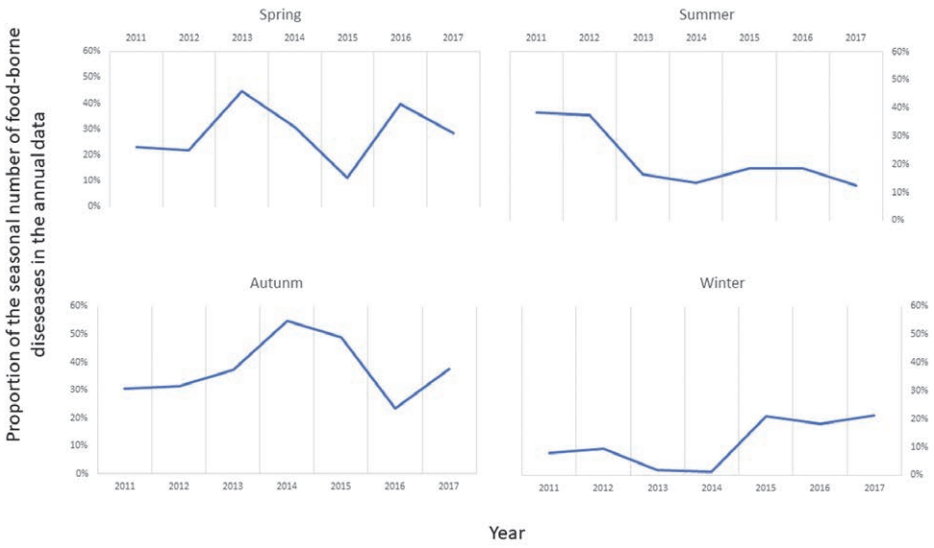

Fig. 6. The proportion of the seasonal number of the food-borne diseases in the annual data (2011–2017).

4. Discussion

A significant relationship has been revealed between the annual mean temperature and the number of food-borne diseases based on annual data (1961–2010). Several studies, mentioned below, have already focused on the relationship between temperature and food-borne diseases, and it has been found that climate change, as well as other factors such as globalization and land cover change, contribute to outbreaks of transboundary animal diseases – some transmissible to humans – that can affect food and nutrition security, as well as livestock rearing and trade. For a better understanding of the processes over time, the dataset of 50 years was divided into two parts (1961–1985 and 1986–2010). The result suggests the

enhancing effect of the annual mean temperature. Because of the explanation of the results, the distribution by the infection type of the annual total number of food-borne diseases was analyzed between 2011 and 2017. Unfortunately, this detailed information had not been registered previously. Between 2011 and 2017, the monthly number of the food-borne diseases was available, besides the annual data. The frequency of occurrence of *Clostridium botulinum* and *Clostridium perfingens* increased between 2015 and 2017. The share of salmonellosis noticeably decreased, while that of the *Calici virus* infections increased with time. Between 2015 and 2017 *Clostridium perfingens* appeared, not having been present previously. Climate change can contribute to bring novel vectors into temperate regions (*Newell et al.,* 2010).

Analyzing the proportion of the seasonal and monthly numbers of food-borne diseases within the annual data, it can be concluded that the rise in temperature is projected to be above yearly average in the winter months, and the ratio of diseases occurring in January is likely to increase rapidly. This may indeed be proof of the influence of rising temperature, as the temperature conditions more closely coincide with those to which the infecting bacteria is accustomed and in which it thrives. In June the ratio decreases. It is reasonable to assume that the summer months are supposed to be warmer and warmer (*Bartholy et al.,* 2011), and therefore, it is possible that this increase in temperature will put it beyond the "comfort zone" of the bacteria which constitute the typical infecting species.

There is a direct correlation between the environment and the organisms from which food is produced and the impact of food safety on human health and economic well-being. Meanwhile, food-borne pathogens in the food chain are affected by complex interactions between the environment, microorganisms, and reservoir hosts (*EC,* 2007). Increases in temperature may speed up the growth of pathogens and/or parasites that exist at least part of their life cycle outside of their host, negatively affecting livestock (*Rojas-Downing et al.,* 2017). Climate change may induce shifts in the pattern of the spread of disease, or even introduce new diseases in areas where livestock had never before been exposed to them (*Thornton et al.,* 2009). Pathogens in charge of human disease can originate in animal stock on farms, from contamination during food processing or transportation, or during the commercial or home preparation of food. There is proof that the growth and dissemination of the accountable microorganisms can be affected by the weather (*MMWR,* 1999, *Rose et al.,* 2000; *Curriero et al.,* 2001, *Rose et al.,* 2001). A study in the United Kingdom found an association between temperature and food poisoning (*Bentham et al.,* 1995).

5. Conclusions

Ten meteorological parameters and extreme indices were analyzed in regression statistics (multiple linear regression backward elimination) to the annual number

of food-borne diseases in Hungary in the period of 1961–2010. The adjusted coefficient of determination was 22.0% and had an increased value in the period 1981–2010. Of the ten parameters examined, only the annual mean temperature was found to be a significant predictor, and then the correlation is negative between the annual mean temperature and the annual number of food-borne diseases. Intra-annual examination could be carried out in depth only for the period of 2011–2017, and it was found that changes in temperature do indeed have an influence on the annual distribution of the number of diseases. Temperature rises in summer and winter are likely to have a twofold effect, in that while they create more favorable conditions in winter for bacteria, they also play a limiting role in summer, as it may be observed in the incidence of food-borne diseases, which is actually declining in summer, but increasing in winter.

The scarcity of the data available is certainly places limits on how definite any conclusions drawn may be, but even this examination of a dataset covering a short period of time gives a clear indication of the changes occurring. While further research is required, as a preliminary conclusion, it may be stated that where there is a rise in temperature, the modification of intra-annual peaks in the incidence of diseases is to be expected.

References

Aczel, A.D. and *Sounderpandian, J.*, 2006: Complete business statistics. McGraw Hill Singapore.

Bartholy, J., Bihari, Z., Horányi, A., Krüzselyi, I., Lakatos, M., Piecka, I., Pongrácz, R., Szabó, P., Szépszó, G., and Torma, Cs., 2011: Hazai éghajlati tendenciák. In (Eds: Bartholy, J., Bozó, L., and Haszpra, L.) Klímaváltozás–2011, 145–234. (in Hungarian)

Bartholy, J. and *Pongrácz, R.*, 2005: Tendencies of extreme climate indices based on daily precipitation in the Carpathian Basin for the 20th century. *Időjárás 109*, 1–20.

Bartholy, J. and *Pongrácz, R.*, 2010: Analysis of precipitation conditions for the Carpathian Basin based on extreme indices in the 20th century and climate simulation for 2050 and 2100. *Phys. Chem. Earth* 35, 43–51.
https://doi.org/10.1016/j.pce.2010.03.011https://doi.org/10.1016/j.pce.2010.03.011

Bartholy, J., Pongrácz, R., and *Kis, A.*, 2015: Projected changes of extreme precipitation using multi-model approach. *Időjárás* 119, 129–142.

Bastien-Olvera, B., Bautista-Gonzalez, E., and *Gay-Garcia, C.*, 2017: An agent-based model of food-borne diseases under climate change scenarios in Mexico City. The risk of street-food in a warming city. Conference paper

Bentham, G.C., and *Langford, I.H.* (1995). Climate change and the incidence of food poisoning in England and Wales. *International Journal of Biometeorology, 39*, 81-86.

CARPATCLIM Database, 2013: Szalai, S., Auer, I., Hiebl, J., Milkovich, J., Radim, T. Stepanek, P., Zahradnicek, P., Bihari, Z., Lakatos, M., Szentimrey, T., Limanowka, D., Kilar, P., Cheval, S., Deak, Gy., Mihic, D., Antolovic, I., Mihajlovic, V., Nejedlik, P., Stastny, P., Mikulova, K., Nabyvanets, I., Skyryk, O., Krakovskaya, S.,Vogt, J., Antofie, T., and Spinoni, J., CARPATCLIM Database © European Commission – JRC, Climate of the Greater Carpathian Region. *Final Technical Report*. www.carpatclim-eu.org

Centers for disease control and prevention: Outbreaks of Escherichia coli O157:H7 infection and Campylobacter among attendees of the Washington Country Fair-New York 1999, *MMWR* Morb Mortal Wkly Rep.48, pp: 868-872.

Cissé, G., 2019: Food-borne and water-borne diseases under climate change in low- and middle-income countries: Further efforts needed for reducing environmental health exposure risks. *Acta Tropica 194*, 181–188. https://doi.org/10.1016/j.actatropica.2019.03.012

Cullen, E., 2009: The impact of climate change on the future incidence of specified foodborne diseases in Ireland. *Epidemiology 20*(6), S227–S228. https://doi.org/10.1097/01.ede.0000362763.61421.93

Curriero, F.C., Patz, J.A., and *Rose, J.B.*, 2001: The association between extreme precipitation and waterborne disease outbreaks in the United States 1948–1994. *Amer. J. Publ. Health 91*, 1194–1199. https://doi.org/10.2105/AJPH.91.8.1194

EC, 2007: Commission staff working document. Annex accompanying the green paper from the Commission to the Council, the European Parliament, the European Economic and Social Committee and the Committee of the Regions. Adapting to climate change in Europe – options for EU action.

ECDC, 2012: Technical Report Assessing the potential impacts of climate change on food- and waterborne diseases in Europe. European Centre for Disease Prevention and Control, Stockholm.

EEA, 2016: Water- and food-borne diseases. European Environmental Agency Copenhagen.

Fawzy, S., Osman, A.I., Doran, J., and *Rooney, D.W.*, 2020: Strategies for mitigation of climate change: a review. *Environ. Chem. Lett. 18*, 2069–2094. https://doi.org/10.1007/s10311-020-01059-w

Helsel, D.R. and *Hirsh, R.M.*, 2002: Trend analysis. In: Techniques of Water-Resources Investigations of the United States Geological Survey Book 4, Hydrologic Analysis and Interpretation Chapter A3: Statistical Methods in Water Resources, 296–305. https://doi.org/10.3133/twri04A3

IPCC, 2021: Summary for Policymakers. In: Climate Change 2021: The Physical Science Basis. Contribution of Working Group I to the Sixth Assessment Report of the Intergovernmental Panel on Climate Change [(eds.: *Masson-Delmotte, V., P. Zhai, A. Pirani, S.L. Connors, C. Péan, S. Berger, N. Caud, Y. Chen, L. Goldfarb, M.I. Gomis, M. Huang, K. Leitzell, E. Lonnoy, J.B.R. Matthews, T.K. Maycock, T. Waterfield, O. Yelekçi, R. Yu, and B. Zhou*]. Cambridge University Press, Cambridge, United Kingdom and New York, NY, USA, 3−32. https://doi.org/10.1017/9781009157896.001

Kim, Y.S., Park, K.H., Chun, H.S., Choi, C., and *Bahk, G.J.*, 2015: Correlation between climatic conditions and foodborne disease. *Food Res. Int. 68*, 24–30. https://doi.org/10.1016/j.foodres.2014.03.023

Kis, A., Pongrácz, R., Bartholy, J., 2017: Multi-model analysis of regional dry and wet conditions for the Carpathian Region. *Int. J. Climatol.* 37, 4543–4560. https://doi.org/10.1002/joc.5104

Kovats, R.S., Edwards, S.J., Hajat, S., Armstrong, B.G,, Ebi, K.L., and *Menne, B.*, 2004: The effect of temperature on food poisoning: a time-series analysis of salmonellosis in ten European countries. *Epidemiol. Infect 132*, 443–453. https://doi.org/10.1017/S0950268804001992

Krüzselyi, I., Bartholy, J., Horán yi, A., Pieczka, I., Pongrácz., R., Szabó, P., Szépszó, G., and Torma, Cs. 2011: The future climate characteristics of the Carpathian Basin based on a regional climate model mini-ensemble. Adv. Sci. Res. 6, 69–73. https://doi.org/10.5194/asr-6-69-2011

Lakatos, M., Bihari, Z., Szentimrey, T., Spinoni, J., and *Szalai, S.*, 2016: Analyses of temperature extremes in the Carpathisn Region in the period 1961-2010. *Időjárás 120*, 41–51.

Lake, I.R. and *Barker, G.C.*, 2018: Climate change, foodborne pathogens and illness in higher-income countries. *Curr. Environ. Health Rep. 5*, 187–196. https://doi.org/10.1007/s40572-018-0189-9

Lake, I.R., 2017: Food-borne disease and climate change in the United Kingdom. *Environ. Health 16*, 117. https://doi.org/10.1186/s12940-017-0327-0

Newell, D.G., Koopmans, M., Verhoef, L., Duizer, E., Aidara-Kane, A., Sprong, H., Opsteegh, M., Langelaar, M., Threfall, J., Scheutz, F., van der Giessen, J., and Kruse,H., 2010: Food-borne diseases — The challenges of 20years ago still persist while new ones continue to emerge. *Int. J. Food Microbiol.* 139, S3–S15. https://doi.org/10.1016/j.ijfoodmicro.2010.01.021

O'Brian, R.M., 2007: A Caution Regarding Rules of Thumb for Variance Inflation Factors. *Qual. Quant. 41*, 673–690. http://doi.org/10.1007/s11135-006-9018-6

Osborne, J.W. and *Waters, E.*, 2002: Four assumption of Multiple Regression that researchers should always test. *Practic. Assess. Res. Evaluat. 8*(2), 1–5.

Patz, J., Campbell-Lendrum, D., Holloway, T., and *Foley, J.A.*, 2005: Impact of regional climate change on human health. *Nature 438*, 310–317. https://doi.org/10.1038/nature04188

Patz, J.A., Vavrus, S.J., Uejio, C.K., and *McLellan, S.L.*, 2008: Climate change and waterborne disease risk in the Great Lakes region of the U.S. *Amer. J. Prev. Med. 35*, 451–458. https://doi.org/10.1016/j.amepre.2008.08.026

Pongrácz, R., Bartholy, J., and *Kis, A.*, 2014: Estimation of future precipitation conditions for Hungary with special focus on dry periods. *Időjárás 118*, 305–321.

Rojas-Downing, M.M., Nejadhashemi, A.P., Harrigan, T., and Woznicki, S.A., 2017: Climate Change and livestock: Impacts, adaptation and mitigation. Climate Risk Manage. 16, 145–163. https://doi.org/10.1016/j.crm.2017.02.001

Rose, J.B., Epstein, P.R., and *Lipp, E.K.*, 2001: Climate variability and change in the United States: potential impacts on water and foodborne diseases caused by microbiologic agents. *Environ. Health Perspect 109*, 211–221. https://doi.org/10.1289/ehp.01109s2211

Rose, J.B., Daeschner, S., Easterling, D.R., Curriero, F.C., Lele, S., and Patz, J.A., 2000: Climate and waterborne disease outbreaks. J. Amer. Water Works Assoc. 90, 77–87. https://doi.org/10.1002/j.1551-8833.2000.tb09006.x

Schuster-Wallace, C., Dickin, S., and *Metcalfe, C.*, 2014: Waterborne and Foodborne Diseases, Climate Change Impacts on Health. In: Freedman B. (eds) Global Environmental Change. Handbook of Global Environmental Pollution, vol 1. Springer, Dordrecht, 615–622. https://doi.org/10.1007/978-94-007-5784-4_102

Thornton, P.K., van de Steeg, J., Notenbaert, A., and *Herrero, M.*, 2009: The impacts of climate change on livestock and livestock systems in developing countries: A review of what we know and what we need to know. *Agricult. Syst.* 101(3), 113–127. http://dx.doi.org/10.1016/j.agsy.2009.05.002

Topál, D., Hatvani, I.G., and *Kern, Z.*, 2020: Refining projected multidecadal hydroclimate uncertainty in East-Central Europe using CMIP5 and single-model large ensemble simulations. *Theor. Appl. Climatol. 142*, 1147–1167. https://doi.org/10.1007/s00704-020-03361-7

Utaaker, K.S. and *Robertson, L.J.*, 2015: Climate change and foodborne transmission of parasites: A consideration of possible interactions and impacts for selected parasites. *Food Res. Int. 68*, 16–23. https://doi.org/10.1016/j.foodres.2014.06.051

van de Venter, T., 2000: Emerging food-borne disease: a global responsibility. FAO, https://www.fao.org/3/x7133m/x71133m01.pdf

van Meijl, H., Havlik, P., Lotze-Campen, H., Stehfest, E., Witzke, P., Domínguez, I.P., Bodirsky, B.L., van Dijk, M., Doelman, J., Fellmann., T., Humpenöder, F., Koopman, J.F.L., Müller, C., Popp, A., Tabeau, A., Valin, H., and van Zeist, V.J., 2018: Comparing impacts of climate change and mitigation on global agriculture by 2050. Environ. Res. Lett. 13, 064021. https://doi.org/10.1088/1748-9326/aabdc4

Appendix 1

Detailed results of the step-by-step calculations of the backward-elimination method

Step	Number of predictor parameters	Parameters involved in the regression model	*p*-value of ANOVA	Se	Residuals follow normal distribution	Significant parameter (α=5%)	*p*-value of t-test	Parameter eliminated	Reason	Adjusted R^2
1	10	annual mean temperature; annual mean relative humidity; Tmax higher than 30; Tmin higher than 20, R higher than 10 mm; absolute max of diurnal precipitation; longest dry period; longest wet period; RX5	0.061	1578.87	yes	annual mean temperature	0.04	annual precipitation sum	multicollinearity; insignificant parameter	0.169
2	9	annual mean temperature; annual mean relative humidity; Tmax higher than 30; Tmin higher than 20, R higher than 10 mm; absolute max of diurnal precipitation; longest dry period; longest wet period; RX5	0.037	1559.15	yes	annual mean temperature	0.029	Tmax higher than 30	multicollinearity; insignificant parameter	0.189
3	8	annual mean temperature; annual mean relative humidity; Tmin higher than 20; R higher than 10 mm, absolute max of diurnal precipitation; longest dry period; longest wet period; RX5	0.045	1580.7	yes	annual mean temperature	0.047	RX5	multicollinearity; insignificant parameter	0.167

Appendix 1. continue

Step	Number of predictor parameters	Parameters involved in the regression model	*p*-value of ANOVA	Se	Residuals follow normal distribution	Significant parameter (α=5%)	*p*-value of t-test	Parameter eliminated	Reason	Adjusted R^2
4	7	annual mean temperature; annual mean relative humidity, Tmin higher than 20; R higher than 10 mm; absolute max of diurnal precipitation; longest dry period; longest wet period	0.025	1561.8	yes	annual mean temperature	0.044	annual mean relative humidity	multicollinearity; insignificant parameter	0.187
5	6	annual mean temperature; Tmin higher than 20; R higher than 10 mm; absolute max of diurnal precipitation; longest dry period; longest wet period	0.01691	1556.135	yes	annual mean temperature	0.0033	Tmin higher than 20	multicollinearity; insignificant parameter	0.192
6	5	annual mean temperature, R higher than 10 mm; absolute max of diurnal precipitation. longest dry period. longest wet period	0.0124	1556.852	yes	annual mean temperature	0.000125	absolute max of diurnal precipitation	multicollinearity; insignificant parameter	0.192
7	4	annual mean temperature; R higher than 10 mm; longest dry period longest wet period	0.0066	1547.9	yes	annual mean temperature	0.00022	longest wet period	insignificant parameter with highest p-value	0.201
8	3	annual mean temperature; R higher than 10 mm; longest dry period	0.0026	1533.5	yes	annual mean temperature	0.0002	longest dry period	insignificant parameter with highest p-value	0.216
9	2	annual mean temperature; R higher than 10 mm	0.001044	1527.88	yes	annual mean temperature	0.00023	R higher than 10 mm	insignificant parameter with highest p-value	0.222
10	1	annual mean temperature	0.000344	1528.94	yes	annual mean temperature	0.000344	–	–	0.220

DOI:10.28974/idojaras.2023.2.5

IDŐJÁRÁS

Quarterly Journal of the Hungarian Meteorological Service
Vol. 127, No. 2, April – June, 2023, pp. 233–251

Graupel mixing ratio forecast from a cloud resolving numerical weather prediction model as a tool for lightning activity prediction

Boryana Tsenova*, **Konstantin Mladenov**, and **Milen Tsankov**

National Institute of Meteorology and Hydrology,
Sofia, Bulgaria

**Corresponding author E-mail: boryana.tsenova@meteo.bg*

(Manuscript received in final form July 15, 2022)

Abstract— Graupel mixing ratio over Bulgaria for the warm half year of 2021 based on the AROME-BG numerical weather prediction (NWP) model, is evaluated and connected lightning data detected by the ATDnet lightning location network. Lightning data and forecasted graupel mixing ratios were considered on resolutions of 5×5 km and 10×10 km with flash rate for one and three hours, as well on a daily base using upscaling neighborhood method. Two daily model runs are considered – at 06 and 18 UTC. Commonly used skill-scores in meteorological forecasts are used as evaluation metrics – probability of detection (POD), false alarm rate (F), proportion correct index (PC), and frequency bias index (FBI). Lightning probability forecast (based on graupel mixing ratio) is evaluated at diurnal, monthly, and spatial bases. Results show that graupel mixing ratio taken from the cloud resolving NWP model AROME-BG could be used as a tool to forecast lightning probability with a relatively high performance. Decreases of forecast spatial resolution and time frequency lead to improvement of forecast probability of detection (POD) and frequency bias index (FBI) and to a slight deterioration of its false alarm rate (F) and its percent correct (PC), and the impact of forecast time frequency is more pronounced.

Key-words: graupel mixing ratio, lightning, AROME, ATDnet

1. Introduction

Laboratory studies by *Reynolds et al.* (1957), *Takahashi* (1978), and *Jayaratne et al.* (1983) indicated that particle charging in thunderstorms is associated with collisions between riming graupel and vapor grown ice crystals. *Bruning et al.* (2007) found that lightning initiated shortly after the detection of graupel in thunderclouds.

Dotzek et al. (2001) classified that the majority of lightning activity occurs in the cloud regions where graupel particles are present, followed by those with snow and hail. The conclusions of *Lund et al.* (2009) were consistent with Dotzek and Bruning, which show lightning initiation in or near the cloud regions that contain graupel. With the rapid development and improvement of the numerical weather prediction (NWP) models, the regional numerical forecast is usually based on cloud-resolving models that predict the atmospheric microphysics for a few days ahead. *McCaul et al.* (2009) proposed approaches for making time- and space- dependent quantitative short-term forecasts of lightning threats using the Weather Research and Forecasting (WRF) model. They considered upward fluxes of precipitating ice hydrometeors in the mixed-phase region at the -15 ^{o}C level and vertically integrated amounts of ice hydrometeors in each model grid column. Their simulations of diverse cases over North Alabama showed that the vertically integrated amounts of ice hydrometeors are promising for depicting the areal coverage of lightning threat. In our study, the non-hydrostatic AROME model is used. AROME-BG is a small scale numerical prediction model, operational at the National Institute of Meteorology and Hydrology of Bulgaria since November 2017. It was designed to improve short range forecasts of severe events such as intense precipitations, severe storms, fog, and urban heat during heat waves. It is developed by Meteo-France in close collaboration with national and international institutes so as to benefit from the latest research in atmospheric modeling. The physical parameterizations of the model come mostly from the research Méso-NH model, whereas the dynamic core is the non-hydrostratic ALADIN one. In the present study, graupel mixing ratio for the warm half year of 2021 based on AROME-BG over Bulgaria is evaluated and connected to the detected lightning by using an upscaling neighborhood method. Lightning data are taken from the ATDnet (Arrival Time Differencing NETwork) lightning location network of the Met Office (*Lee*, 1986; *Gaffard et al*., 2008). The aim of the study is to evaluate the relationships between the graupel mixing ratio forecasted by AROME-BG and the detected lightning by considering the forecast accuracy in time and location for lightning activity prediction.

In the next sections of the paper, a more detailed description of the NWP model version (Section 1.1), the ATDnet (Section 1.2), and the evaluation metrics used for the study (Section 1.3) are presented. Results and summary are in Section 2 and Section 3, respectively followed by the conclusion in Section 4.

1.1. AROME-BG model

AROME is a non-hydrostatic limited area cloud-resolving model, used to improve the short range forecasts of severe events. It was developed by Meteo-France in close collaboration with national and international institutes so as to benefit from the latest research in atmospheric modeling. It uses mostly the physical parameterizations from the Méso-NH model (http://www.aero.obs-mip.fr/mesonh/) and the dynamic core of the ALADIN model (*Termonia et al*.,

2018). The microphysics scheme used in the present study (as in the operational version of the model running over Bulgaria – AROME-BG) is the three-class ice parameterization ICE3 scheme presented in *Pinty* and *Jabouille* (1998). It follows the approach of *Lin et al*. (1983), which is a three-class ice parameterization coupled to a Kessler scheme (*Kessler*, 1969) used for the warm processes. The ICE3 scheme follows the evolution of the mixing ratios of six water species: vapor, cloud and rain drops, pristine ice, snow, and graupel. The concentration of the precipitating particles is parameterized according to *Caniaux et al*. (1994). The pristine ice category is initiated by two heterogeneous nucleation processes: formation of ice embryos in a supersaturated environment over ice (deposition) following *Meyers et al.* (1992) and freezing of supercooled droplets. In the model, the secondary production of ice crystals or rime-splintering mechanism is following *Hallett* and *Mossop* (1974). The homogeneous nucleation of pristine ice starts at temperatures lower than −35 °C. Ice crystals grow by water vapor deposition. The snow phase is initiated by autoconversion of primary ice crystals, and it grows by deposition of water vapor, by aggregation through small crystal collection and by the riming produced by impaction of cloud droplets and of raindrops. Graupel particles are produced by the heavy riming of snow or by rain freezing, when supercooled raindrops come in contact with pristine ice crystals. According to the heat balance equation and the efficiency of their collecting capacity, graupel particles can grow in dry and wet modes (when riming is very intense and the excess of non-freezable liquid water at the surface of the graupel is shed and forms raindrops). At temperatures above 0 °C, ice particles melt into cloud and rain drops. The cloud droplet autoconversion, accretion, and rain evaporation follow the Kessler scheme. The diameter spectrum of each water species is assumed to follow a generalized gamma distribution. Power-law relationships are used to link the mass and the terminal speed velocity to the particle diameters. Microphysics prognostic variables are advected by the semi-Lagrangian scheme. They act on inertia and gravity terms in the momentum equation and with their thermal inertia in the thermodynamical computations. In addition, ICE3 has been upgraded by a subgrid condensation scheme (*Bougeault*, 1982; *Bechtold et al.* 1995) and a probability density function (PDF)- based sedimentation scheme (*Bouteloup et al*., 1995).

The operational AROME-BG model configuration (actually based on the model version cy43t2) at NIMH is the following: the integration domain is covering Bulgaria, with a horizontal resolution of 2.5 km, 60 vertical levels, a time step of 60 s, and a forecast range of 36 h. It runs four times daily – at 00, 06, 12, and 18 UTC – and uses the ALADIN-BG output for initial and boundary conditions. In the present study, the 06 and 18 UTC runs are used. For the aim of the study, the integrated graupel mixing ratio, $r_{g,}$ between model levels 35 and 15 (or between 2756 m and 10306 m) was considered and, as a first approach, cases with $r_g > 0$ were considered as probable lightning occurrence.

1.2. ATDnet

In the present study, lightning data are based on data from the ATDnet (Arrival Time Differencing NETwork) over the territory of Bulgaria for the period April-September 2021. The ATDnet is the most recent version of the VLF (very low frequency) lightning location network of the Met Office that operates since 1987 (*Lee*, 1986, *Gaffard et al*., 2008). It takes advantage of the long propagation paths of the VLF spherics emitted by lightning discharges, which propagate over the horizon via interactions with the ionosphere. The differences in the arrival times of these strokes at the outstations are used to calculate the lightning's location. The ATDnet predominantly detects spherics created by cloud to ground (CG) strokes, as the energy and polarization of spherics created by CG return strokes mean that they can travel more efficiently in the Earth-ionosphere waveguide, and so are more likely to be detected at longer ranges than the typical inter-/intracloud (IC) discharges (*Anderson* and *Klugmann*, 2014). Data are collected every minute and BUFR encoded using the universal BUFR template for lightning data with 15 minutes of data combined into one file, which is then sent by the UK Met Office on behalf of the World Meteorological Organization to member states through its global telecommunication system.

As mentioned above, the resolution of AROME-BG is 2.5×2.5 km. However, due to the uncertainty of ATDnet accuracy over the studied region (*Fig. 1a*), in the present study, lightning data and forecasted graupel mixing ratios were considered on resolutions of 5×5 km and 10×10 km with flash rate for one and three hours, as well on a daily base using the upscaling neighborhood method. This technique was used to evaluate the accuracy of the forecast for the precise location and time, respectively. Cases with lightning were considered as bins from the corresponding mesh with at least one detected flash. As an example, *Fig. 1b* presents the spatial distribution of lightning density on a grid with a resolution of 5 km for the period April-September 2021 over the considered region (left panel) as well the spatial distribution of the cases with at least one detected flash for the same period with the same spatial resolution (right panel). These last values are used to evaluate the ability of the graupel mixing ratio forecasted by AROME-BG to predict lightning activity. In *Fig. 2*, the diurnal distributions of the cases with at least one flash detected by ATDnet over the considered region on grids with a resolution of 5×5 km and 10×10 km, with frequencies of one and three hours, for the period April-September 2021 are shown. *Figs. 1* and *2* give and idea of the number of cases with lightning (as well their spatial distribution) that were compared with the corresponding forecast for the graupel mixing ratios integrated between the 35 and 15 model levels. From *Fig. 2a* it is visible, that a big majority of cases with lightning is between 09 and 21 UTC which is normal for our latitudes. *Fig. 2b* shows the monthly distribution of cases with lightning.

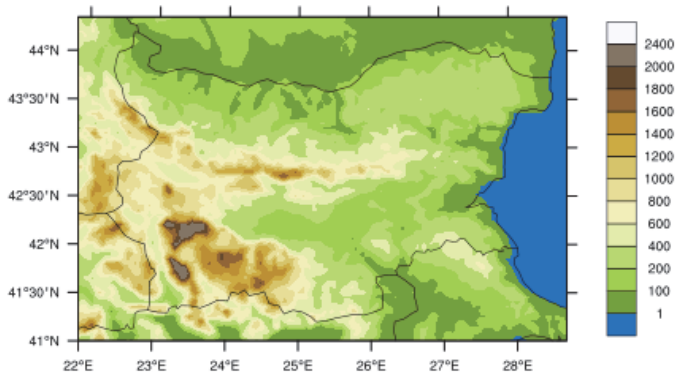

Fig. 1a. Orography of the domain covering Bulgaria and its surroundings, over which the lightning probability forecast performance is evaluated.

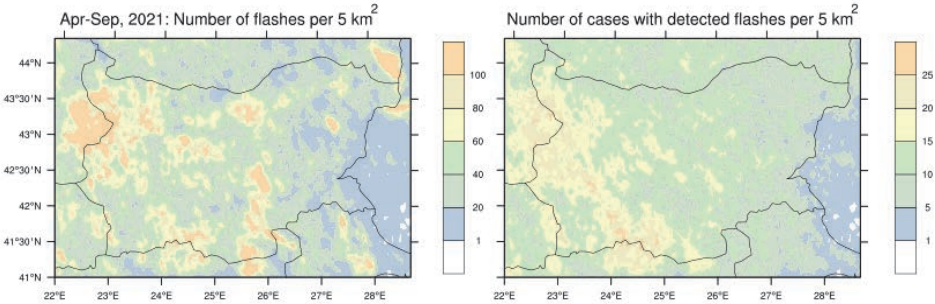

Fig. 1b. Number of flashes per 5x5 km detected between April and September 2021 (left panel) and the corresponding number of cases with at least one detected flash on the grid with a resolution of 5 km (right panel) for the same period.

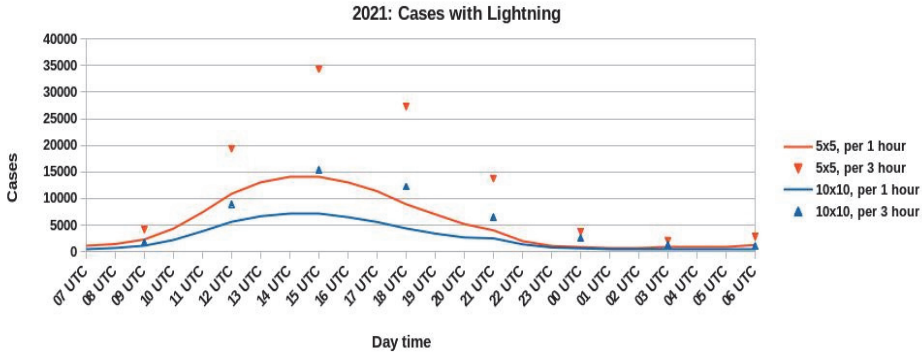

Fig. 2a. Diurnal distributions of the cases with at least one flash detected by ATDnet over the considered region on a grid with a resolution of 5×5 km (red) and 10×10 km (blue), with a frequency of one (line) and three hours (triangle), for the period April-September 2021.

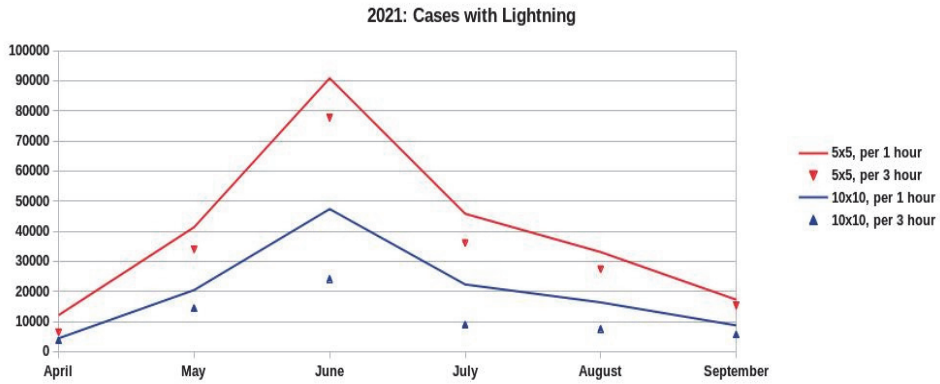

Fig. 2b. Monthly distributions of the cases with at least one flash detected by ATDnet over the considered region on a grid with a resolution of 5×5 km (red) and 10×10 km (blue), with a frequency of one (line) and three hours (triangle), for the period April-September 2021.

1.3. Evaluation metrics

The used here evaluation metrics include four types of commonly used skill-scores in meteorological forecasts: frequency bias index (FBI), proportion correct index (PC), probability of detection (POD) and false alarm rate (F).

Table 1. Parameters used for the evaluation of the forecast skill-scores

	Event observed	
Event forecast	Yes	No
Yes	a	b
No	c	d

Frequency bias index: $FBI = \frac{a+b}{a+c}$; $0 < FBI < \infty$; for a perfect score $FBI = 1$; if $FBI < 1$, there is under forecasting, while if $FBI > 1$ there is an over-forecasting.

Proportion correct index: $PC = \frac{a+b}{a+b+c+d}$; $0 < PC < 1$; for a perfect score $PC = 1$; yes and no forecasts are rewarded equally.

Probability of detection: $POD = \frac{a}{a+c}$; $0 < POD < 1$; for a perfect score $POD = 1$; it is sensitive to misses events and hits only.

False alarm rate: $F = \frac{b}{b+d}$; $0 < F < 1$; for a perfect score $F = 0$; it is sensitive to false alarms .

2. Results

2.1. Diurnal distribution of forecast skill-scores

Figs. 3–6 present the diurnal distributions of the probability detection (POD), false alarm rate (F), proportion correct index (PC), and frequency bias index (FBI), respectively, for the different forecast resolutions and time frequencies for the period between April and September 2021, for the two forecast runs at 06 and 18 UTC. From *Fig. 3* it is visible, that the probability of detection increases with the onset of daylight (when most lightning cases occur) and decreases with the onset of the dark part of the day. Decreasing the spatial resolution leads to a slight increase of POD, while decreasing the time frequency of the forecast leads to a more considerable increasing of POD. Values of POD for the two model runs at 06 and 18 UTC are similar for the respective day hours forecast, except for the three first hours of the 18 UTC run forecast, when the very low POD could be due to the model spin up. Considering daily forecasts of graupel mixing ratio (or forecast on a daily base), values of POD for lightning activity are similar for the two resolutions (5×5 km and 10×10 km) reaching values above 0.9 for daily hours and 0.7 for night hours.

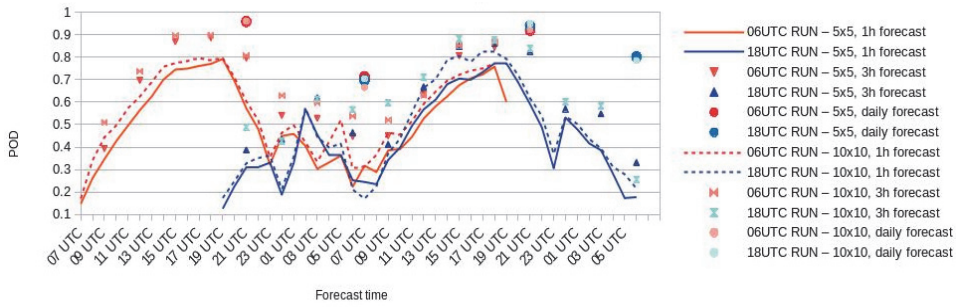

Fig. 3. Diurnal distribution of the probability of detection (POD) for the period April-Sepember 2021.

The decreases of forecast spatial resolution and time frequency may lead to an improvement of forecast probability of detection, but also to a slight deterioration of its false alarm rate (*Fig. 4*) and its proportion correct index (*Fig. 5*), that are slightly worse during the day hours in comparison to night hours. F is below 0.2 for the two resolutions (5×5 km and 10×10 km) and forecast frequencies (1h and 3h) for the night hours lightning activity and between 0.2 and 0.4 for the day hours. On a daily base, the forecasted false alarm rate is around 0.3 for the night and 0.4 for the day. The values of F and PC (*Fig. 5*) for the two

model runs are identical (excluding the spin up time of three hours for the model run at 18 UTC). The proportion correct index is above 0.7 for all forecast considerations except when it is considered on a daily base, where PC <0.6 for the first day forecast on a resolution of 10×10 km.

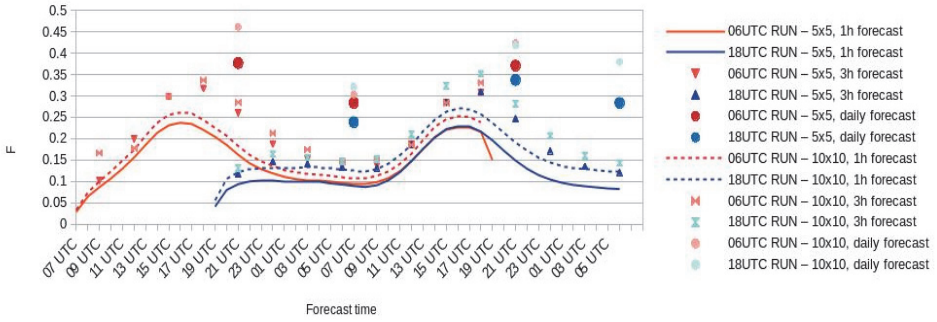

Fig. 4. Diurnal distribution of the false alarm rate (F) for the period April-September 2021.

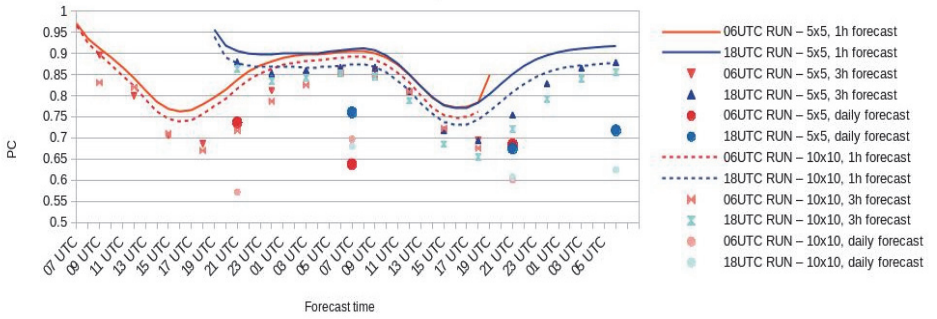

Fig. 5. Diurnal distribution of the proportion correct (PC) for the period April-September 2021.

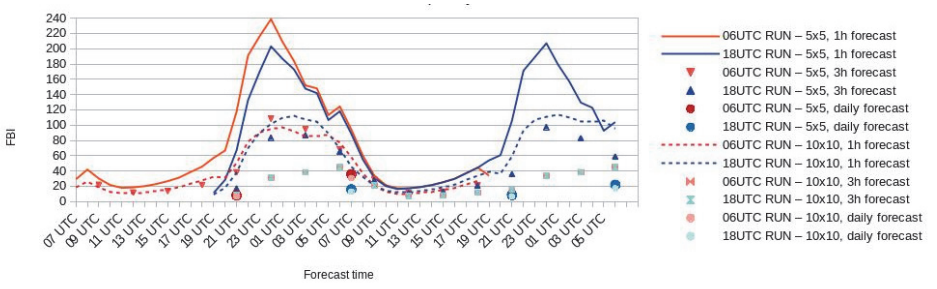

Fig. 6. Diurnal distribution of the frequency bias index (FBI) for the period April-September 2021.

The behavior of the frequency bias index (*Fig. 6*) is similar to behavior of POD with better results for day hours (although still overestimating the lightning activity probability), with improvements due to decreases of forecast resolution and/or its time frequency.

2.2. Monthly distribution of forecast skill-scores

The monthly values of POD, F, PC, and FBI are shown in *Figs. 7–10*. Due to the low number of lightning cases in April 2021 (see *Fig.2b*), for a better view of the results for May-September, April is omitted form these figures. Considering the monthly values of the different indices one can see, that they are different as for the different months, as for the two model runs, and for the considered forecast resolution and time frequency as well.

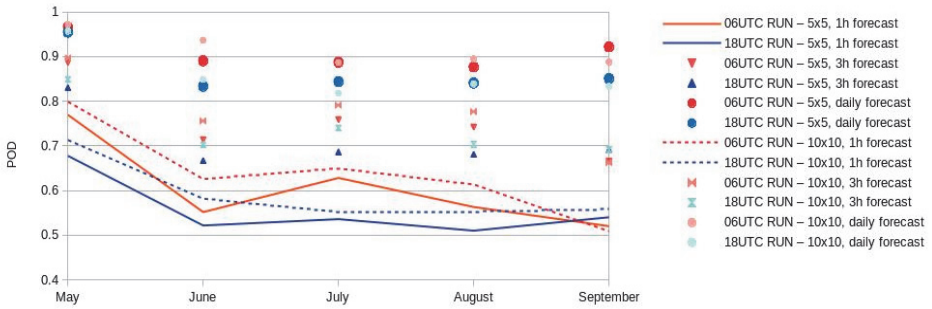

Fig. 7. 2021: Monthly distribution of the probability of detection (POD) for the period May-September 2021.

POD (*Fig. 7*) is higher for model run at 06 UTC in comparison to this for model run at 18 UTC. Probability of detection is highest in May (around and above 0.7) and decreases slightly for other months (remaining above 0.5).

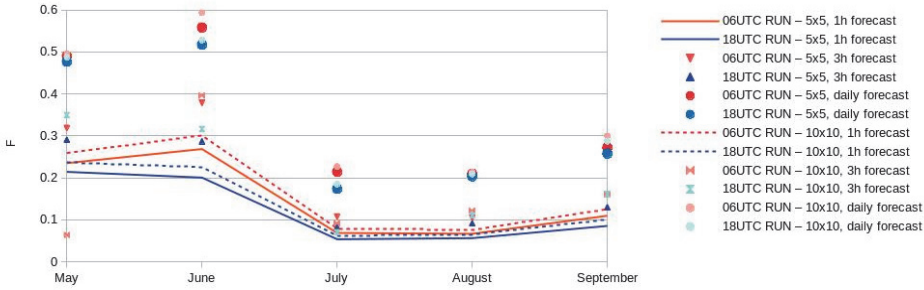

Fig. 8. 2021: Monthly distribution of the false alarm rate (F) for the period May-September 2021.

F (*Fig. 8*) and PC (*Fig. 9*) are considerably lower/higher, respectively, during July, August, and September in comparison to the other months, when the 18 UTC run seems to predict more correctly lightning activity in comparison to the 06 UTC run.

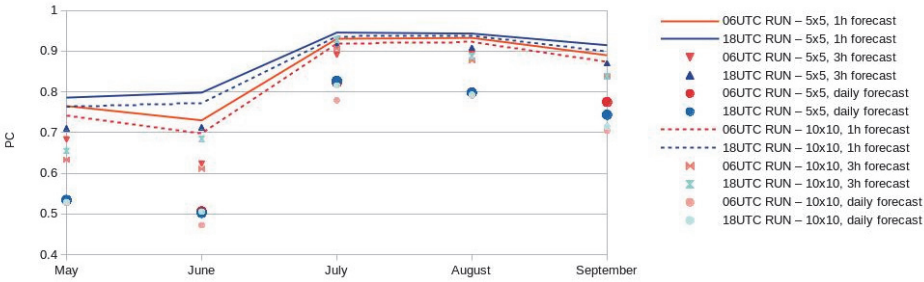

Fig. 9. 2021: Monthly distribution of the proportion correct (PC). for the period May-September 2021.

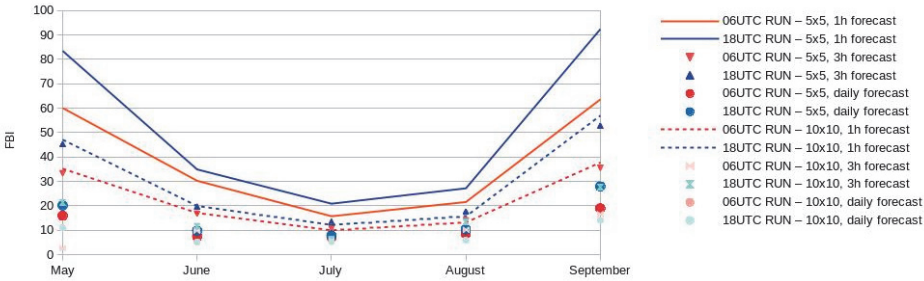

Fig. 10. 2021: Monthly distribution of the frequency bias index (FBI) for the period May-September 2021.

Monthly values of FBI (*Fig. 10*) show a considerable thunderstorm over-forecasting, especially in May and September. Results for the 06 UTC run are slightly better in comparison to those for the 18 UTC run, and the decrease of spatial and temporal resolution also improve the FBI slightly. However, the number of incorrectly forecasted “no lightning cases” is considerably higher than the number of incorrectly forecasted “lightning cases” leading to high values of FBI.

2.3. Spatial distribution of forecast skill-scores

Bulgaria is a relatively small country in the eastern part of the Balkan Peninsula, but with varying topography. Plains occupy about 35% of the territory, while plateaus and hills occupy 41%. The eastern boarder of the country is the Black Sea. The lowest point is the sea level, while the highest (Musala) is 2925 m, which is also the highest mount on the Balkan Peninsula. It is interesting to evaluate the performance of the lightning probability forecast based on the AROME-BG graupel mixing ratio over different parts of the country. *Figs. 11* and *12* show the monthly spatial distribution of POD and F (*Fig. 11*), and PC and FBI (*Fig. 12*) for the model runs at 06 and 18 UTC and the flash density detected by ATDnet for the months April to September 2021. For April, the spatial distribution of POD for the 06 and 18 UTC model runs are similarly with POD mainly above 0.9 at regions where flashes were detected (see the flash density in April), as for points from the grid without any detected flashes, POD is considered as 0. F is mainly between 0.3 and 0.4. The proportion correct index is between 0.5 and 0.7 for April (*Fig. 12*). The distribution of FBI for April shows that over the regions without any detected flashes, FBI is below 5, while where flashes were detected, FBI is between 20 and 60 for the 06 UTC run and reaching values above 100 for the 18 UTC run. For May, similarly to April, the spatial distribution of POD for the 06 and 18 UTC model runs are similar, with POD mainly above 0.9 at regions where flashes were detected. F and PC for May are mainly between 0.2 and 0.4 and between 0.6 and 0.8, with respectively lower or higher values (between 0.2 and 0.3 and between 0.7 and 0.8) at the southeastern (for the 06 UTC run) and eastern parts (for the 18 UTC run). FBI is between 5 and 20 over a big part of western Bulgaria for the 06 UTC model run, while for the 18 UTC run it is mostly above 20. Over the southeastern part for the 18 UTC run, FBI still reaches values above 100. The spatial distribution of POD in June and July differs more considerably for the two model runs. There are much more regions especially at the western part, where POD is above 0.9 for the 06 UTC model run in comparison to the 18 UTC run. In July, over a big part of eastern Bulgaria and over the Black Sea, POD is below 0.5, although there were detected flashes (see the flash density in July). F is below 0.2 in July over the whole considered region, while for June it even reaches values above 0.5. Similar is the distribution of PC following its score evaluation. FBI is mainly below 40 over the whole considered region during the months June, July, and August. The spatial distribution of POD in August is similar for the two model runs, with values mostly above 0.9. There are only some regions (at the northern and southeastern parst of Bulgaria), where The 18 UTC run shows lower scores, with values around 0.5. F and PC spatial distributions for August are similar to those for July. In September, spatial distribution of POD for the 18 UTC run shows more regions with POD>0.9 than for the 06 UTC run, as well more

regions with lower values of F and higher values of PC. However, values of FBI are higher over a big part of the domain for the 18 UTC run, showing higher over-forecast in comparison to the 06 UTC run.

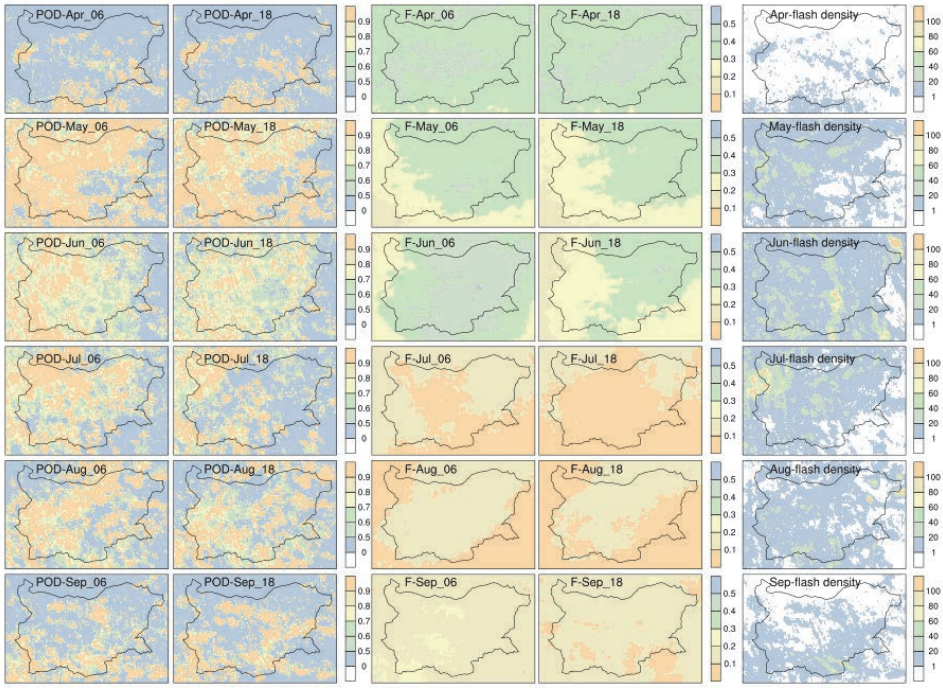

Fig. 11. 2021: Spatial distribution of probability of the detection (POD) and false alarm rate (F) for a grid of 5×5 km, for the model runs at 06 and 18 UTC (denoted respectively with "_06" and "_18"), and the flash density detected by ATDnet for the months April to September 2021 which is used to evaluate model forecast with a time frequency of 3 hours.

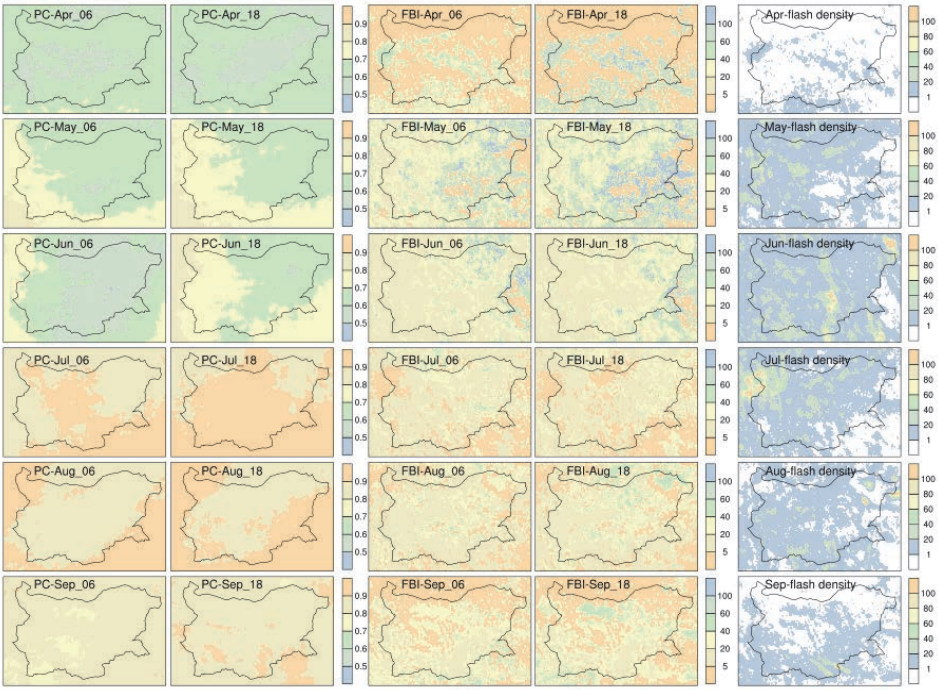

Fig. 12. 2021: Spatial distribution of proportion correct index (PC) and frequency bias index (FBI) for a grid of 5×5 km, for the model runs at 06 and 18 UTC (denoted respectively with "_06" and "_18"), and the flash density detected by ATDnet for the months April to September 2021 which is used to evaluate model forecast with a time frequency of 3 hours

Fig. 13 shows the boxplot of POD and F for lightning probability forecast (evaluated at a resolution of 5 km with a frequency of 3 hours) over different altitudes of the domain for the two model runs. As by default, the boxplot displays the 0th, 25th, 50th, 75th, and 100th percentiles of the corresponding data, or in other words, their minimum, first and third quartiles with median between, and maximum values. The altitude were separated in 8 groups: $z=0$ m, $0 \text{ m}<z\leq100$ m, $100 \text{ m}<z\leq500$ m, $500 \text{ m}<z\leq1000$ m, $1000 \text{ m}<z\leq1500$ m, $1500 \text{ m}<z\leq2000$ m, and $z>2000$ m. The width of boxes is proportional to the number of cases. It is visible that the probability of detection POD is the worst over the sea ($z=0$ m) with mean values about 0.3 for the two model runs. However, the POD medians equal to 0 may indicate that there are more points of the sea with no detected flashes than with not correctly forecasted lightning activity. Also, only over the sea, third quartiles of POD (0.5 and 0.67 for 06 UTC and 18 UTC model runs, respectively) differ from their maximum values that are 1. With the increase of the altitude,

POD scores get better. At the coastal zones (z<50 m and z<100 m), the median of POD is 0.5 (for the two model runs) with mean values also close to 0.5. At altitudes between 100 m and 500 m (z<500 m), which is the largest sample of data, the median of POD for the morning model run is 0.67, while for the evening run it is 0.5. Between 500 m and 2000 m, there is a significant difference between the minimum value (0) and first quartile of POD (that is between 0.4 and 0.5) for the two model runs, except for the 18 UTC run at altitudes between 500 and 1000m (z<1000). At these altitudes, the POD medians are around 0.8 and the mean values are between 0.6 and 0.7. The false alarm rate does not differ considerably for the different altitudes as for the two model runs, with median around 0.2.

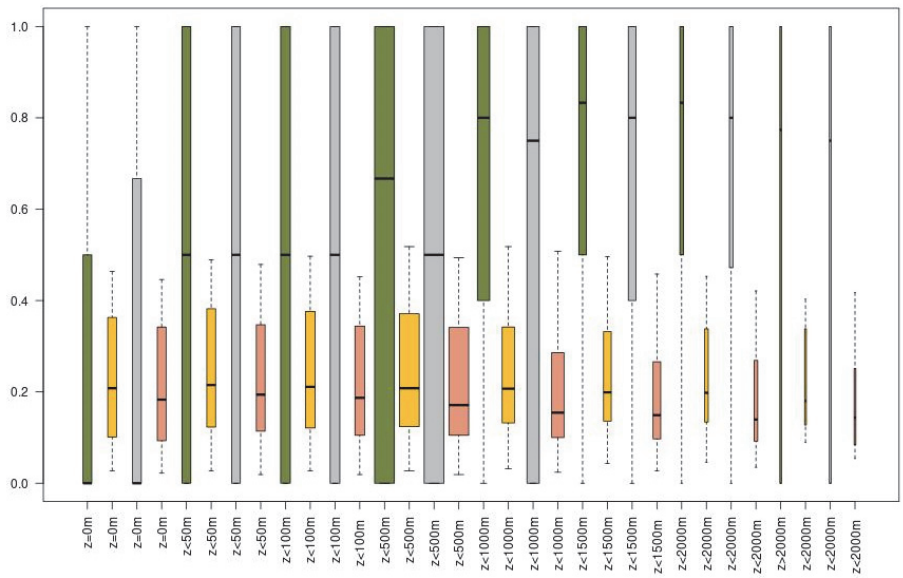

Fig. 13. Box plot of the probability of detection POD (green for the 06 UTC model run and grey for the 18 UTC model run) and false alarm rate F (yellow for the 06 UTC model run and orange for the 18 UTC model run) for different altitudes over the sea level. (The forecast is evaluated at a resolution of 5×5 km with a 3 hours frequency.)

2.4. Case study

Fig. 14 presents the hourly forecast (06 UTC run) for the graupel mixing ratio, r_g, integrated between 2756 m and 10306 m combined with the corresponding "lightning cases" according to the ATDnet flashes on a spatial grid of 5×5 km on July 1, 2021. This date was chosen as it is representing the different forecast skill-scores for the different hours. For this day, the thunderstorm probability forecast

based on r_g seems to be relatively satisfactory for the afternoon hours (as well as for the two days of the forecast), however with a visible overestimation of thunderstorm regions, while during the morning and evening hours, there are more lightning cases over regions, where no graupel mixing ratio was forecasted by AROME-BG. There were no detected lightning between 08 and 09 UTC on July 1 and between 02 and 07 UTC on July 2, and then POD and FBI have no values, while F and PC show very good skill-scores (with very low and high values, respectively), because regions with forecasted $r_g > 0$ are also a few. There are some hours when FBI is very high. At 08 UTC on July 2 for example, there are only three lightning cases on the eastern part of the domain (in the Black Sea) that were not predicted by the model. This results, as expected, in a null probability of detection, but also in a very high frequency bias index of 236 due to the low number of lightning cases. One hour later, at 09 UTC, lightning cases were still not predicted by the model, but their number is 29 (much higher in comparison to 08 UTC). However, as the number of non-lightning cases with forecasted $r_g > 0$ are not much more than those at 08 UTC (994 versus 709), it results in a significantly lower FBI of 34 (still very high and showing an over-forecasting of the thunderstorm probability over the whole domain). FBI is below 1 (0.19) only at the first hour of model integration, when there were no regions with forecasted $r_g > 0$, while lightning were detected. Results from the present case study also show that the increase of the number of lightning cases lead to a deterioration of the false alarm rate skill-scores almost independently of the forecast success rate, which suggests that F should not be considered independently.

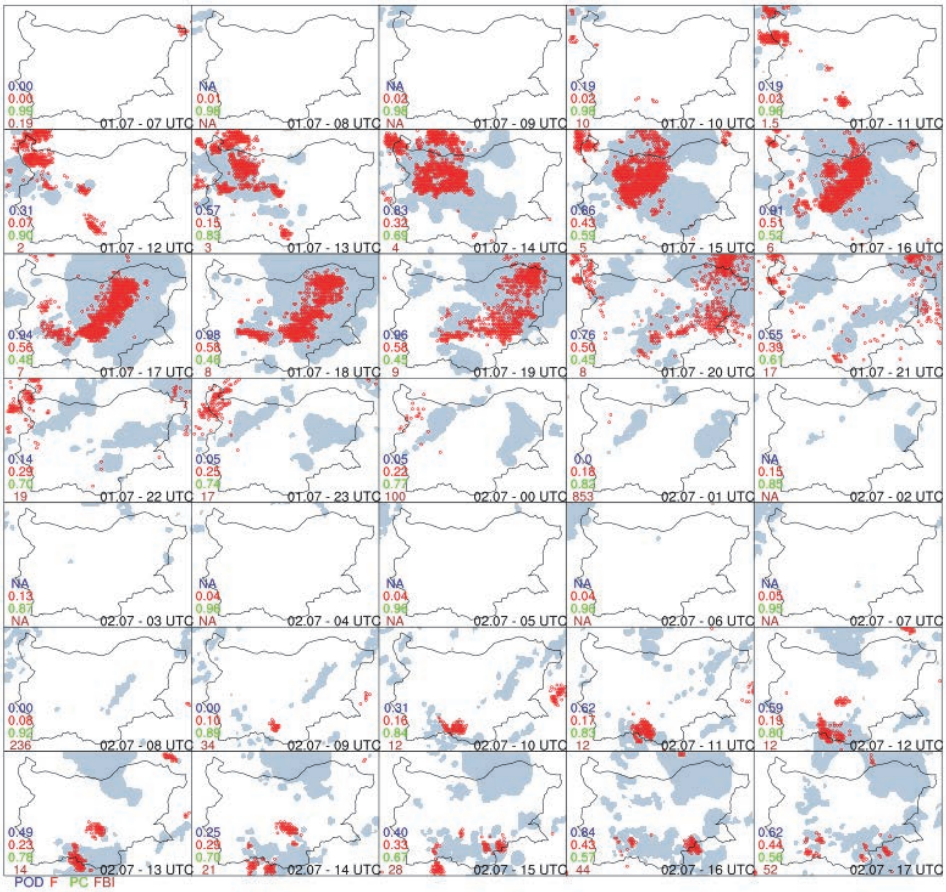

Fig. 14. AROME-BG forecast on July 1, 2021 (06 UTC run) for the graupel mixing ratio $r_g > 0$ integrated between 2756 m and 10306 m (grey) and cases with flashes detected by the ATDnet (red) with spatial resolution 5×5 km. Respective values of POD (in blue), F (in red), PC (in green), and FBI (in brown) are indicated for each hour of the forecast.

3. Summary

The results of this study show that:

– The decreases of the spatial resolution and time frequency of the forecast lead to an improvement of forecast's probability of detection (POD) and frequency bias index (FBI) and to a slight deterioration of its false alarm rate (F) and its proportion correct index (PC), and the impact of the time frequency is more pronounced.

Considering diurnal forecast distributions:

– The probability of detection (POD) and the frequency bias index (FBI) give considerably better scores of the forecast during the day hours in comparison

to the night hours, which shows that lightning activity is better forecasted and with less overestimations during the day, when in principle most flashes are detected;

- The false alarm rate (F) and the proportion correct index (PC) give slightly better scores of the forecast during the night hours. An explanation to these results could be the higher number of night cases that are without detected flashes, and then their proportion to all corresponding night cases is higher;
- There are no significant differences between POD, F, and PC for the two different model runs at 06 and 18 UTC, while FBI gives slightly better scores to the 18 UTC model run;

Considering monthly distributions:

- The robability of detection (POD) is higher for the first part of the warm half year of 2021, while the other considered skill-scores give better results in July, August, and September; the month with highest number of lightning cases, June has the lowest skill-scores;
- Regarding POD and FBI, there are differences in the monthly scores of the two model runs, and the 06 UTC run is with higher values of probability of detection and lower values of frequency bias index;

Considering the spatial forecast distributions:

- The false alarm rate (F) and the proportion correct index (PC) have similar spatial distribution of skill-scores for all months;
- In April, May, and September, the probability of detection (POD) is high over the regions with detected lightning activity for the two model runs, but the false alarm rate (F) have also high values (especially in April) over the whole considered domain; the score of the frequency bias index (FBI) differs for the two model runs during these months with higher values for the 18 UTC run;
- In June and July (the months with highest lightning activity over Bulgaria), skill-scores give different results for the two model runs, with higher POD and F for the 06 UTC run; better scores are obtained in the western part of Bulgaria, while the forecast for lightning activity over the Black Sea (eastern part of the domain) is worse;

Considering the height over the sea level forecast distribution

- Lightning probability forecast performance is similar for the two model runs at all considered altitudes, with slightly lower performance of the evening forecast; POD is improving with the increase of the terrain height, while F is not affected significantly.

4. Conclusions

In the present study, graupel mixing ratio for the warm half year 2021 based on AROME-BG model forecasts over Bulgaria was evaluated and connected to the detected lightning by using upscalling neighborhood method. Lightning data and forecasted graupel mixing ratios were considered on resolutions of 5×5 km and 10×10 km with flash rate for one and three hours, as well on a daily base using the upscaling neighborhood method. This technique was used to evaluate the accuracy of the forecast for the precise location and time, respectively. The main conclusion from the study is that the graupel mixing ratio taken from the cloud-resolving NWP model AROME-BG could be used as a tool to forecast lightning probability with a relatively high performance. The relatively low performance over the sea could be due to different reasons, like the model performance or the not appropriate considered model levels over the water pool. Such investigations have to be done in the future. Furthermore, it is expected that the inclusion of data assimilation in the operational numerical weather prediction at the National Institute of Meteorology and Hydrology of Bulgaria and especially the assimilation of lightning data will improve the lightning probability forecast in time and place.

References

Anderson, G. and *Klugmann, D.,* 2014: European lightning density using ATDnet data. *Nat. Hazards Earth Syst. Sci. 14*, 815–829. https://doi.org/10.5194/nhess-14-815-2014

Bechtold, P., J. Cuijpers, P. Mascart, and *P. Trouilhet*, 1995: Modelling of trade-wind cumuli with a low-order turbulence model–toward a unified description of Cu and Sc clouds in meteorological models. *J. Atmos. Sci. 52*, 455–463. https://doi.org/10.1175/1520-0469(1995)052<0455:MOTWCW>2.0.CO;2

Bougeault, P., 1982: Cloud-ensemble relations based on the gamma probability distribution for the higher-order models of the planetary boundary layer. *J. Atmos. Sci. 39*, 2691–2700. https://doi.org/10.1175/1520-0469(1982)039<2691:CERBOT>2.0.CO;2

Bouteloup, Y., 1995: Improvement of the spectral representation of the earth topography with a variational method. *Mon. Weather Rev. 123*, 1560–1573. https://doi.org/10.1175/1520-0493(1995)123<1560:IOTSRO>2.0.CO;2

Bruning E.C., Rust W.D., Schuur T.J., MacGorman D.R., Krehbiel P.R., and *Rison W.,* 2007: Electrical and polarimetric radar observations of a multicell storm in TELEX. *Mon. Weather Rev. 135*, 2525. https://doi.org/10.1175/MWR3421.1

Caniaux, G., Redelsperger, J.-L., and *Lafore, J.-P.,* 1994: A numerical study of the stratiform region of a fast-moving squall line. Part I: general description and water and heat budgets. *J. Atmos. Sci. 51*, 046–2074. https://doi.org/10.1175/1520-0469(1994)051<2046:ANSOTS>2.0.CO;2

Dotzek N., Holler H., Thery C., and *Fehr T.,* 2001: Lightning evolution related to radar-derived microphysics in the 21 July 1998 EULINOX supercell storm. *Atmos. Res. 56* (1-4), 335. https://doi.org/10.1016/S0169-8095(00)00085-5

Hallett, J. and *Mossop, S.C.,* 1974: Production of secondary ice particles during the riming process. *Nature 249*, 26–28. https://doi.org/10.1038/249026a0

Gaffard, C., Nash, J., Atkinson, N., Bennett, A., Callaghan, G., Hibbett, E., Taylor, P., Turp, M., and *Schulz, W.,* 2008: Observing lightning around the globe from the surface, in: the Preprints, 20th International Lightning Detection Conference, Tucson, Arizona, 21–23.

Jayaratne, E.R., Saunders, C.P.R., and *Hallett, J.*, 1983: Laboratory studies of the charging of soft-hail during icecrystal interactions. *Quart. J. Roy. Meteorol. Soc. 109*, 609–630. https://doi.org/10.1002/qj.49710946111

Kessler, E., 1969: On the distribution and continuity of water substances in atmosphericcirculations. Meteorol. Monogr. 10, 32 Bolton. https://doi.org/10.1007/978-1-935704-36-2

Lee, A.C., 1986: An operational system for the remote location of lightning flashes using a VLF arrival time difference technique. *J. Atmos. Oc. Technol. 3*, 630–642. https://doi.org/10.1175/1520-0426(1986)003<0630:AOSFTR>2.0.CO;2

Lin, Y.-L., Farley, R.D., and *Orville, H.D.*, 1983: Bulk parameterization of the snow field in a cloud model. *J. Clim. Appl. Meteorol. 22*, 1065–1092 https://doi.org/10.1175/1520-0450(1983)022<1065:BPOTSF>2.0.CO;2

Lund N.R., MacGorman D.R., Schuur T.J., Biggerstaff M.I., and *Rust W.D.*, 2009: Relationships between lightning location and polarimetric radar signatures in a small mesoscale convective system. *Month. Weather Rev. 137*, 4151. https://doi.org/10.1175/2009MWR2860.1

McCaul, E.W., Goodman, S.J., LaCasse, K.M., and *Cecil, D.J.* 2009: Forecasting lightning threats using cloud-resolving model simulations, *Weather Forecast. 24*, 709–729. https://doi.org/10.1175/2008WAF2222152.1

Meyers, M.P., DeMott, P.J., and *Cotton, W.R.*, 1992: New primary ice-nucleation parameterizations in an explicit cloud model. *J. Appl. Meteorol. 31*, 708–721. https://doi.org/10.1175/1520-0450(1992)031<0708:NPINPI>2.0.CO;2

Pinty, J.-P. and *Jabouille, P.*, 1998: A mixed-phased cloud parameterization for use in a mesoscale non-hydrostatic model: Simulations of a squall line and of orographic precipitation. Preprints, Conf. on Cloud Physics, Everett, WA, Amer. Meteor. Soc., 217–220.

Reynolds, S., Brook, M., and *Gourley, M.F.*, 1957: Thunderstorm charge separation. *J. Meteor. 14*, 426–436. https://doi.org/10.1175/1520-0469(1957)014<0426:TCS>2.0.CO;2

Takahashi, T., 1978: Riming electrification as a charge generation mechanism in thunderstorms. *J. Atmos. 35*, 1536–1548. https://doi.org/10.1175/1520-0469(1978)035<1536:REAACG>2.0.CO;2

Termonia, P., Fischer, C., Bazile, E., Bouyssel, F., Brožková, R., Bénard, P., Bochenek, B., Degrauwe, D., Derková, M., El Khatib, R., Hamdi, R., Mašek, J., Pottier, P., Pristov, N., Seity, Y., Smolíková, P., Španiel, O., Tudor, M., Wang, Y., Wittmann, C., and *Joly, A.*: The ALADIN System and its canonical model configurations AROME CY41T1 and ALARO CY40T1. *Geosci. Model Dev., 11*, 257–281. https://doi.org/10.5194/gmd-11-257-2018

DOI:10.28974/idojaras.2023.2.6

IDŐJÁRÁS

Quarterly Journal of the Hungarian Meteorological Service
Vol. 127, No. 2, April – June, 2023, pp. 253–265

The role of temperature on the germination activity of leguminous crops exposed to saline conditions

Noriza Khalid, **Asma H. Sghaier**, **Márton Jolánkai**, and **Ákos Tarnawa**

Department of Agronomy
Hungarian University of Agriculture and Life Sciences
Institute of Agronomy
Gödöllő Campus
Páter Károly u. 1, 2100 Gödöllő, Hungary

Corresponding author E-mail:norizahockey@gmail.com

(Manuscript received in final form April 25, 2022)

Abstract— Germination is an important starting point of plant life. Abiotic stresses during the germination stage in seeds can threaten the development process of a plant species. Abiotic factors such as temperature and salt concentration influence the germination process of various crop seeds, including leguminous species. The aim of this study is to determine the germination rate and seedling growth of leguminous cover crops under two different temperatures and four levels of salt stress. Alfalfa (*Medicago sativa*), red clover (*Trifolium pratense*), and chickpea (*Cicer arietinum*) were studied in this in vitro trial. The study results showed that the increase in sodium chloride (NaCl) concentration suppressed the growth of the germinated seedlings. At the same time, the increase in temperature reduced the germination rate of red clover and chickpea at higher salt concentrations. The data also showed a significant relationship between salt concentration and temperature on shoot and radicle growth in all three leguminous species. These data may benefit farmers and growers trying to cultivate these crops in unfavorable conditions.

Key-words: temperature stress, salt stress, germination, seedlings development, leguminous crops.

1. Introduction

Seed germination is a biological process influenced by biotic and abiotic factors, including water, oxygen, and temperature, to achieve successful germination. A combination of conducive environmental factors and various cellular processes will allow physiological and morphological changes within the seed, resulting in the activation of the embryo. Under optimal temperature, germination starts as the seed absorbs water (seed imbibition), resulting in expansion of the seed and elongation of the embryo (*Tina* and *Leubner-Metzger*, 2017). During germination, starch stored in the endosperm of the seeds is converted to soluble sugars such as sucrose through combined actions of enzymes such as α-amylase, β-amylase, and α-glucosidase. Favorable growing conditions will allow adenosine triphosphate (ATP) regeneration hence, allowing activation of hormones and enzymes responsible for germination, such as abscisic acid (ABA), gibberellins, ethylene, and auxin (IAA) (*Joshi*, 2018). Germination ends when the radicle has grown out of the seed's coating layers and the emergence of the coleoptile protrusion (*Miransari* and *Smith*, 2014).

Abundant studies show that abiotic stresses can affect plant growth at all stages, with stresses during plants' reproductive stage greatly influencing the yield produced. *Gyuricza et al*., (2012) showed that extreme precipitation levels could affect the yield value, protein content, and starch content in wheat and maize grains. At the point of limited water availability for the plant roots, the transpiration rate started to decrease, decreasing biomass produced and simultaneously affecting the yield produced (*Nagy* and *Ján*, 2006). However, stresses inflicted in the early development stage, including germination and seedling development, will significantly affect crop yield. Under abiotic stress conditions, seeds will undergo secondary dormancy, which will prevent seed germination from occurring in unfavorable conditions. This protective mechanism acts as a survival strategy to prevent the emerging seedling from dying or failing to develop further until the reproductive stage (*Miransari* and *Smith*, 2014). Once favorable soil condition is achieved, secondary dormancy will be terminated, and the germination process starts.

According to *Kaymakanova* (2009), high salinity in soil solutions will result in high osmotic pressure that restricts the seed imbibition by preventing water absorption and entry into the seed. In Hungary, about 10% of the soil is classified as strong salinity and alkalinity. The salt contributes to the formation of a cemented, impermeable soil surface which limits the water infiltration into a deeper soil layer (*Várallyay*, 2008). The inability to absorb water due to high salt concentration will also prevent the mobilization of essential nutrients needed for germination. Besides that, a high saline condition during the early growth stage also caused sodium ions (Na^+) and chloride ion (Cl^-) toxicity to the embryo and young seedlings resulting in stunted development of the plants (*Khajeh-Hosseini et al*., 2003; *Kaymakanova*, 2009).

Salt stress caused by NaCl also decreases the content of essential hormones for germination, such as gibberellins, while increasing the ABA levels (*Atia et al.*, 2009). *Shu, et al.,* (2017) also observed the same effect in soybean seed germination, which is delayed by the reduced GA/ABA ratio. Furthermore, a study also shows that salt stress reduces the germination rate by negatively affecting the seeds' nitrogen content, thus reducing the amino acids and protein biosynthesis. Hence, nitrogen compound application in areas with salt stress is suggested to alleviate the side effects of high salinity to the crop (*Atia et al.*, 2009). Another study also suggests fluoride as a potential plant growth regulator that works by inhibiting ABA biogenesis and stimulating soybean seeds' germination under high saline soil (*Shu et al*., 2017).

Climate change is one of the main concerns in the agriculture industry nowadays. Temperature rises around the globe affects food production all around the world. Analysis at the Carpathian Region in Central and Eastern Europe shows an increased temperature pattern in large part of this region within the 49 years of the study conducted. The increase in the yearly frequency of warm nights caused the growing season to start earlier in the majority area of this region (*Lakatos et al.,* 2016). Meanwhile, studies show that temperature elevation can cause thermoinhibition in seed germination. A study on Nigeria's main crops, including maize, rice, and sorghum, shows the impact of increases in temperature on seed germination and seedling development. The high temperature also caused a significant reduction in the length of sorghum stem and leaf length reduction in rice (*Iloh et al*., 2014). In *Arabidopsis thaliana*, high temperature causes B3-domain transcription factor FUSCA3 (FUS3) to accumulate during seed imbibition. Overexpression of FUS3 protein generates a seed that is hypersensitive to a higher optimal temperature, thus preventing germination through de novo synthesis of ABA. Consequently, this will cause the seed to maintain or lead to secondary seed dormancy hence, inhibiting germination and vegetative development (*Chiu et al*., 2012).

It is common for one agricultural land to handle more than one abiotic stress simultaneously. A combination of two or more abiotic stresses will aggravate the impact of each stress, and farmers may need to spend more input to remove or lessen the impacts. High temperature, simultaneously with salt stress, is a common condition, especially in semiarid and arid regions in the world (*Shahid et al*., 2018). High temperatures caused more damaging effects on germination under salinity stress compared to at optimum temperatures. It was observed that the combination of these stresses reduced the germination rate, shoot length, and dry weight of wheat seedlings compared to the effects of one stress alone. The combined stresses also reduced the photosynthetic rate in wheat crops due to a decline in pigmentation (*Neelambari et al*., 2018). *Luan et al.,* (2014) show that a higher rate of germination occurs in sunflower seeds at lower alternating temperatures (10–20 °C) than at higher alternating temperatures (20–30 °C) under the same salinity conditions induced by NaCl. The high temperature may have

increased the moisture evaporation causing salt content elevation by capillary movement and slowing down the activation of metabolic processes, thus reducing the activity of different enzymes responsible for germination (*Luan et al*., 2014).

Therefore, this study was conducted to determine the effect of different salt concentrations and temperatures on the germination and growth of various legume species. The relationship between these two stresses on the germination and development of these crops may benefit farmers and further research.

2. Materials and methods

The trial was conducted in the laboratory of the Crop Production Institute of the Hungarian University of Agriculture and Life Sciences, Gödöllő, Hungary. For this trial, three species of leguminous crops; alfalfa, chickpeas, and red clover were chosen. The seeds were germinated at four different saline treatments and two different temperatures. Sodium chloride (NaCl) was diluted with distilled water to produce 0.5%, 1%, 1.5%, and 2% salt solution. 0% solution consisting of distilled water was used as the control. Seeds were surface sterilized with 5% Hypo solution for 5 minutes and rinsed with distilled water three times. All seeds were germinated on 13.5 cm petri dishes containing single layer Whatman filter paper. Memmert type climatic chamber at 70% moisture was used to control the growing temperature at 10 °C and 20 °C.

Each treatment was repeated four (4) times with each petri dish was filled with 20 seeds except for chickpeas with only 10 seeds per petri dish. All seeds were allowed to germinate at each treatment for 10 days. The number of seeds germinated was counted, and the length of plumule and radicles developed were measured using a ruler on the 10th day after the treatment started. The data collected were analyzed using Microsoft Excel 2010 for charts, while IBM SPSS Statistics 27 was used for the analysis of variance (ANOVA).

3. Results

3.1. Germination percentage at different temperatures and salinity levels

In general, the germination rate of all three cover crop species decreases as the saline concentration increases in both temperature conditions. Moreover, the increase of temperature from 10 °C to 20 °C improves the germination of all three species germinated in 0.5% and 0% saline solutions. However, in 1% saline solution, red clover and chickpea seeds showed a 10.1% and 15% higher germination rate at 10 °C than at 20 °C (*Figs. 1* and *2*). *Fig. 3* showed that only alfalfa seeds germinated at 1.5% NaCl at 20 °C, and all three crops failed to germinate at 2% NaCl. Based on the germination rate, it can be concluded that alfalfa had the highest salt tolerance, followed by red clover, and chickpeas had

the lowest tolerance as the salt concentration increased. The data also showed no significant difference between the germination rate at 0% and 0.5% NaCl for both red clover and chickpeas.

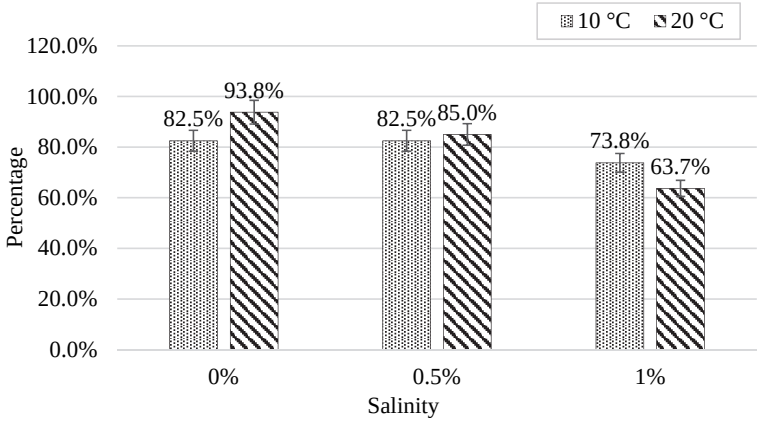

Fig. 1. Germination rate of red clover at 10 °C and 20 °C.

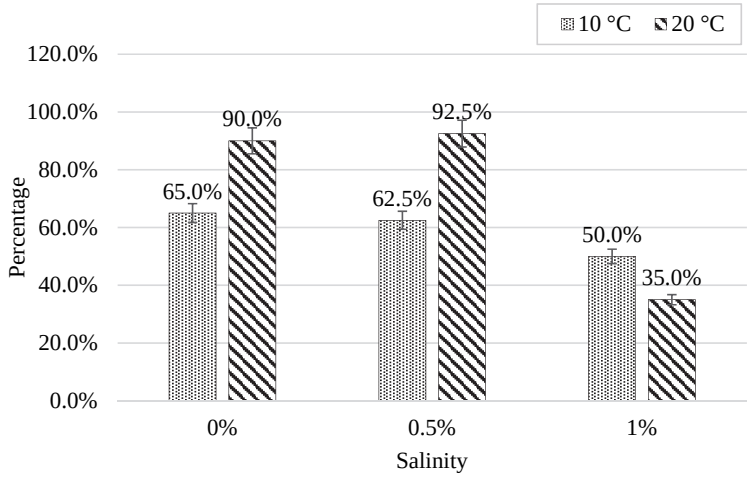

Fig. 2. Germination rate of chickpeas at 10 °C and 20 °C.

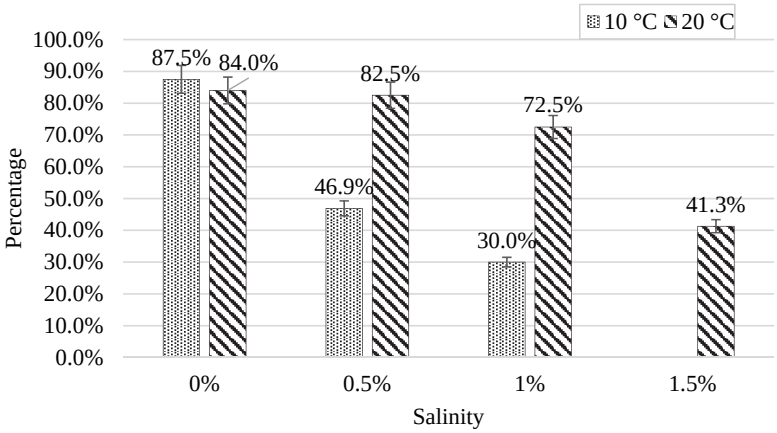

Fig. 3. Germination rate of alfalfa at 10 °C and 20 °C.

Analysis of variance in *Table 1* showed that there was a highly significant difference in the germination rate between groups of cover crop species F (2, 1279) = 19.084, at p<0.001. *Table 2* shows a significant difference in germination rate between red clover and chickpeas and between alfalfa and red clover with p<0.001. In contrast, there was no significant difference in germination rate between chickpeas and alfalfa with p=0.784.

Table 1. Analysis of variance for germination rate of seeds between crop species

	Sum of squares	df	Mean square	F	Sig.
Between groups	7.771	2	3.886	19.084	<0.001
Within groups	260.404	1279	0.204		
Total	268.175	1281			

Table 2. Post hoc test of germination rate between species

	(I) Cover crop	(J) Cover crop	Mean difference (I-J)	Std. error	Sig.
Tukey HSD**	Red clover	Chickpeas	0.144*	0.036	<0.001
		Alfalfa	0.167*	0.028	<0.001
	Chickpeas	Red clover	-0.144*	0.036	<0.001
		Alfalfa	0.023	0.035	0.784
	Alfalfa	Red clover	-0.167*	0.028	<0.001
		Chickpeas	-0.023	0.035	0.784

* The mean difference is significant at the 0.05 level

** Turkey's honest significance test

3.2. Radicle and shoot lengths in different salt concentrations

The radicle and shoot lengths were measured and recorded after 10 days. *Figs. 4* and *5* showed that the increase in salinity suppressed both radicle and shoot growths in all cover crop species. Alfalfa at 20 °C produced longer radicles and shoots average at 0.5%, 1.0%, and 1.5% NaCl concentration. In contrast, chickpeas produced the shortest radicles and shoots average in both temperatures compared to the other crops. Analysis of variance (*Table 3*) showed a highly significant difference of both radicle length $F(3, 1278) = 63.296$ and shoot length $F(3, 1278) = 170.707$ developed under the different salt concentrations with $p<0.001$.

However, there was no significant difference in radicle length developed between 1.0% and 1.5% NaCl. The data was supported by the post-hoc test carried out, as shown in *Table 4* with $p=0.285$. *Fig. 5* showed the same decreasing pattern on shoot length as salt concentration increased. There was significant difference in shoot development in all salt concentrations except between 1% and 1.5% NaCl, which was proved by the post-hoc test with $p=0.704$ (*Table 4*).

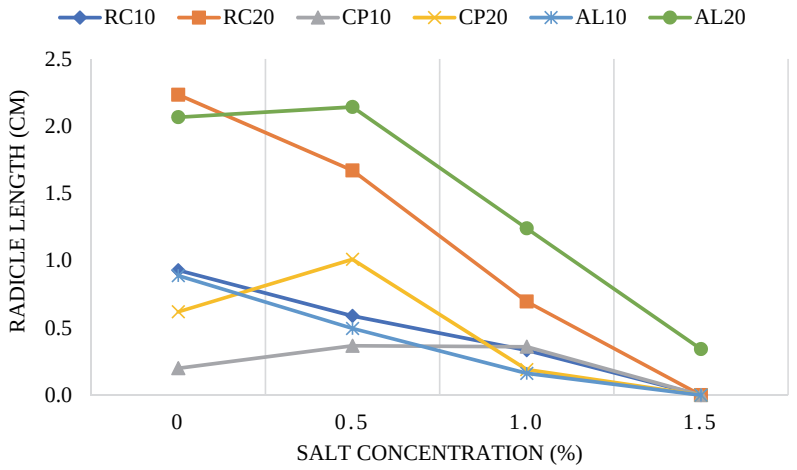

Fig. 4. Mean of radicle length developed after 10 days. RC: Red clover, CP: Chickpeas AL: Alfalfa, 10: 10 °C and 20: 20 °C.

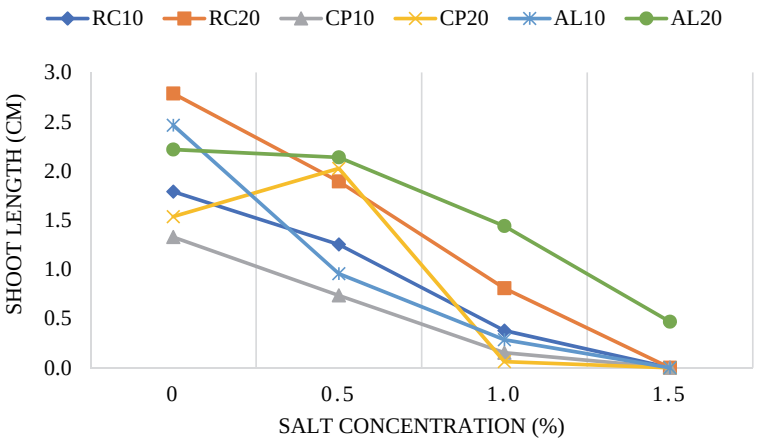

Fig. 5. Mean of shoot length developed after 10 days. RC: Red clover, CP: Chickpeas AL: Alfalfa, 10: 10 °C and 20: 20 °C.

Table 3. Analysis of variance of radicle and shoot lengths at different salt concentrations

		Sum of squares	df	Mean square	F	Sig.
Radicle length	Between groups	158.592	3	52.864	63.294	<.001
	Within groups	1067.411	1278	.835		
	Total	1226.003	1281			
Shoot length	Between groups	545.688	3	181.896	170.707	<0.001
	Within groups	1361.764	1278	1.066		
	Total	1907.453	1281			

Table 4. Post-hoc test (Tukey's honest significance test)

Dependent Variable	(I) Salinity	(J) Salinity	Mean difference (I-J)	Std. error	Sig.
Radicle length	0%	0.5%	0.19152*	0.06454	0.016
		1.0%	0.76608*	0.06458	<0.001
		1.5%	0.96498*	0.11191	<0.001
	0.5%	0%	-0.19152*	0.06454	0.016
		1.0%	0.57456*	0.06458	<0.001
		1.5%	0.77346*	0.11191	<0.001
	1.0%	0%	-0.76608*	0.06458	<0.001
		0.5%	-0.57456*	0.06458	<0.001
		1.5%	0.19890	0.11193	0.285
	1.5%	0%	-0.96498*	0.11191	<0.001
		0.5%	-0.77346*	0.11191	<0.001
		1.0%	-0.19890	0.11193	0.285
Shoot length	0%	0.5%	0.6155*	0.0729	<0.001
		1.0%	1.5342*	0.0729	<0.001
		1.5%	1.6702*	0.1264	<0.001
	0.5%	0%	-0.6155*	0.0729	<0.001
		1.0%	0.9187*	0.0729	<0.001
		1.5%	1.0547*	0.1264	<.001
	1.0%	0%	-1.5342*	0.0729	<0.001
		0.5%	-0.9187*	0.0729	<0.001
		1.5%	0.1360	0.1264	0.704
	1.5%	0%	-1.6702*	0.1264	<0.001
		0.5%	-1.0547*	0.1264	<0.001
		1.0%	-0.1360	0.1264	0.704

* The mean difference is significant at the 0.05 level

3.3. Interaction between variables on radicle and shoot lengths

A three-way analysis of variance was conducted to compare the main effects of cover crop species, temperature, and salinity as well as their interaction on the radicle length (*Table 5*). The cover crop species, temperature and salinity effects

were statistically significant at $p<0.001$. The main effect of cover crop species yielded an effect size of 0.124, indicating that 12.4% of the variance in the radicle length was explained by cover crop species ($F(2,1263)=89.242$, $p<0.001$). The main effect of temperature yielded an effect of 0.237, indicating that 23.7% of the variance in the radicle length was explained by temperature ($F(1, 1263)=392.305$, $p<0.001$). Lastly, the main effect of salinity yielded an effect size of 0.265, indicating that 26.5% of the variance in radicle length was explained by salinity level ($F(3,1263)=151.828$, $p<0.001$). The interaction with all three effects was significant ($F(4,1263)=4.294$, $p=0.002$), showing that there was a combined effect of cover crop species, temperature, and salinity.

Table 5. Analysis of variances on radicle length

Tests of between-subjects effects

Dependent Variable: Radicle length

Source	Type III sum of squares	df	Mean square	F	Sig.	Partial eta squared
Corrected model	614.688[a]	18	34.149	70.554	<0.001	.501
Intercept	555.438	1	555.438	1147.556	<0.001	.476
Covercrop	86.390	2	43.195	89.242	<0.001	.124
Temperature	189.883	1	189.883	392.305	<0.001	.237
Salinity	220.462	3	73.487	151.828	<0.001	.265
Covercrop * Temperature	40.483	2	20.242	41.820	<0.001	.062
Covercrop * Salinity	25.871	4	6.468	13.363	<0.001	.041
Temperature * Salinity	24.362	2	12.181	25.166	<0.001	.038
Covercrop * Temperature * Salinity	8.313	4	2.078	4.294	0.002	.013
Error	611.315	1263	.484			
Total	2378.946	1282				
Corrected total	1226.003	1281				

a. R Squared = .501 (Adjusted R squared = 0.494)

A three-way analysis of variance was also conducted to compare the main effects of cover crop species, temperature, and salinity, as well as their interaction with the shoot length (*Table 6*). The cover crop species, temperature, and salinity effects were statistically significant at $p<.0001$. The main effect of cover crop

species yielded an effect size of 0.055, indicating that 5.5% of the variance in the shoot length was explained by cover crop species ($F(2,1263)=37.078$, $p<0.001$). The main effect of temperature yielded an effect of 0.088, indicating that 8.8% of the variance in the shoot length was explained by temperature ($F(1, 1263)=122.085$, $p<0.001$). Lastly, the main effect of salinity yielded an effect size of 0.338, indicating that 33.8% of the variance in shoot length was explained by salinity level ($F(3, 1263)=215.149$, $p<0.001$). The interaction with all three effects was significant ($F(4,1263)=17.790$, $p<0.001$), showing that there was a combined effect of cover crop species, temperature, and salinity.

Table 6. Analysis of variances on shoot length

Tests of between-subjects effects

Dependent Variable: Shoot length

Source	Type III sum of squares	df	Mean square	F	Sig.	Partial eta squared
Corrected model	838.220[a]	18	46.568	55.007	<0.001	0.439
Intercept	1407.578	1	1407.578	1662.661	<0.001	0.568
Covercrop	62.779	2	31.389	37.078	<0.001	0.055
Temperature	103.355	1	103.355	122.085	<0.001	0.088
Salinity	546.424	3	182.141	215.149	<0.001	0.338
Covercrop * Temperature	2.409	2	1.205	1.423	0.241	0.002
Covercrop * Salinity	19.941	4	4.985	5.889	<0.001	0.018
Temperature * Salinity	25.168	2	12.584	14.865	<0.001	0.023
Covercrop * Temperature * Salinity	60.244	4	15.061	17.790	<0.001	0.053
Error	1069.233	1263	0.847			
Total	4286.480	1282				
Corrected total	1907.453	1281				

a. R Squared = .439 (Adjusted R squared = 0.431)

4. Conclusions

In conclusion, based on the investigation, increased salt stress negatively affects the germination and growth of all three crops species in both growing temperatures. A similar observation was also discovered in other plant species by other studies such as *Laghmouchi et al.* (2017) and *Sharma et al.* (2014). In this trial, elevation in salt concentration reduces the germination rate and inhibits

radicle and shoot elongation on all three legume species. A study on other different legume species shows that salt stress inhibits embryonic axis growth in legume seeds. This defence mechanism against salt stress caused delay and stunted growth in the plumule and radicle of the seedlings (*Tlahig et al*., 2021). *Nadeem et al.*, 2019 also mentioned that leguminous species are more sensitive to salt stress at seedling growth stage than at the germination stage.

Furthermore, the germination data shows, that alfalfa had higher salt stress tolerance during germination at 20 °C than at 10 °C. However, for red clover and chickpeas, the increase in temperature amplifies the salt stress by inhibiting the seeds from germinating, thus affecting the germination rate at higher salt concentrations. Identical results were also presented in other studies on different crop species (*Gulzar et al*., 2001; *Zhang et al*., 2012). In a study on other forage legumes, a higher accumulation of chloride (Cl) ions was found in the seed embryo at a higher temperature. This chloride ion caused toxicity in the embryo, leading to germination suppression (*Humphrey*, 1995).

This study may be extended to other crop species and may be carried out on open field trials in the future. Due to climate change and soil quality degradation nowadays, studies on any abiotic stress impact on every crop are essential for farmers and growers. These data can also be the starting point to discovering the best mitigation action on the adverse effect of abiotic stress on crop plants.

Acknowledgement: This research was supported by the Doctoral Programme of Hungarian Agriculture and Life Sciences. The PhD students involved were funded by the Government of Hungary under Stipendium Hungaricum Scholarship. The authors would like to express their gratitude to all colleagues and technical staff in laboratories for their assistance and contribution to this study

References

Atia, A., Debez, A., Barhoumi, Z., Smaoui, A., and *Abdelly, C.*, 2009: ABA, GA(3), and nitrate may control seed germination of Crithmum maritimum (Apiaceae) under saline conditions. *Comptes Rendus Biol. 332*, 704–710. https://doi.org/10.1016/j.crvi.2009.03.009

Chiu, R. S., Nahal, H., Provart, N. J., and *Gazzarrini, S.*, 2012: The role of the Arabidopsis FUSCA3 transcription factor during inhibition of seed germination at high temperature. *BMC Plant Biol. 12*, 1–16. https://doi.org/10.1186/1471-2229-12-15

Gulzar, S., Khan, M., and *Ungar, I.*, 2001: Effect of salinity and temperature on the germination of Urochondra setulosa (Trin.) C. E. Hubbard. *Seed Sci. Technol. 29*, 21–29.

Gyuricza, C., Balla, I., Tarnawa, Á., Nyárai, H., Kassai, K., Szentpétery, Z., and *Jolánkai, M.*, 2012: Impact of precipitation on yield quantity and quality of wheat and maize crops. *Időjárás 116*, 211–220.

Humphrey, A. E., 1995: Partitioning of chloride ion in the germinating seed of two forage legumes under varied salinity and temperature regimes. *Commun. Soil Sci. Plant Anal. 26*, 3357–3370. https://doi.org/10.1080/00103629509369532

Iloh, A., Omatta, G., Ogbadu, G. H., and *Onyenekwe, P. C.*, 2014: Effects of elevated temperature on seed germination and seedling growth on three cereal crops in Nigeria. *Sci. Res. Ess. 9*(18), 806–813. https://doi.org/10.5897/SRE2014.5968

Joshi, R., 2018: Role of enzymes in seed germination. *Int. J. Creative Res. Thoughts 6*, 1481–1485.

Kaymakanova, M., 2009: Effect of salinity on germination and seed physiology in bean (Phaseolus vulgaris L.). *Biotechnol. Biotechnol. Equipment 23*, 326–329. https://doi.org/10.1080/13102818.2009.10818430

Khajeh-Hosseini, M., Powell, A., and *Bingham, I.,* 2003: The interaction between salinity stress and seed vigour during germination of soyabean seeds. *Seed Sci. Technol 31*, 715–725. https://doi.org/10.15258/sst.2003.31.3.20

Laghmouchi, Y., Belmehdi, O., Bouyahya, A., Senhaji, N., and *Abrini, J.,* 2017: Effect of temperature, salt stress and pH on seed germination of medicinal plant Origanum compactum. *Biocatal. Agricult. Biotechnol. 10*, 156–160. https://doi.org/10.1016/j.bcab.2017.03.002

Lakatos, M., Bihari, Z., Szentimrey, T., Spinoni, J., and *Szalai, S.,* 2016: Analyses of temperature extremes in the Carpathian region in the period 1961–2010. *Időjárás 120*, 41–51.

Luan, Z., Xiao, M., Zhou, D., Zhang, H., Tian, Y., Wu, Y., Guan, B., and *Song, Y.,* 2014: Effects of salinity, temperature, and polyethylene glycol on the seed germination of sunflower (Helianthus annuus L.). *Scie. World J. 2014*, 1–9. https://doi.org/10.1155/2014/170418

Miransari, M. and *Smith, D.,* 2014: Plant hormones and seed germination. *Environ. Experiment. Botany 99*, 110–121. https://doi.org/10.1016/j.envexpbot.2013.11.005

Nadeem, M., Li, J., Yahya, M., Wang, M., Ali, A., Cheng, A., Wang, X., and *Ma, C.,* 2019: Grain legumes and fear of salt stress: focus on mechanisms and management strategies. *Int. J. Molecular Sci. 20*(4), 799. https://doi.org/10.3390/ijms20040799

Nagy, V. and *Ján, H.,* 2006: Method to estimate the critical soil water content of limited availability for plants. *Biologia , 61*(Suppl.19), S289–S293. https://doi.org/10.2478/s11756-006-0175-9

Neelambari., Singh, A. K., and *Kumar, S.,* 2018: Effect of individual and combined salinity and high temperature stress during germination stage of different wheat (Triticum aestivum L.) genotypes. *Int. J. Curr. Microbiol. Appl. Sci. 7*, 1723–1730. https://doi.org/10.20546/ijcmas.2018.707.204

Shahid, S A., Zaman, M., and *Lee, H.,* 2018: Soil salinity: Historical perspectives and a world overview of the problem. In (Eds. *S. Shahid, M. Zaman,* and *H. L.*), Guideline for Salinity Assessment, Mitigation and Adaptation Using Nuclear and Related Techniques. Springer, Cham. 43–53. https://doi.org/10.1007/978-3-319-96190-3_2

Sharma, S., Jamwal, A., Puri, S., Bhattacharya, S., Randev, N., and *Thakur, K.,* 2014: Effect of salt stress on seedling growth and survival of Oenothera biennial . *Int. Res. J. Environ. Sci. 3*, 70–74.

Shu, K., Qi, Y., Chen, F., Meng, Y., Luo, X., Shuai, H., Zhou, W., Ding, J., Du, J., Liu, J., Yang, F., Wang, Q., Liu, W., Yong, T., Wang, X., Feng, Y., and *Yang, W.,* 2017: Salt stress represses soybean seed germination by negatively regulating GA biosynthesis while positively mediating ABA biosynthesis. *Front.Plant Sci. 8*, 1–12. https://doi.org/10.3389/fpls.2017.01372

Tina, S. and *Leubner-Metzger, G.,* 2017: The biomechanics of seed germination. *J. Exper. Botany 68*, 765–783.

Tlahig, S., Bellani, L., Karmous, I., Barbieri, F., Loumerem, M., and *Muccifora., S.,* 2021: Response to salinity in legume species: An insight on the effects of salt stress during seed germination and seedling growth. *Chem. Biodivers. 18*(4), 1–16. https://doi.org/10.1002/cbdv.202000917

Várallyay, G., 2008: Extreme soil moisture regime as limiting factor of the plants' water uptake. *Cereal Res. Commun. 36* (Suppl.), 3–6.

Zhang, H., Irving, L. J., Tian, Y., and *Zhou, D.,* 2012: Influence of salinity and temperature on seed germination rate and the hydrotime model parameters for the halophyte, Chloris virgata, and the glycophyte, Digitaria sanguinalis. *South African J. Botany 78*, 203–210. https://doi.org/10.1016/j.sajb.2011.08.008

INSTRUCTIONS TO AUTHORS OF *IDŐJÁRÁS*

The purpose of the journal is to publish papers in any field of meteorology and atmosphere related scientific areas. These may be

- research papers on new results of scientific investigations,
- critical review articles summarizing the current state of art of a certain topic,
- short contributions dealing with a particular question.

Some issues contain "News" and "Book review", therefore, such contributions are also welcome. The papers must be in American English and should be checked by a native speaker if necessary.

Authors are requested to send their manuscripts to

Editor-in Chief of IDŐJÁRÁS
P.O. Box 38, H-1525 Budapest, Hungary
E-mail: journal.idojaras@met.hu

including all illustrations. MS Word format is preferred in electronic submission. Papers will then be reviewed normally by two independent referees, who remain unidentified for the author(s). The Editor-in-Chief will inform the author(s) whether or not the paper is acceptable for publication, and what modifications, if any, are necessary.

Please, follow the order given below when typing manuscripts.

Title page should consist of the title, the name(s) of the author(s), their affiliation(s) including full postal and e-mail address(es). In case of more than one author, the corresponding author must be identified.

Abstract: should contain the purpose, the applied data and methods as well as the basic conclusion(s) of the paper.

Key-words: must be included (from 5 to 10) to help to classify the topic.

Text: has to be typed in single spacing on an A4 size paper using 14 pt Times New Roman font if possible. Use of S.I. units are expected, and the use of negative exponent is preferred to fractional sign. Mathematical formulae are expected to be as simple as possible and numbered in parentheses at the right margin.

All publications cited in the text should be presented in the *list of references*, arranged in alphabetical order. For an article: name(s) of author(s) in Italics, year, title of article, name of journal, volume, number (the latter two in Italics) and pages. E.g., *Nathan, K.K.,* 1986: A note on the relationship between photosynthetically active radiation and cloud amount. *Időjárás 90,* 10–13. For a book: name(s) of author(s), year, title of the book (all in Italics except the year), publisher and place of publication. E.g., *Junge, C.E.,* 1963: *Air Chemistry and Radioactivity.* Academic Press, New York and London. Reference in the text should contain the name(s) of the author(s) in Italics and year of publication. E.g., in the case of one author: *Miller* (1989); in the case of two authors: *Gamov* and *Cleveland* (1973); and if there are more than two authors: *Smith et al.* (1990). If the name of the author cannot be fitted into the text: *(Miller,* 1989); etc. When referring papers published in the same year by the same author, letters a, b, c, etc. should follow the year of publication. DOI numbers of references should be provided if applicable.

Tables should be marked by Arabic numbers and printed in separate sheets with their numbers and legends given below them. Avoid too lengthy or complicated tables, or tables duplicating results given in other form in the manuscript (e.g., graphs). *Figures* should also be marked with Arabic numbers and printed in black and white or color (under special arrangement) in separate sheets with their numbers and captions given below them. JPG, TIF, GIF, BMP or PNG formats should be used for electronic artwork submission.

More information for authors is available: journal.idojaras@met.hu

Published by the Hungarian Meteorological Service

Budapest, Hungary

ISSN 0324-6329 (Print)

ISSN 2677-187X (Online)